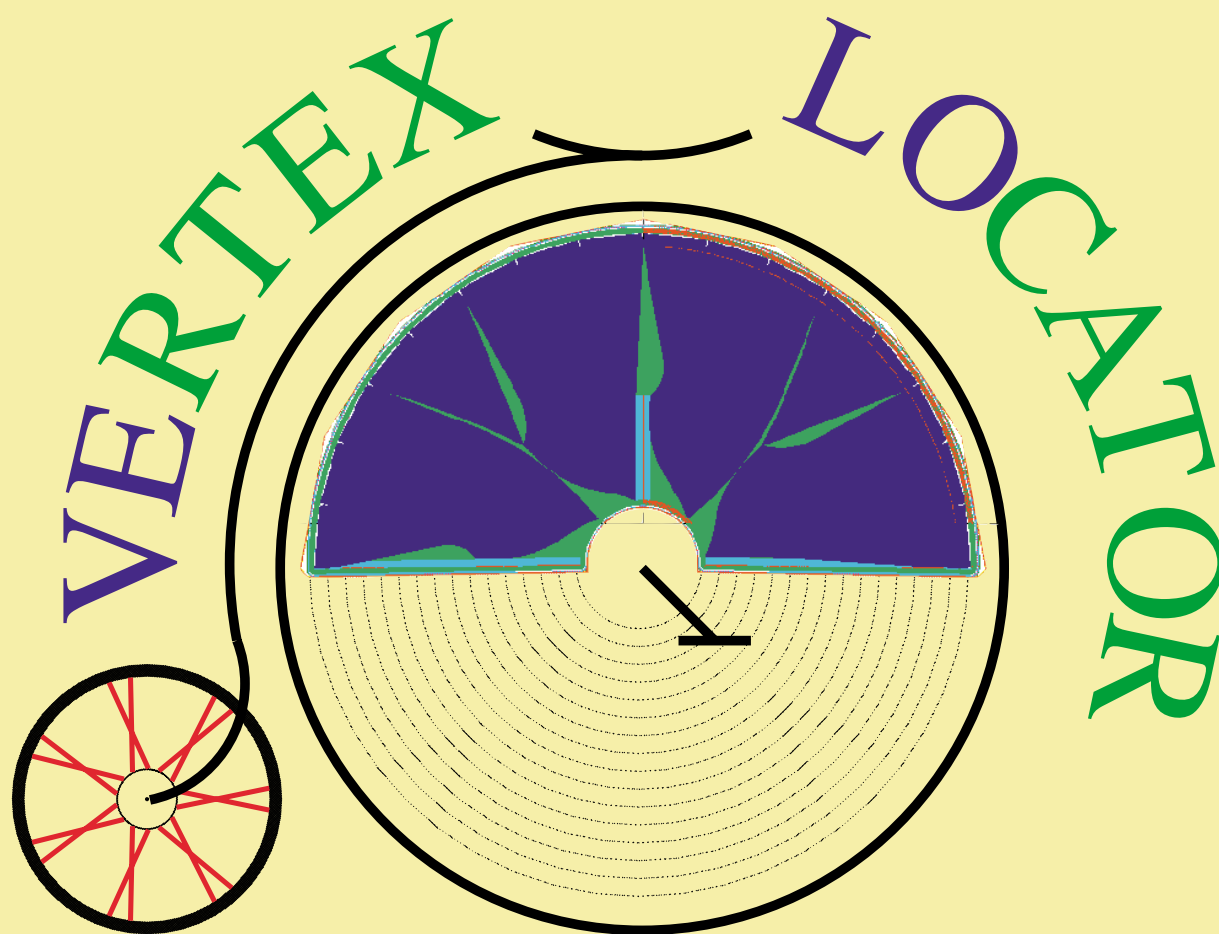




CERN/LHCC 2001-0011
LHCb TDR 5
31 May 2001

TDR VELO



Technical Design Report

VELO TDR

The LHCb Collaboration¹

Brasilian Research Center for Physics, CBPF, Rio de Janeiro, Brasil

P.R. Barbosa Marinho, I. Bediaga, A. França Barbosa, J. Magnin, J. Marques de Miranda, A. Massafferri, A. Reis, R. Silva

University of Rio de Janeiro, UFRJ, Rio de Janeiro, Brasil

S. Amato, P. Colrain, T. da Silva, J.R.T. de Mello Neto, L. de Paula, M. Gandelman, J.H. Lopes, B. Marechal, D. Moraes, E. Polycarpo

University of Clermont-Ferrand II, Clermont-Ferrand, France

Z. Ajaltouni, G. Bohner, V. Breton, R. Cornat, O. Deschamps, A. Falvard¹⁾, P. Henrard, J. Lecoq, P. Perret, C. Rimbault, C. Trouilleau, A. Ziad

CPPM Marseille, Aix University-Marseille II, Marseille, France

E. Aslanides, J.P. Cachemiche, R. Le Gac, O. Leroy, P.L. Liotard, M. Menouni, R. Potheau, A. Tsaregorodtsev, B. Viaud

University of Paris-Sud, LAL Orsay, Orsay, France

G. Barrand, C. Beigbeder-Beau, D. Breton, T. Caceres, O. Callot, Ph. Cros, B. D'Almagne, B. Delcourt, F. Fulda Quenzer, A. Jacholkowska¹⁾, B. Jean- Marie, J. Lefrançois, F. Machefert, V. Tocut, K. Truong, I. Videau

Technical University of Dresden, Dresden, Germany

R. Schwierz, B. Spaan

Max-Planck-Institute for Nuclear Physics, Heidelberg, Germany

C. Bauer, D. Baumeister, N. Bulian, H.P. Fuchs, T. Glebe, W. Hofmann, K.T. Knöpfle, S. Löchner, M. Schmelling, B. Schwingenheuer, F. Sciacca, E. Sexauer²⁾, U. Trunk

Physics Institute, University of Heidelberg, Heidelberg, Germany

S. Bachmann, P. Bock, H. Deppe, F. Eisele, M. Feuerstack-Raible, S. Henneberger, P. Igo-Kemenes, R. Rusnyak, U. Stange, M. Walter, D. Wiedner, U. Uwer

Kirchhoff Institute for Physics, University of Heidelberg, Heidelberg, Germany

V. Lindenstruth, R. Richter, M.W. Schulz, A. Walsch

Laboratori Nazionali dell' INFN, Frascati, Italy

G. Bencivenni, C. Bloise, F. Bossi, P. Campana, G. Capon, P. DeSimone, C. Forti, M.A. Franceschi, F. Murtas, L. Passalacqua, V. Patera⁽¹⁾, A. Sciubba⁽¹⁾
⁽¹⁾also at Dipartimento di Energetica, University of Rome, "La Sapienza"

University of Bologna and INFN, Bologna, Italy

M. Bargiotti, A. Bertin, M. Bruschi, M. Capponi, I. D'Antone, S. de Castro, P. Faccioli,

¹This list includes additional colleagues who made particular contributions to the work presented in this TDR

L. Fabbri, D. Galli, B. Giacobbe, U. Marconi, I. Massa, M. Piccinini, M. Poli, N. Semprini-Cesari, R. Spighi, V. Vagnoni, S. Vecchi, M. Villa, A. Vitale, A. Zoccoli

University of Cagliari and INFN, Cagliari, Italy

A. Cardini, M. Caria, A. Lai, D. Pinci, B. Saitta(1)

(1) also at CERN

University of Ferrara and INFN, Ferrara, Italy

V. Carassiti, A. Cotta Ramusino, P. Dalpiaz, A. Gianoli, M. Martini, F. Petrucci, M. Savrié

University of Florence and INFN, Florence, Italy

A. Bizzeti, M. Calvetti, G. Collazuol, G. Passaleva, M. Veltri

University of Genoa and INFN, Genoa, Italy

S. Cuneo, F. Fontanelli, V. Gracco, P. Musico, A. Petrolini, M. Sannino

University of Milano-Bicocca and INFN, Milano, Italy

M. Alemi, T. Bellunato(1), M. Calvi, C. Matteuzzi, M. Musy, P. Negri, M. Paganoni

(1) also at CERN

University of Rome, “La Sapienza” and INFN, Rome, Italy

G. Auriemma(1), V. Bocci, C. Bosio, D. Fidanza(1), A. Frenkel, K. Harrison, G. Martellotti, S. Martinez, G. Penso, R. Santacesaria, C. Satriano(1), A. Satta

(1) also at University of Basilicata, Potenza, Italy

University of Rome, “Tor Vergata” and INFN, Rome, Italy

G. Carboni, D. Domenici, G. Ganis, R. Messi, L. Pacciani, L. Paoluzi, E. Santovetti

NIKHEF, The Netherlands

G. van Apeldoorn(1,3), N. van Bakel(1,2), T.S. Bauer(1,4), M. van Beuzekom(1), H. Boer Rookhuizen(1), J. van den Brand(1,2), H.J. Bulten(1,2), M. Doets(1), R. van der Eijk(1), I. Gouz(1,5), P. de Groen(1), V. Gromov(1), R. Hierck(1), L. Hommels(1), E. Jans(1), L. Jansen(1), A.P. Kaan(1), T. Ketel(1,2), S. Klous (1,2), B. Koene(1), M. Kraan(1), F. Kroes(1), J. Kuijt(1), M. Merk(1), F. Mul(2), M. Needham(1), H. Schuijlenburg(1), T. Sluijk(1), J. van Tilburg(1), J. Verkooyen(1), H. de Vries(1), L. Wiggers(1), N. Zaitsev(1,3)³⁾, M. Zupan(1)

(1) Foundation of Fundamental Research of Matter in the Netherlands,

(2) Free University Amsterdam,

(3) University of Amsterdam,

(4) University of Utrecht,

(5) on leave from Protvino

Institute of High Energy Physics, Beijing, P.R.C.

C. Gao, C. Jiang, H. Sun, Z. Zhu

Research Centre of High Energy Physics, Tsinghua University, Beijing, P.R.C.

M. Bisset, J.P. Cheng, Y.G. Cui, Y. Gao, H.J. He, Y.P. Kuang, Y.J. Li, Q. Li, Y. Liao, J.P. Ni, B.B. Shao, J.J. Su, Y.R. Tian, Q. Wang, Q.S. Yan

Institute for Nuclear Physics and University of Mining and Metalurgy, Krakow, Poland

E. Banas, J. Blocki, K. Galuszka, L. Hajduk, P. Jalocha, P. Kapusta, B. Kisielewski, W. Kucewicz, T. Lesiak, J. Michalowski, B. Muryn, Z. Natkaniec, W. Ostrowicz, G. Polok, E. Rulikowska-Zarebska, M. Stodulski, M. Witek, P. Zychowski

Soltan Institute for Nuclear Physics, Warsaw, Poland

M. Adamus, A. Chlopik, Z. Guzik, A. Nawrot, M. Szczekowski

Horia Hulubei-National Institute for Physics and Nuclear Engineering (IFIN-HH), Bucharest-Magurele, Romania

D.V. Anghel⁴⁾, C. Coca, A. Cimpean, G. Giolu, C. Magureanu, S. Popescu, T. Preda, A.M. Rosca⁽¹⁾, V.L. Rusu⁵⁾

(1) also at Humbolt University, Berlin

Institute for Nuclear Research (INR), Moscow, Russia

V. Bolotov, S. Filippov, J. Gavrilov, E. Guschin, V. Kloubov, L. Kravchuk, S. Laptev, V. Laptev, V. Postoev, A. Sadovski, I. Semenouk

Institute of Theoretical and Experimental Physics (ITEP), Moscow, Russia

S. Barsuk, I. Belyaev, A. Golutvin, O. Gouchtchine, V. Kiritchenko, G. Kostina, N. Levitski, A. Morozov, P. Pakhlov, D. Roussinov, V. Rusinov, S. Semenov, A. Soldatov, E. Tarkovski

Budker Institute for Nuclear Physics (INP), Novosibirsk, Russia

K. Beloborodov, A. Bondar, A. Bozhenok, A. Buzulutskov, S. Eidelman, V. Golubev, S. Oreshkin, A. Poluektov, S. Serednyakov, L. Shekhtman, B. Shwartz, Z. Silagadze, A. Sokolov, A. Vasiljev

Institute for High Energy Physics (IHEP-Serpukhov), Protvino, Russia

L.A. Afanassieva, I.V. Ajinenko, K. Belous, V. Brekhovskikh, S. Denisov, A.V. Dorokhov, R.I. Dzhelyadin, A. Kobelev, A.K. Konoplyannikov, A.K. Likhoded, V.D. Matveev, V. Novikov, V.F. Obraztsov, A.P. Ostankov, V.I. Rykalin, V.K. Semenov, M.M. Shapkin, N. Smirnov, A. Sokolov, M.M. Soldatov, V.V. Talanov, O.P. Yushchenko

Petersburg Nuclear Physics Institute, Gatchina, St.Petersburg, Russia

B. Botchine, S. Guetz, V. Lazarev, N. Saguidova, E. Spiridenkov, A. Vorobyov, An. Vorobyov

University of Barcelona, Barcelona, Spain

R. Ballabriga⁽¹⁾, S. Ferragut, Ll. Garrido, D. Gascon, S. Luengo⁽¹⁾, R. Miquel⁶⁾, D. Peralta, M. Rosello⁽¹⁾, X. Vilasis⁽¹⁾

(1) also at departament d'Engineria Electronica La Salle, Universitat Ramon Llull, Barcelona

University of Santiago de Compostela, Santiago de Compostela, Spain

B. Adeva, P. Conde, F. Gomez, J.A. Hernando, A. Iglesias, A. Lopez-Aguera, A. Pazos, M. Plo,

J.M. Rodriguez, J.J. Saborido, M.J. Tobar

University of Lausanne, Lausanne, Switzerland

P. Bartalini, A. Bay, B. Carron, C. Currat, O. Dormond, F. Dürrenmatt, Y. Ermoline, R. Frei, G. Gagliardi, G. Haefeli, J.P. Hertig, P. Koppenburg, T. Nakada(1), J.P. Perroud, F. Ronga, O. Schneider, L. Studer, M. Tareb, M.T. Tran
(1) also at CERN, on leave from PSI Villigen

University of Zürich, Zürich, Switzerland

R. Bernet, E. Holzschuh, P. Sievers, O. Steinkamp, U. Straumann, D. Wyler, M. Ziegler

Institute of Physics and Technologies, Kharkiv, Ukraine

S. Maznichenko, O. Omelaenko, Yu. Ranyuk

Institute for Nuclear Research, Kiev, Ukraine

V. Aushev, V. Kiva, I. Kolomiets, Yu. Pavlenko, V. Pugatch, Yu. Vasiliev, V. Zerkov

University of Bristol, Bristol, U.K.

N.H. Brook, J.E. Cole, R.D. Head, A. Phillips, F.F. Wilson

University of Cambridge, Cambridge, U.K.

K. George, V. Gibson, C.R. Jones, S.G. Katvars, C. Shepherd-Themistocleous, C.P. Ward, S.A. Wotton

Rutherford Appleton Laboratory, Chilton, U.K.

C.A.J. Brew, C.J. Densham, S. Easo, B. Franek, J.G.V. Guy, R.N.J. Halsall, J.A. Lidbury, J.V. Morris, A. Papanestis, G.N. Patrick, F.J.P. Soler, S.A. Temple, M.L. Woodward

University of Edinburgh, Edinburgh, U.K.

S. Eisenhardt, A. Khan, F. Muheim, S. Playfer, A. Walker

University of Glasgow, Glasgow, U.K.

A.J. Flavell, A. Halley, V. O'Shea, F.J.P. Soler

University of Liverpool, Liverpool, U.K.

S. Biagi, T. Bowcock, J. Carroll, R. Gamet, G. Gasse, M. McCubbin, C. Parkes, G. Patel, J. Palacios, U. Parzefall, J. Phillips, P. Sutcliffe, P. Turner, V. Wright

Imperial College, London, U.K.

G.J. Barber, D. Clark, P. Dauncey, A. Duane, M. Girone(1), J. Hassard, R. Hill, M.J. John⁷⁾, D.R. Price, P. Savage, B. Simmons, L. Toudup, D. Websdale
(1) also at CERN

University of Oxford, Oxford, U.K.

M. Adinolfi, G. Damerell, J. Bibby, M.J. Charles, N. Harnew, F. Harris, I. McArthur, J. Rademacker, N.J. Smale, S. Topp-Jorgensen, G. Wilkinson

CERN, Geneva, Switzerland

F. Anghinolfi, F. Bal, M. Benayoun⁽¹⁾, W. Bonivento⁽²⁾, A. Braem, J. Buytaert, M. Campbell, A. Cass, M. Cattaneo, E. Chesi, J. Christiansen, R. Chytrcek⁽⁸⁾, J. Closier, P. Collins, G. Corti, C. D'Ambrosio, H. Dijkstra, J.P. Dufey, M. Elsing, M. Ferro-Luzzi, F. Fiedler, W. Flegel, F. Formenti, R. Forty, M. Frank, C. Frei, I. Garcia Alfonso, C. Gaspar, G. Gracia Abril, T. Gys, F. Hahn, S. Haider, J. Harvey, B. Hay⁽⁹⁾, E. van Herwijnen, H.J. Hilke, G. von Holtey, D. Hutchcroft, R. Jacobsson, P. Jarron, C. Joram, B. Jost, A. Kashchuk⁽³⁾, I. Korolko⁽⁴⁾, D. Lacarrère, M. Laub, M. Letheren, J.F. Libby, R. Lindner, M. Losasso, P. Mato Vila, H. Müller, N. Neufeld, J. Ocariz⁽¹⁰⁾, S. Ponce, F. Ranjard, W. Riegler, F. Rohner, T. Ruf, S. Saladino⁽¹¹⁾, S. Schmeling, B. Schmidt, T. Schneider, A. Schopper, W. Snoeys, V. Souvorov⁽³⁾, W. Tejessy, F. Teubert, J. Toledo Alarcon, O. Ullaland, A. Valassi, P. Vazquez Regueiro, F. Vinci do Santos⁽⁵⁾, P. Wertelaers, A. Wright⁽¹²⁾, K. Wyllie

(1) on leave from Universite de Paris VI et VII (LPNHE), Paris

(2) on leave from INFN Cagliari, Cagliari

(3) on leave from Petersburg Nuclear Physics Institute, Gatchina, St.Petersburg

(4) on leave from ITEP, Moscow

(5) on leave from UFRJ, Rio de Janeiro

¹⁾ now at Groupe d'Astroparticules de Montpellier (GAM), Montpellier, France

²⁾ now at Dialog Semiconductor, Kirchheim-Nabern, Germany

³⁾ now at Fortis Bank, Netherlands

⁴⁾ now at Oslo University, Oslo, Norway

⁵⁾ now at Pennsylvania University, Philadelphia, USA

⁶⁾ now at LBNL, Berkeley, USA

⁷⁾ now at Collège de France, Paris, France

⁸⁾ now at IT Division, CERN, Geneva, Switzerland

⁹⁾ now at SWX Swiss Exchange, Geneve, Switzerland

¹⁰⁾ now at Universite de Paris VI et VII (LPNHE), Paris, France

¹²⁾ now at Preveessin, France

¹¹⁾ now at Lancaster University, Lancaster, UK

Acknowledgments

The LHCb Collaboration is greatly indebted to all the technical and administrative staff for their important contributions to the design, testing and prototype activities. We are grateful for their dedicated work and are aware that the successful construction and commissioning of the LHCb experiment will also in future depend on their skills and commitment. The help provided by the CERN Accelerator Physics and LHC vacuum groups in the design of the VELO vacuum vessel is greatly appreciated. We also like to thank L. Gatignon and the staff of the CERN accelerator complex for their support during the test-beam periods. It is a pleasure to acknowledge the contribution of: E. Chesi, R. de Oliveira, A. Gandi, A. Honma, J.R. Moser, K. Muhlemann and A. Teixeira.

Contents

Acknowledgments	viii
1 Introduction	1
1.1 Physics requirements	1
1.2 VELO system overview	2
1.2.1 Constraints	2
1.2.2 Overall dimensions	3
1.2.3 Sensors	5
1.2.4 Readout electronics	6
1.2.5 Detector cooling system	7
1.2.6 Integration with LHC	7
1.2.7 Alignment	8
1.2.8 Material budget	9
1.2.9 Detector resolution	9
1.3 Evolution since the Technical Proposal	9
1.4 Structure of this document	10
2 Summary of R&D and test of prototypes	11
2.1 Silicon	11
2.1.1 Design parameters	11
Thickness	11
Segmentation	12
Oxygenation	13
Cryogenic operation	13
2.1.2 Prototype designs	13
2.1.3 Prototype manufacture	14
2.1.4 Prototype tests	15
2.1.5 Laboratory tests	16
PR01 Prototype	16
PR02 Prototype	16
2.1.6 Test-beam results on non-irradiated sensors	17
Common mode and noise analysis	17
Track fitting and alignment	18
Triggering	18
Resolution	18
SCT128A performance	19
2.1.7 Irradiation procedures	20
2.1.8 Test-beam results on irradiated sensors	20

	DELPHI-ds prototype	21
	PR01 prototypes	21
	PR02 prototype	22
2.1.9	Measurements with a laser	24
2.1.10	Summary	25
2.2	Hybrid	26
2.3	VELO modules	27
2.4	Front-end electronics	29
2.4.1	Front-end chip	29
	The SCT128A and SCTA-VELO chips	30
	The Beetle chip	30
2.4.2	L1 Electronics	31
2.5	Mechanics, wake fields, cooling and vacuum	34
2.5.1	Mechanical aspects of the secondary vacuum container	34
2.5.2	The secondary vacuum container as a wake field suppressor	35
2.5.3	Protection of the secondary vacuum container	38
2.5.4	Proof-of-principle of the CO ₂ cooling system	38
3	Technical design	41
3.1	Sensors	41
3.1.1	Operating conditions for the silicon sensors	44
3.2	Modules	45
3.3	Front-end electronics	46
3.3.1	System architecture	46
3.3.2	L0 Electronics	46
	Front-end chip	46
	The ECS interface	49
	Hybrid	50
3.3.3	L1 Electronics	50
	Repeater cards	50
	Analog data transmission	50
	Digitizer board	50
3.3.4	Power supplies	52
	Low voltage modules	52
	High voltage modules	53
	Crate controller module	53
	Cables	53
3.3.5	Grounding scheme	53
3.4	Mechanics	54
3.4.1	Mechanical design	55
3.5	Vacuum system	58
3.5.1	Layout	58
3.5.2	Protection devices of the LHCb vacuum system	61
3.5.3	LHCb vacuum: effects on LHC operation	61
3.5.4	Risk analysis	62
3.6	Cooling	62
3.7	Material budget	63
3.8	Alignment	64

3.9	Safety aspects	66
4	Simulation results	67
4.1	Software and event samples	67
4.2	Optimization	67
4.2.1	Overall detector optimization	67
4.2.2	Impact on L1 trigger	67
4.3	Particle fluxes	68
4.4	Physics performance	69
4.4.1	Impact parameter resolution	69
4.4.2	Primary vertex, decay length and time resolutions	71
4.4.3	Invariant mass resolutions	72
5	Project organization	73
5.1	Schedule	73
5.1.1	Completion of design and prototyping	73
5.1.2	Construction	73
5.1.3	Installation and commissioning	75
5.2	Milestones	75
5.3	Costs	75
5.4	Division of responsibilities	79

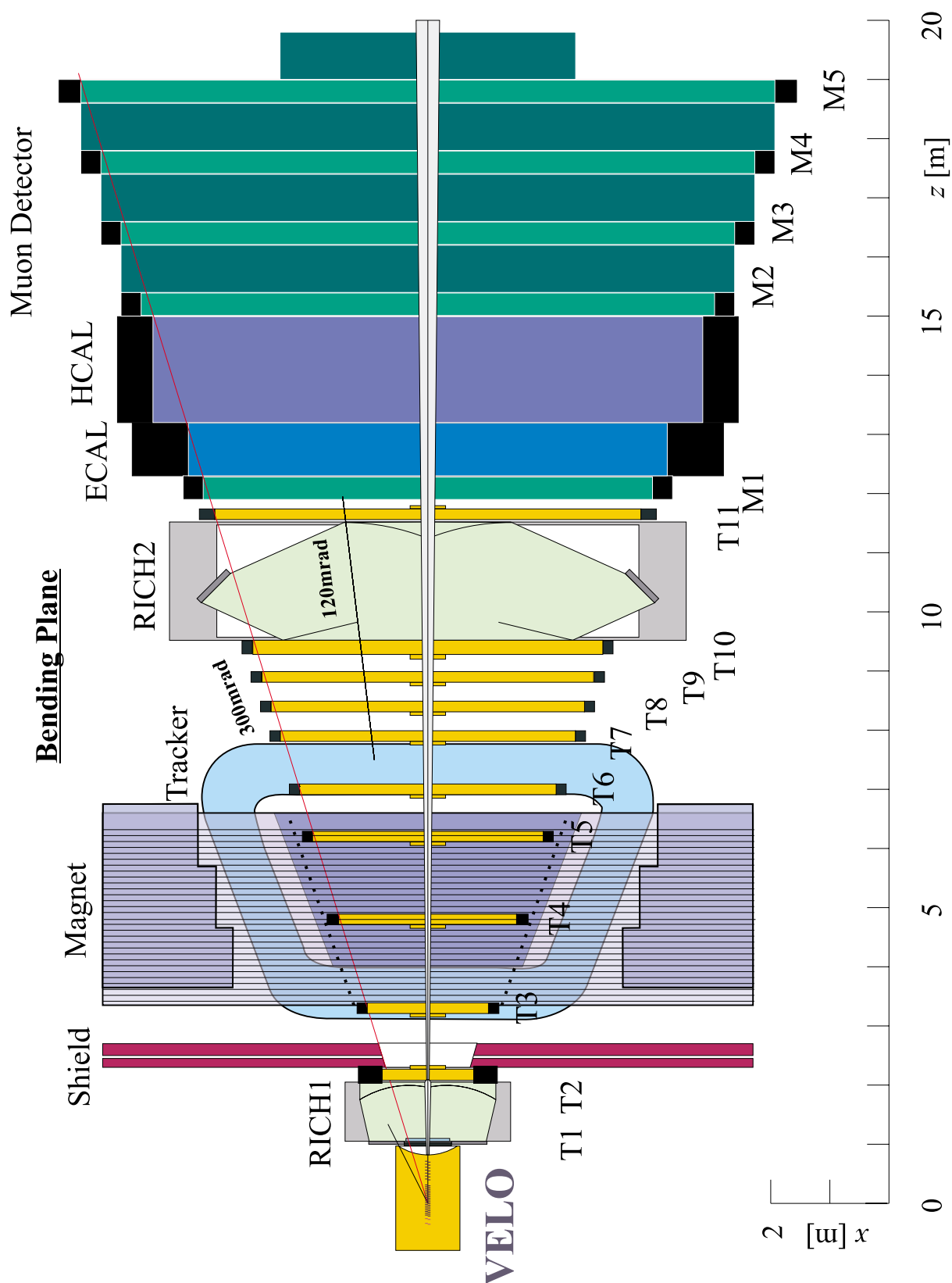


Figure 1: The LHCb spectrometer seen from above (cut in the bending plane), showing the location of the VELO.

1 Introduction

Vertex reconstruction is a fundamental requirement for the LHCb experiment. Displaced secondary vertices are a distinctive feature of b-hadron decays. The **VE**rtex **LO**cator (VELO) has to provide precise measurements of track coordinates close to the interaction region. These are used to reconstruct production and decay vertices of beauty- and charm-hadrons, to provide an accurate measurement of their decay lifetimes, and to measure the impact parameter of particles used to tag their flavor. The VELO measurements are also a vital input to the second level trigger (L1), which enriches the b-decay content of the data.

The VELO features a series of silicon stations placed along the beam direction. They are placed at a radial distance from the beam which is smaller than the aperture required by the LHC during injection and must therefore be retractable. This is achieved by mounting the detectors in a setup similar to Roman pots (Fig. 1.1). The placement of the VELO within the LHCb spectrometer can be seen in Fig. 1, which shows the top view of the LHCb spectrometer. Details of the rest of the experiment can be found in [1, 2]. In this introduction, the physics requirements are discussed, and an overview is given of the VELO detector system. A brief discussion of the evolution since the Technical Proposal is then given, before an outline of the rest of the document.

1.1 Physics requirements

The basic tasks of the LHCb VELO system are the reconstruction of the position of the primary vertex, the detection of tracks which do not originate from the primary vertex and the reconstruction of b-hadron decay vertices.

The VELO has to cover completely the angular acceptance of the downstream detectors.

Special requirements emerge from the use of the VELO information in the L1 trigger. The L1 algorithm requires a fast and standalone three-dimensional pattern recognition to distinguish b-events from those minimum bias events which are accepted by the first level trigger (L0). B-hadrons that have all their decay products within the acceptance of the spectrometer are typically produced with a polar angle below 200 mrad. Hence, the projection of the impact parameter of the decay products to the primary vertex in the rz -plane is large, while in the plane perpendicular to the beam-axis ($r\phi$) it is similar to that of tracks originating from the primary vertex. The L1 trigger exploits this by first reconstructing all tracks in the rz -projection, but reconstructing only tracks in three dimensions which have a significant rz -impact parameter. Hence, the strip pattern on the sensors has strips with constant radius for the rz -track reconstruction, combined with radial-strip sensors having a stereo angle of $(10^\circ - 20^\circ)$ to allow the two projections to be combined.

The $r\phi$ -geometry has also the advantage that it allows in a natural way to choose the smallest strip pitch close to the beam axis, hence best hit resolution where it is needed, and larger strip pitches towards the outside of the sensors. This minimizes the number of readout channels and results in a balanced occupancy throughout the sensor.

The detectors have to operate in an extreme radiation environment which is strongly non-uniform. The damage to silicon at the most irradiated area during one year of operation is equivalent to that of 1 MeV neu-

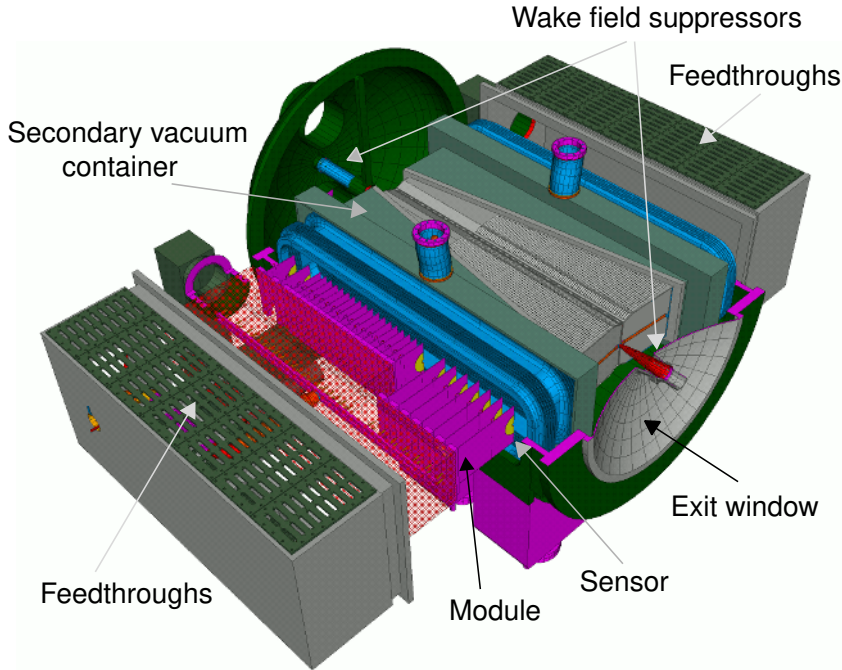


Figure 1.1: The VELO Roman pot configuration. One detector half is not installed to show the sensors.

trons with a flux of 1.3×10^{14} particles/cm² ($= 1.3 \times 10^{14} n_{\text{eq}}/\text{cm}^2$), whereas the irradiation in the outer regions does not exceed a flux of $5 \times 10^{12} n_{\text{eq}}/\text{cm}^2$ (see Fig. 1.2 and section 4.3). The effects of radiation were studied in detail with prototype detectors and are reported in section 2.1.

1.2 VELO system overview

The design of the VELO system is constrained by its proximity to the LHC beams and its integration into the LHCb experiment. This section describes these constraints and the considerations leading to the overall dimensions of the detector. This is followed by an overview of the sub-components of the system. Some global parameters and dimensions are listed in Table 1.1.

1.2.1 Constraints

In the design of the VELO, the following boundary conditions are imposed:

- The need for shielding against RF pickup

from the LHC beams, and the need to protect the LHC vacuum from outgasing of the detector modules, requires a protection to be placed around the detector modules. This material is a major fraction of the total radiation length of the VELO.

- A short track extrapolation distance leads to a better impact parameter measurement, therefore the innermost radius should be as small as possible. In practice, this is limited by the aperture required by the LHC machine. During physics running conditions, the σ of the beams will be less than $100 \mu\text{m}$, but for safety reasons, the closest approach allowed to the nominal beam axis is 5 mm. To this must be added the thickness of the RF-shield, the clearance between the RF shield and the sensors, and the need for about 1 mm of guard-ring structures on the silicon. Taking everything into account, the sensitive area can only start at a radius of 8 mm.

number of stations	25
position of first station upstream	−17.5 cm
position of last station downstream	75 cm
total area of silicon	0.32 m ²
total number of channels	204,800
radiation level at 8 mm	$(0.5 - 1.3) \times 10^{14} n_{\text{eq}}/\text{cm}^2$ per year
radiation level at 50 mm	240 kRad/year
power dissipation	< 1.5 kW
dimensions of the vacuum vessel (length \times \varnothing)	1.8 m \times 1 m

Table 1.1: Global parameters of the VELO system.

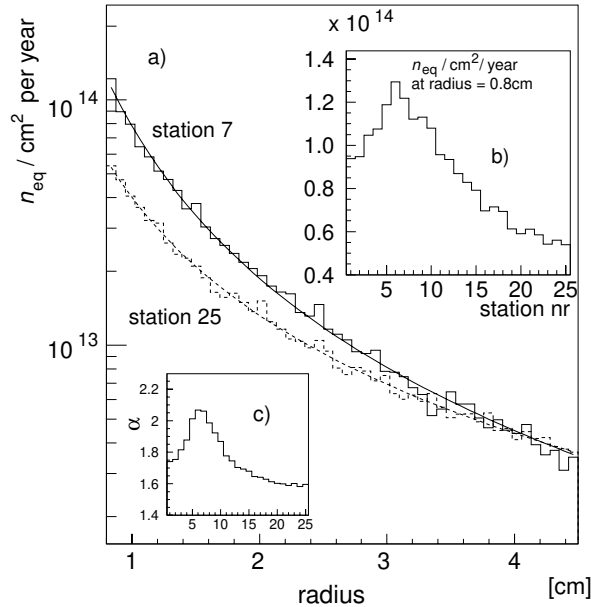


Figure 1.2: a) Total hadron fluences per cm^2 and year normalized to the damage of neutrons of 1 MeV energy, for station 7 and 25 as function of radius. The radial dependence is well described by the function $N \times r^{-\alpha}$, with N and α changing as function of z . b) The flux per year at $r = 0.8$ cm as a function of the station number. c) The parameter α as function of the station number.

- During injection, the aperture required by the LHC machine increases, necessitating the retraction of the two detector halves by 3 cm.
- To allow for a replacement of the sensors in case of radiation damage, access has to be rather simple.

- The number of analog readout channels in the VELO is limited to about 200,000 channels. This is due to the limited space for the vacuum feedthroughs on the VELO vacuum vessel.

1.2.2 Overall dimensions

Apart from covering the full LHCb forward angular acceptance, the VELO also has a partial coverage of the backward hemisphere to improve the primary vertex measurement. The angular coverage is achieved with a series of stations, each providing an R and a ϕ measurement. The number of individual sensors is kept to a minimum, which simplifies the alignment. Each sensor has an azimuthal coverage of $\approx 182^\circ$, giving a small overlap between the right and left halves which is used for their relative alignment.

The L0 trigger aims to select beam crossings with only one pp-interaction by reconstructing the z -position of the interactions using two R -measuring sensors located upstream of the VELO stations. Two station locations are reserved in the VELO vacuum vessel for these pile-up VETO sensors [3]. The VETO trigger will be described in the Trigger technical design report.

The detector setup is defined by the following constraints (see Fig. 1.3):

- A polar angle coverage down to 15 mrad for all events with a primary vertex within $\pm 2\sigma$ of the nominal interaction point together with the minimum dis-

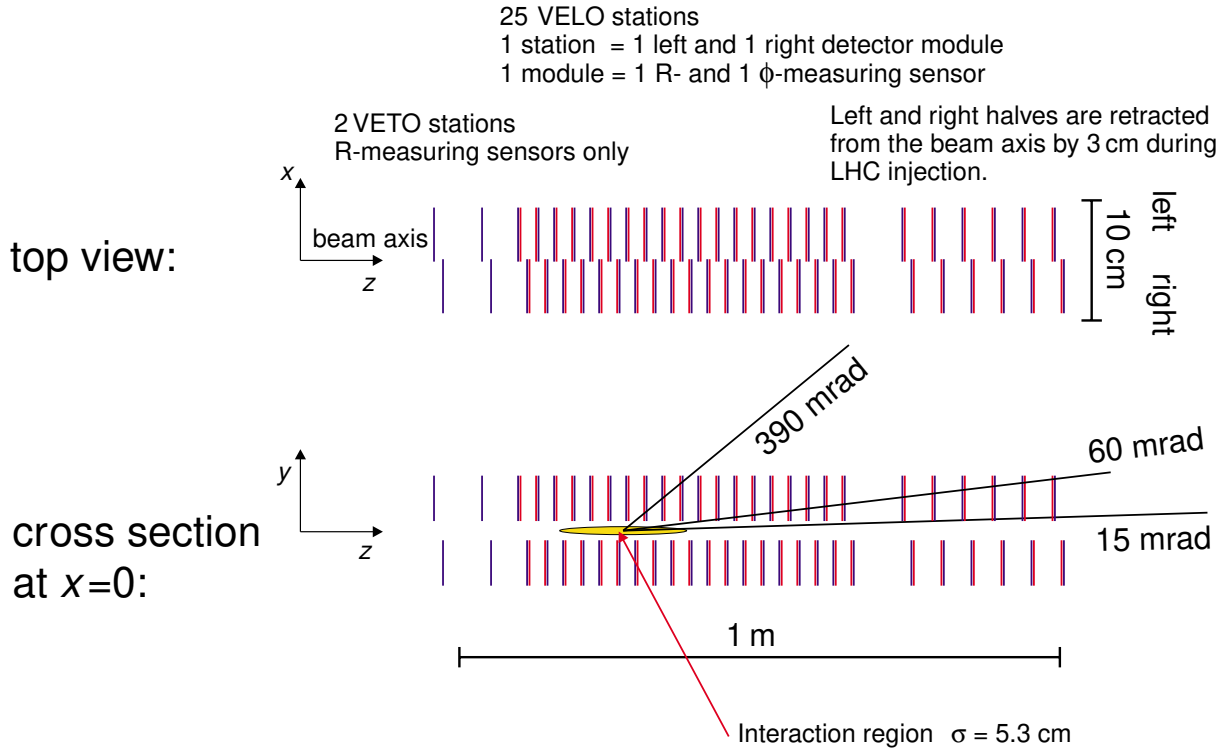


Figure 1.3: Arrangement of detectors along the beam axis. The top figure shows the VELO setup seen from above, indicating the overlap between the left and right detector halves. The bottom figure is a cross section of the setup at $x = 0$ along the beam axis showing also the nominal position of the interaction area ($\pm 2\sigma$). The three lines indicate the maximum and minimum angular coverage of the VELO and the average angle of tracks in minimum bias events respectively.

tance to the beam axis, 8 mm, defines the position of the last downstream stations and the length of the VELO.

- A track in the LHCb spectrometer angular acceptance of $250 \text{ mrad} \times 300 \text{ mrad}$ should cross at least three VELO stations. The outer radius of the sensors is limited to 42 – 45 mm, which allows the use of 100 mm wafers for the sensor production. These two constraints define the distance between the stations in the central region to be about 3 cm. In addition, minimizing the distance from the first measured point of a track to its vertex demands a dense packing of stations.
- To allow for an overlap between the left and right halves, in order to cover the full azimuthal acceptance and for alignment

issues, the detectors in the left and right halves are displaced by 1.5 cm along the beam axis.

- The present setup of 19 stations covering the central part, and 6 stations covering the low angle tracks with a larger distance between stations, is the result of a detailed optimization study [4].

As a result of being able to reconstruct all tracks in the LHCb acceptance ($1.6 < \eta < 4.9$) with the VELO by requiring at least three measured points, the number of hit measurements of a track varies substantially as a function of η and the position of the primary vertex (Fig. 1.4).

	R-sensor	ϕ -sensor
number of sensors	50 + 4(VETO)	50
readout channels per sensor	2048	2048
smallest pitch	40 μm	37 μm
largest pitch	92 μm	98 μm
length of shortest strip	6.4 mm	9.2 mm
length of longest strip	66.6 mm	24.4 mm
inner radius of active area	8 mm	8 mm
outer radius of active area	42 mm	42 mm
angular coverage	182°	$\approx 182^\circ$
stereo angle	–	10°–20°
double metal layer	yes	yes
average occupancy (inner area)	0.5%	0.7%
average occupancy (outer area)	0.9%	0.5%

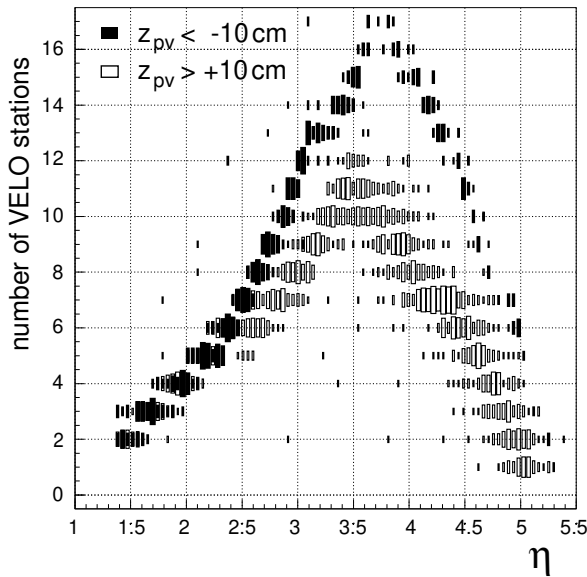
Table 1.2: Parameters of the R- and ϕ -measuring sensors.

Figure 1.4: The number of hits of a track in the VELO stations as function of pseudorapidity η . The two distributions are for tracks from events with a primary vertex 10 cm (–10 cm) from the nominal interaction point. All other tracks are between the two distributions.

1.2.3 Sensors

The silicon sensors have a circular shape, patterned with azimuthal (R measuring) or quasi-radial (ϕ measuring) strips, and span 182°. These views have been chosen in order to optimize the stand-alone tracking performance for

the L1 trigger. By using a double metal layer, it is possible to decouple the routing of the signals from the strip geometry and to move the electronics as far as possible out of the acceptance. Given the constraints outlined in the previous section, the innermost radius of the sensitive area is 8 mm and the outermost radius is ≈ 42 mm.

The concept of the strip layout is illustrated schematically in Fig. 1.5. The strips in the ϕ -sensor are split into an inner and an outer region, chosen to equalize the occupancy in the two regions. The detectors are flipped from station to station, and the strips are tilted with a stereo angle, which is different in sign and magnitude for the inner and outer region. This results in a dog-leg shape, which minimizes the depth of the corrugations needed in the RF shield (Fig. 1.7) to accommodate the shape. The strips in the R-sensor are segmented into 4 (2) azimuthal sections in the inner (outer) regions. With this design it is possible to determine the primary vertex position in the plane perpendicular to the beam using the R-sensors alone, which is an important input to the L1 trigger. The pitch varies with radius, striking a balance between making the occupancy as uniform as possible, and ensuring that the first two points on the track are measured with the finest pitch available.

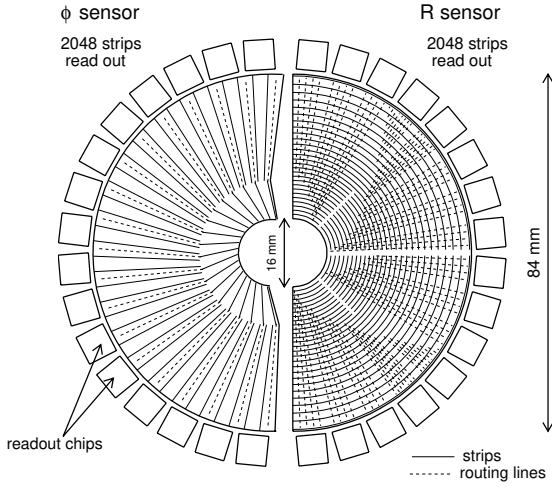


Figure 1.5: Schematic view of a R- and ϕ -measuring sensor. A R-measuring sensor has azimuthal strips at constant radius, whereas a ϕ -measuring sensor has radial strips with a stereo angle between 10° and 20° which is defined at the innermost point of a strip.

The LHCb VELO sensors will be subject to a harsh radiation environment. At the innermost radius this will be dominated by charged particles and will reach levels of about $10^{14} n_{eq}/cm^2$ per year (Fig. 1.2). Due to the $r^{-\alpha}$ dependence of the irradiation, there is a sharp gradient in dose from the inner to the outer radius. The highest radiation levels occur at the place where the sensors have the finest pitch, and the demands on the resolution are greatest. These considerations, combined with extensive prototyping, have led to the choice of n-strip detectors on n-bulk material (n-on-n), with AC coupling and polysilicon biasing. It was verified that an efficient operation of up to three years is ensured. It should be noted that because of the strong non-uniform irradiation and the chosen $r\phi$ -geometry, only the innermost strips of the most irradiated sensors will lose efficiency after this time. It is expected that the sensors have to be replaced every three years.

The basic parameters of the sensors are listed in Table 1.2.

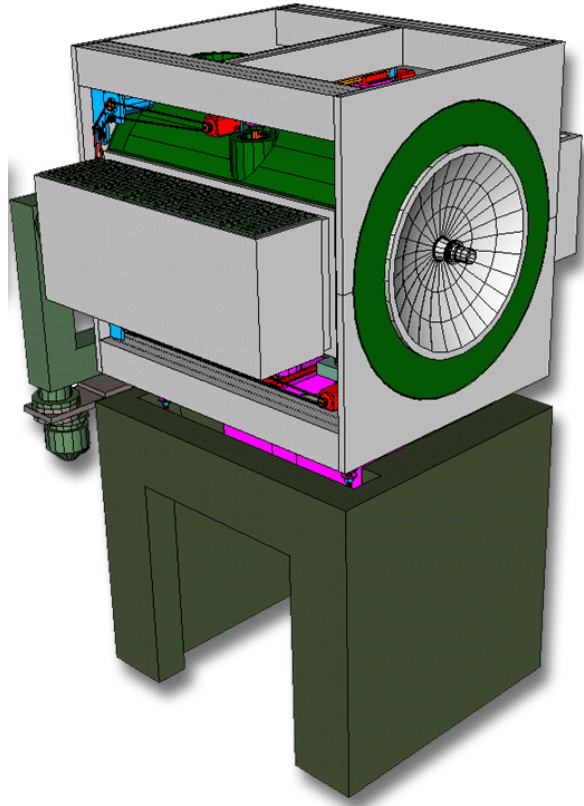


Figure 1.6: VELO vacuum vessel on its concrete stand.

The option of using Si-pixels was considered, but was not found to offer any advantage. No gain is expected in terms of resolution. The area covered by each strip is matched to the particle flux such that leakage current will not dominate the noise even after five years of operation. In addition, the channel occupancy is so low that no problems with pattern recognition are anticipated. The drawbacks of using pixels, such as material, cooling, number of channels and increased cost, are not justified in the case of the VELO.

1.2.4 Readout electronics

The readout electronics chain must conform to the overall LHCb readout specifications [5]. Data from the VELO system are used in the L1 trigger.

Analog rather than binary readout has been chosen since it provides a better hit reso-

lution [6] and allows for better monitoring and control of effects due to the very non-uniform radiation damage to the silicon detectors. A total of 128 readout lines will be bonded to a front end chip (Sect. 3.3.2). Two radiation hard designs are under study, one in the $0.25\ \mu\text{m}$ CMOS, the other in the DMILL technology (Sect. 2.4.1). Both chips accept input data at 40 MHz which are kept in an analog pipeline of $4\ \mu\text{s}$ latency until the L0 decision is received. Then, 32 channels are read out in 900 ns in order to cope with the average L0 accept rate of 1 MHz. The analog data are sent via twisted pair cables to the off-detector L1 electronics situated at 60 m distance in a radiation free environment. The L1 electronics performs synchronization checks, provides the interface to the L1 trigger and performs zero-suppression and cluster finding. Events accepted by the L1 trigger are processed and transferred to the DAQ.

1.2.5 Detector cooling system

Cooling of the detector modules is required since the sensors are operated in a high radiation environment. This is achieved by using a mixed-phase CO_2 cooling system. Besides being an adequate coolant for applications in high radiation environments, CO_2 exhibits excellent cooling properties. In the proposed cooling circuit (see section 3.6 and Ref. [7]), CO_2 is supplied as a liquid and expanded into a number of stainless steel capillaries (one line per detector module) via flow restrictions. The capillaries and flow restrictions are vacuum-brazed to a manifold. The connection to the detector modules is achieved via an aluminium coupler and a soft metal indium joint. A carbon-fibre substrate provides a mechanical and thermal link to the sensors. The total amount of CO_2 in the system is relatively small, of the order of 5 kg. The amount in the tubing located inside the secondary vacuum is less than 100 g. The temperature of the coolant in the capillaries is set by controlling the pressure on the return line (typically 15 bar). In this way, a temperature in

the range of -25 to $+10\ ^\circ\text{C}$ can be maintained with a total cooling capacity of about 2.5 kW ($\approx 50\ \text{W}$ per cooling capillary).

1.2.6 Integration with LHC

The required performance of the LHCb VELO demands positioning of the sensitive area of the detectors as close as possible to the beams and with a minimum amount of material in the detector acceptance. This is best accomplished by operating the silicon sensors in vacuum. As a consequence, integration into the LHC machine is a central issue in the design of the VELO.

A large vacuum vessel (Fig. 1.6), supported by a concrete stand, encloses the complete detector array and support frames. To protect the primary (LHC) vacuum, the detector modules are placed in an aluminium, thin-walled, secondary vacuum container. This aluminium structure also acts as a wake field suppressor and shields the detector modules from the high-frequency fields of the LHC beams (Fig. 1.7 and Fig. 3.12). In this case, the amount of material in front of the silicon detector is mainly determined by the necessity to shield against the RF pickup and not by the requirement to withstand atmospheric pressure. However, the design of the vacuum system should ensure that the pressure difference between the secondary and primary vacuum is never so large as to cause inelastic deformations of the secondary vacuum container. The detectors and thin-walled encapsulations are decoupled from the primary vacuum vessel via bellows and attached to a positioning system. In this way, the detectors can be remotely aligned with respect to the beams, as well as retracted (with the encapsulations) during beam filling. All motion mechanics are placed outside the vacuum. A detailed description of the mechanical design can be found in section 3.4 and Ref. [8].

The LHCb vacuum system consists of three communicating sections, namely the VELO primary vacuum vessel, the LHCb beam pipe and the silicon detector volume. The VELO

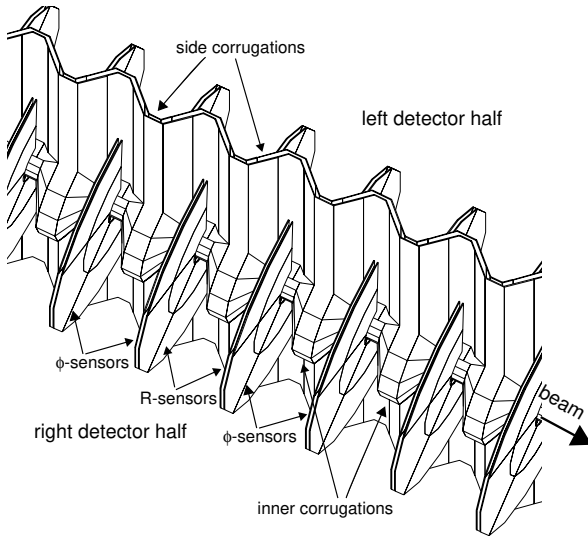


Figure 1.7: Close-up of the secondary vacuum container showing the inside close to the beam (RF shield). The corrugations close to the beam axis are needed to minimize the material seen by tracks before the first measured point. The corrugations at the side allow an overlap between the left and right detector half.

primary vacuum vessel and LHCb beam pipe are integral parts of the LHC primary vacuum system. The LHCb beam pipe extends throughout the complete LHCb detector (length of ≈ 18 m) and its interior will be coated with low activation temperature NEG¹, principally to avoid beam instabilities due to dynamic vacuum effects. The LHCb beam pipe and the VELO vacuum vessel can be baked out in-situ with the detectors removed to about 200°C and 150°C, respectively. On the side of the VELO, the LHCb beam pipe ends with a $\varnothing 76$ cm aluminium window which seals the VELO primary vacuum vessel. The complete VELO vacuum system is further described in section 3.5 and Ref. [10].

Beam bunches passing through the VELO structures will generate wake fields which can affect both the VELO system (RF pick-up, losses) and LHC beams (instabilities). These issues have been addressed in detail [11, 12, 13, 14] and are further discussed in section 2.5.2.

In the design of the VELO, wake field suppression is achieved by enclosing the silicon detector modules in a shielding box made of conductive material (aluminium) and ensuring that a continuous conductive surface guides the mirror charges from one end of the VELO vessel to the other.

Because the VELO constitutes a complex device which must be integrated into the LHC machine vacuum, special attention was paid to the minimization of risk for LHC. A risk analysis was carried out to identify the critical parts of the VELO system [15]. Possible failure scenarios and their consequences for LHC were analyzed to evaluate the risk and, where necessary, to require modifications or precautions and to request a number of tests to be performed before installation at IP8. In particular, based on this analysis, it was recommended that emergency parts are provided to replace, if required, the secondary vacuum containers by a straight cylindrical wake field suppressor, or the complete LHCb beam pipe with cylindrical beam pipes. In this way, one expects the maximum downtime for LHC to be at most two weeks even in the unlikely case of a major vacuum failure.

1.2.7 Alignment

The alignment strategy of the VELO is based on survey during assembly, with the possibility to readjust the individual modules, and measurements with tracks.

The silicon sensors in the individual detector modules will be positioned with a precision of better than $5\ \mu\text{m}$. The position inside the detector halves will be measured before installation with a survey machine and with testbeam data. The final alignment needs to be done with tracks from pp interactions under normal operational conditions, i.e. in vacuum and at -10°C . The feasibility of an alignment with tracks has been demonstrated in test-beam studies. In addition to the overall alignment, a relative alignment of the two detector halves will be done after each change of position, i.e. after each fill of the LHC ma-

¹Non Evaporable Getter pumps [9].

chine.

1.2.8 Material budget

The material which is placed within the LHCb acceptance, due to the different components of the VELO system is discussed in section 3.7. The main contributions come from the RF shield, silicon sensors and the exit window and amount on average to 9%, 5.3% and 1.9% of a radiation length respectively. A detailed study of all the material can be found in Ref.[16]. Special emphasis was put on minimizing the material before the first measured point, which resulted in a corrugated shape of the RF shield (Fig. 1.7).

1.2.9 Detector resolution

The errors on the track parameters arise from the intrinsic resolution of the detectors and from multiple Coulomb scattering, which in turn depends on the thickness of the material in radiation lengths and the momentum of the particle. The errors are magnified by the extrapolation distance from the first measured point to the vertex region and depend to first order on the transverse momentum of the particle (section 4.4).

The error on the primary vertex is dominated by the number of tracks produced in a pp-collision. For an average event, the resolution in the z -direction is $42\text{ }\mu\text{m}$ and $10\text{ }\mu\text{m}$ perpendicular to the beam.

Impact parameter resolutions of $20\text{ }\mu\text{m}$, neglecting the primary vertex contribution, are achieved for tracks with the highest transverse momentum.

The precision on the decay length ranges from $220\text{ }\mu\text{m}$ to $370\text{ }\mu\text{m}$ depending on the decay channel. A lifetime resolution of 40 fs is achieved for the $B_s^0 \rightarrow D_s^- \pi^+$ decay channel, which allows a 5σ measurement of Δm_s up to 54 ps^{-1} after one year of data-taking.

1.3 Evolution since the Technical Proposal

Since the LHCb Technical Proposal [1] a major effort went into the study of prototype detectors after heavy irradiation and the design of a realistic vacuum system. Changes compared to the TP are:

- **Sensors:** In the TP, we proposed six sensors of 60° coverage each per station. By reducing the outer radius of a sensor from 60 mm to 42 mm, it was possible to reduce the number to two sensors each covering 182° . As a consequence, the number of stations was increased from 17 to 25. The inner radius was reduced from 10 mm to 8 mm.
- The **L1 electronics** were moved behind the shielding wall away from the high radiation environment.
- **Vacuum/Mechanics:** A complete system design was carried out. This includes a design of the vacuum vessel, motion and positioning mechanics, thin-walled structures for RF screening, systems for cooling, vacuum, monitoring and control. Finite element analysis (FEA) was performed for the vessel and other components (exit window, cooling capillaries, thin-walled detector encapsulation). Extensive prototyping was carried out on critical items, such as the thin-walled structures, vacuum protection devices, large rectangular bellows and the cooling system. The new design allows baking out of the primary vacuum surfaces and provides easy access to the silicon sensors.
- **Detector optimization:** Detailed studies were carried out of many different detector designs to optimize the physics performance. The layout was finalized with 25 stations, with the arrangement as shown in Fig. 1.3, and with the shape of the corrugations in the RF

shield (Fig. 1.7) optimized for minimizing multiple scattering.

1.4 Structure of this document

This Technical Design Report is intended to be a concise but self-contained description of the VELO system. Further details can be found in the technical notes, which are referenced throughout.

In Chapter 2 an overview is given of the results obtained in the laboratory and test-beam using prototypes, which give confidence that the expected performance will be achieved. The technical design of the detectors is presented in Chapter 3. The performance of the VELO system as obtained from simulation is discussed in Chapter 4. The issues of project organization, including the schedule and cost, are discussed in Chapter 5.

2 Summary of R&D and test of prototypes

2.1 Silicon

The complexities of the LHCb VELO sensor design arise from the varying strip lengths, the double metal layer, and the need for regions of very fine pitch. The first aim of the prototyping programme was to ensure that the sensor gives the expected performance in the context of the chosen design. The second aim was to check that this is maintained after irradiation. It should be noted that the most stringent requirements on the sensor performance are at low radius, where there is both the finest pitch and the highest irradiation (see section 4.3). The strong non-uniform nature of the irradiation is another special consideration for the LHCb VELO. The test-beam programme has also given the opportunity to test the performance of the $r\phi$ -geometry in terms of the alignment and triggering requirements for LHCb.

The global performance of a sensor can be characterized with the following inter-related parameters:

- **Signal to Noise Ratio:** In order to ensure effective trigger performance even after irradiation, the LHCb VELO aims for an initial signal to noise ratio, S/N , of more than 14 [17].
- **Efficiency:** The goal for the efficiency is that it should be above 99% for $S/N > 5$.
- **Resolution:** Typical resolutions which can be achieved are about $3.6\mu\text{m}$ for 100mrad tracks and $40\mu\text{m}$ strip pitch. The resolution should not be degraded

by the irradiation nor by any aspect of the sensor design.

There are various constraints coming directly from the strip layout which can affect these parameters. The noise is affected by the length of the strips and routing lines. The size of the signal can be affected by the presence and geometry of the double metal layer, or the capacitive coupling between strips. Other constraints come from the detailed technical design, e.g. the strip capacitance will be affected by the thickness of dielectric separating the two metal layers, the noise is affected by the strip resistance, and so on. After irradiation the signal might be limited by the breakdown voltage, or the onset of noise at a particular bias voltage. The prototyping programme should establish that the design performs in the expected manner, both before and after irradiation.

In addition there are various silicon technology choices which can be made for a given strip layout.

2.1.1 Design parameters

The most important issues affecting the choice of silicon technologies were investigated with dedicated LHCb prototyping, as described in the following sections. The results were combined with knowledge available from the silicon literature, in order to make the best choices for the LHCb VELO. The principal considerations are listed here.

Thickness

The voltage required to deplete the sensor is proportional to the square of the thickness.

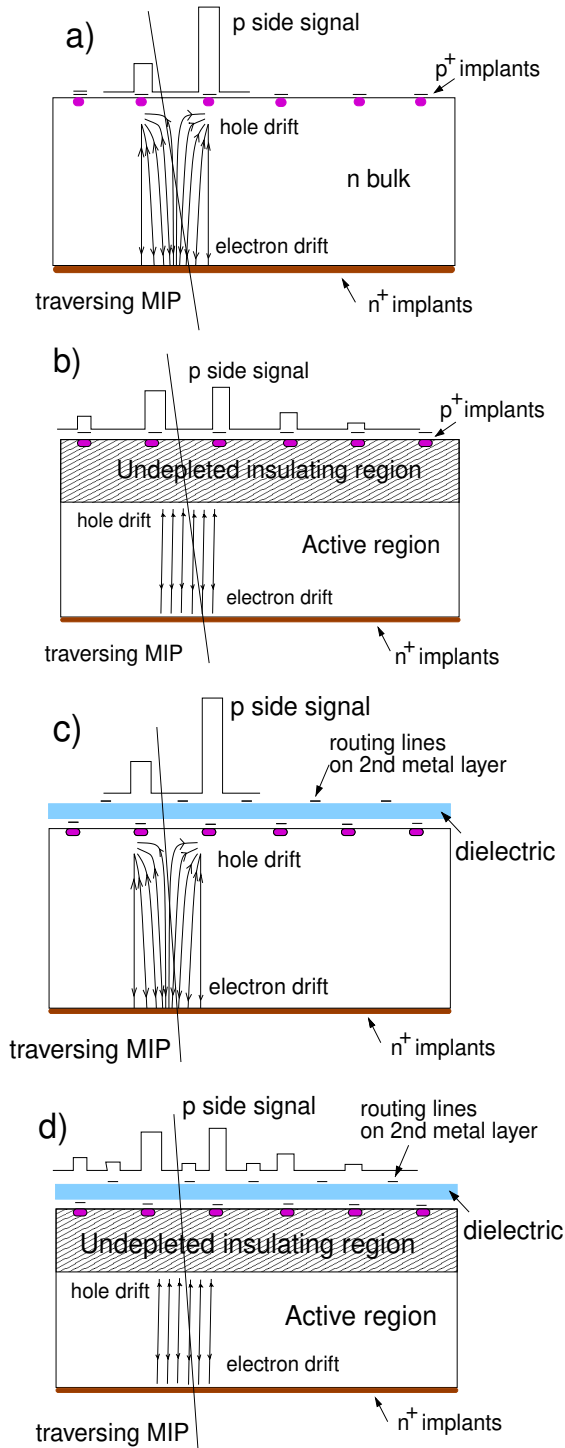


Figure 2.1: Cluster shapes for the depleted and underdepleted cases for a simple segmented *p-on-n* sensor, (a) and (b), and for a sensor with a double metal layer, (c) and (d). At full depletion the charge is focused on the diodes, while at underdepletion the clusters spread (b) and lose charge to the double metal layer (d).

Given the large voltages needed to deplete irradiated sensors, thin silicon is an advantage. In addition, if the irradiated sensor is only partially depleted, then the thinner the sensor, the greater the recovered charge, due to Ramo's theorem [18]. Thin sensors also have less bulk current, in proportion to their thickness, so the risk of thermal runaway is reduced. On the other hand, for a fully depleted sensor the total amount of charge produced is proportional to the thickness, so a thick sensor will start with a better S/N, and will stay this way as long as it is fully depleted.

The cluster resolution is improved by the sharing of charge between strips due to diffusion. In this respect thick sensors are an advantage given the greater diffusion width of the deposited charge.

Thin sensors have the overall advantage that the multiple scattering of tracks is reduced, which is particularly helpful for the L1 trigger.

Segmentation

There is a choice to be made between segmentation on the p- (*p-on-n*) or n- (*n-on-n*) side. This has consequences for the way the detector operates when underdepleted, the operating conditions where micro-discharge noise may occur, and the fabrication possibilities. These points are discussed in turn.

Underdepleted operation: If there is a risk that the sensor will be operated in underdepleted mode after irradiation, then there can be disadvantages for a *p-on-n* design, due to the fact that the irradiated sensor depletes from the n-side. The consequences for the cluster shapes produced by a traversing MIP are illustrated in Fig. 2.1. When the sensor is fully depleted, as in Fig. 2.1(a), the field lines are focused onto the diodes, and the cluster is narrow. When it is partially depleted, as in Fig. 2.1(b), the undepleted region close to the p-strips acts as an insulating layer, and a signal is induced over a number of strips.

This charge spread leads to a loss of efficiency and resolution, and is particularly

dangerous for fine pitch sensors [19, 20]. A double metal layer can cause an additional charge loss, as illustrated in Fig. 2.1(c) and (d). These effects are not present for the *n-on-n* design, where the depleted layer is on the same side as the strips.

Micro-discharge noise: Micro-discharge noise [21] is a reversible phenomenon of random pulse noises around the edge of strips for bias voltages exceeding a certain value. It is visible in the noise and the leakage current, and can place a limit on the bias voltage which can be applied to the sensor. After irradiation the high field regions which cause micro-discharge noise are found close to the *n*-strips [22] and so for an *n-on-n* design micro-discharge noise will occur at a lower voltage than for the corresponding *p-on-n* design. The situation can however be improved with field plates and rounded strips [23]. Before irradiation the situation is reversed, and the turn-on for micro-discharge in the *p-on-n* design will be at a lower voltage. In the LHCb VELO case, there is non-uniform irradiation across the sensor, but only one voltage will be applied. This bias voltage must be tuned to optimize the charge collection efficiency and noise performance in all regions, which may result in areas of underdepletion. From this point of view, *n-on-n* is considered a safer design, as it gives a more reliable performance in situations of underdepletion, due to the reasons discussed in the previous paragraph.

Fabrication: *p-on-n* sensors have the advantage that the single-sided processing is easier, and it is possible to have a finer pitch due to the fact that there is not the need to separate the strips via a mechanism such as *p*-stops. However, it is possible to have a fine pitch for *n-on-n* sensors with the use of such techniques as *p*-spray [24].

The segmentation choice is considered critical for LHCb, where the design includes fine pitch and double metal, and it has been investigated extensively in the prototyping.

Oxygenation

Recent results from ROSE [25, 26] indicate that there is an advantage to be gained by using oxygenated silicon wafers. It was found that after irradiation the oxygenated samples could be fully depleted with bias voltages which were both lower and more predictable than for the standard samples. The advantages are associated particularly with irradiation by charged particles, which corresponds to the situation in the LHCb VELO (see section 4.3).

Cryogenic operation

From considerations of annealing and leakage current after irradiation, the sensors are expected to operate at a temperature of -5°C (see section 3.1.1). The option of going to cryogenic (liquid nitrogen) temperatures was also investigated. A possible advantage of cryogenic operation is that due to trap filling the depletion voltage of an irradiated sensor is lowered. If the sensor is operating at underdepletion, the cryogenic temperatures can make it more efficient and improve the resolution [19]. However this is not a preferred solution for LHCb due to the fact that the recovery is lost after a time interval of the order of minutes, and a very complex procedure would have to be imagined to maintain the performance for long time periods [19, 27].

Cryogenic operation also has an advantage in terms of lower leakage current, but at the VELO operating temperature the current is not expected to be a dominant source of noise. After 3 years of operation the most irradiated strip, operated at -5°C , is expected to have a noise contribution from the current of 100 electrons [28], which is less than 10% of the baseline noise.

2.1.2 Prototype designs

This section summarizes the prototype designs which have been tested for the LHCb VELO. There were three different types of geometrical layouts tested.

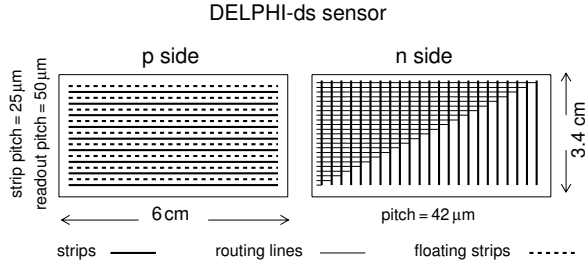


Figure 2.2: Schematic of the DELPHI-ds prototype.

The **DELPHI-ds** prototype, manufactured by Hamamatsu¹ is illustrated in Fig. 2.2. It is a double sided sensor with straight, orthogonal strips. The main purpose of this prototype was to use an existing design to test the performance of *p-on-n* and *n-on-n* fine pitch layouts after non-uniform irradiation, in situations of full depletion and under-depletion, and at cryogenic temperatures.

The **PR01-R** and **PR01- ϕ** prototypes, manufactured by Hamamatsu, have a radial and azimuthal strip geometry which is close to the final LHCb-VELO design, the main differences being that the sensors cover 72° only, and the geometry of the double metal layer is different. These prototypes are of *n-on-n* design, with individual p-stops, and with a thickness of $300\text{ }\mu\text{m}$. The strip layout and the pitches achieved are illustrated in Fig. 2.3; further details may be found in Ref. [29]. The first purpose of these prototypes was to be able to carry out extensive tests of the non-irradiated design, to confirm that the $r\phi$ -geometry of the sensors is suitable for the alignment, precision and vertexing requirements of the LHCb-VELO. The second purpose was to undertake resolution and efficiency measurements on irradiated *n-on-n* prototypes.

The **PR02-R** and **PR02- ϕ** prototypes, manufactured by MICRON² have a radial and azimuthal geometry and an angular coverage of 182° . They were manufactured in thicknesses of 150, 200 and $300\text{ }\mu\text{m}$ and included some pro-

¹Hamamatsu Photonics K.K., 325-6, Sunayama-cho, Hamamatsu City, Shizoka Pref., 430-8587, Japan.

²Micron Semiconductors, 1 Royal Buildings, Marlborough Road, Lancing, Sussex, BN15 8UN, UK.

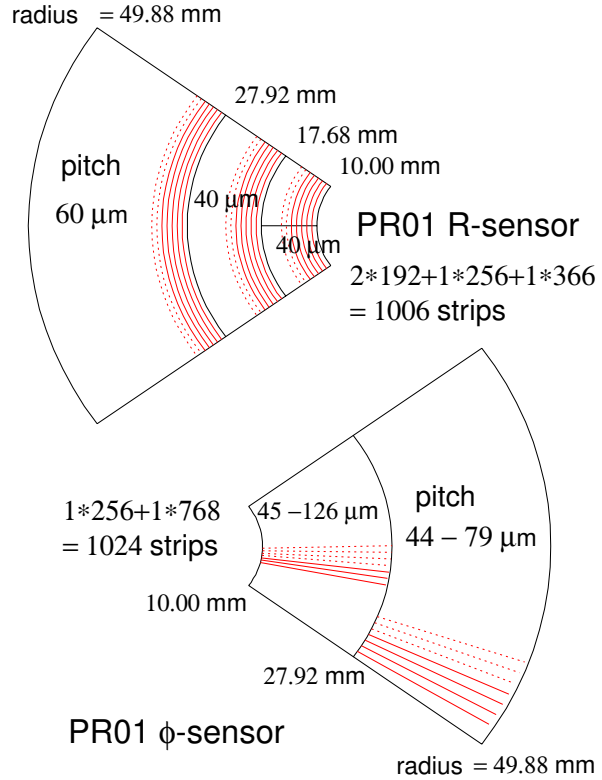


Figure 2.3: Schematic of the Hamamatsu PR01-R and PR01- ϕ prototypes. The routing lines are not shown.

types with oxygenated silicon. The design is *p-on-n* and the minimum strip pitch $24\text{ }\mu\text{m}$. The purpose of these prototypes was to test the performance of the irradiated *p-on-n* design, in particular at fine pitch. The strip layout of the prototypes is illustrated in Fig. 2.4. It is very close to the final LHCb-VELO design (further details may be found in Ref. [29]).

The principal characteristics of the different prototypes are summarized in Table 2.1.

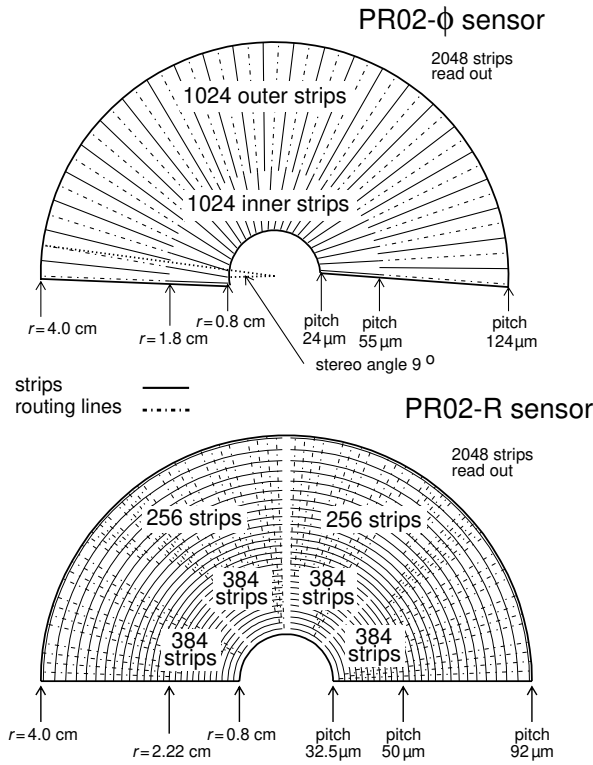
2.1.3 Prototype manufacture

Of the prototypes described above, only the DELPHI-ds was pre-existing. The PR01 prototypes were developed together with Hamamatsu and delivered in 1998. The PR02 masks were designed at Liverpool University, using the CADENCE³ program, and the sensors

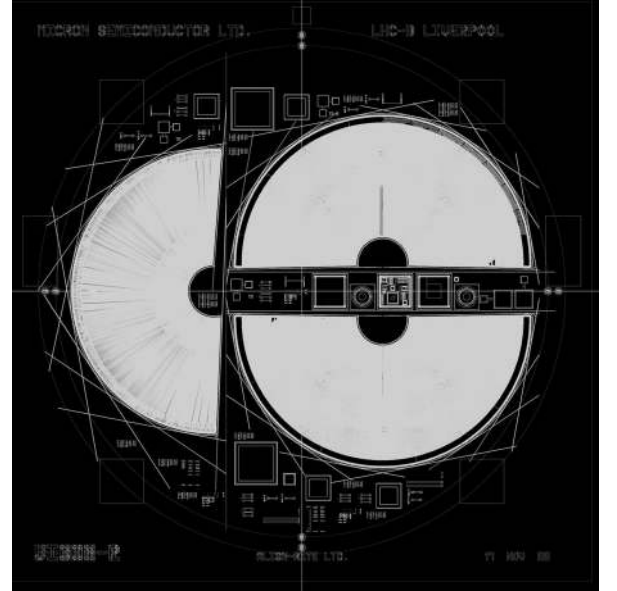
³Cadence Design Systems, Bagshot Road, Bracknell, Berkshire, UK.

	DELPHI-ds	PR01-R	PR01- ϕ	PR02-R	PR02- ϕ
Manufacturer	Hamamatsu	Hamamatsu	Hamamatsu	MICRON	MICRON
segmentation	double-sided	n -on- n	n -on- n	p -on- n	p -on- n
Pitch (μm) p	25			42.5 \rightarrow 92	24 \rightarrow 124
Pitch (μm) n	42	40,60	45 \rightarrow 126		
thickness (μm)	300	300	300	150,200,300	150,200,300
dimensions (cm)	3 \times 6	0.8 < R < 5.0	0.8 < R < 5.0	0.8 < R < 4.0	0.8 < R < 4.0
angular coverage	—	72°	72°	182°	182°
strip length (cm)	p side: 6 n side: 3	0.63 \rightarrow 6.3	1.8,2.2	0.62 \rightarrow 6.3	1.0, 2.2
double metal	p side: no n side: yes	yes	yes	yes	yes
n-separation	p-grid	p-atolls	p-atolls	—	—
non-oxygenated	yes	yes	yes	yes	yes
oxygenated	no	no	no	yes	yes

Table 2.1: Characteristics of the prototype sensors.

Figure 2.4: Schematic of the MICRON PR02- ϕ and PR02-R prototypes.

were manufactured at MICRON. The mask design layout on the 6-inch wafer is illustrated in Fig. 2.5. The manufacturing process at MICRON was carried out on a best effort R&D basis, with the procedures being continually revised during the delivery throughout 2000.

Figure 2.5: PR02 wafer layout. Two R-sensors and one ϕ sensor are fitted onto the wafer, together with a series of test structures.

2.1.4 Prototype tests

The sensors underwent various tests, described in the following sections, including:

- Laboratory tests of the unbonded silicon.
- Large scale evaluation in a test-beam of 120 GeV/c muons and pions, to test the suitability of the $r\phi$ -geometry for triggering and tracking, using slow VA2 [30] electronics.

Name	Type	Thickness μm	Oxygenation $\times 10^{17} \text{ atoms/cm}^3$	Maximum Irradiation $\times 10^{14} p/\text{cm}^2$	Tests
D-ds112	DELPHI-ds	310	None	3.5	TMX6, LAB
h1-R, h2-R, h4-R, h6-R, h7-R	PR01-R	300	None	None	TVA, LAB
h3- ϕ , h5- ϕ , h8- ϕ h9- ϕ , h11- ϕ , h12- ϕ	PR01- ϕ	300	None	None	TVA, LAB
h10-R	PR01-R	300	None	None	TSCT, LAB
h-13-R	PR01-R	300	None	3.4	TSCT
h-14- ϕ	PR01- ϕ	300	None	4.1	TSCT
1976-21-b	PR02-R	300	None	None	LAB
1968-17-c	PR02-R	300	2.5	4.8	LSCT, LAB
1832-9-a	PR02- ϕ	200	None	10.4	TSCT, LAB

Table 2.2: DELPHI-ds, PR01 and PR02 prototypes whose tests are described in this section. The tests are coded as follows: TVA: Test-beam evaluation with VA2 electronics, TMX6: Test-beam evaluation with MX6 electronics, TSCT: Test-beam evaluation with SCT128A electronics, LSCT: Laser evaluation with SCT128A electronics, LAB: Laboratory test.

- Test-beam evaluation of non-irradiated silicon bonded to fast SCT128A [31] electronics clocked at 40 MHz.
- Non-uniform irradiation in a 24 GeV proton beam followed by bonding to slow (MX6 [32] or VA2) or fast (SCT128A) electronics and evaluation both in the laboratory and in a test-beam.

The list of prototype sensors for which detailed tests are discussed in this section is given in Table 2.2.

2.1.5 Laboratory tests

PR01 Prototype

12 PR01 prototypes (h-1 to h-12) underwent laboratory tests [33] at CERN. The depletion voltage was measured from the C-V curve, the resistance of the set of strips to the back plane was checked, and the current versus voltage was measured up to 200 V. All sensors satisfied the parameters given in Table 2.3. After bonding to VA2 hybrids the mean number of dead channels was 0.8%.

PR02 Prototype

A total of 35 PR02 prototype sensors were delivered from MICRON. The sensors covered a range of thicknesses, with 2, 10 and 23 detectors with thicknesses of 150, 200 and 300 μm respectively, and had different oxygenation levels, with 11 and 3 detectors oxygenated to levels of 2.5 and $1.0 \times 10^{17} \text{ atoms/cm}^3$ respectively. The pre-irradiation depletion voltages were measured using a C-V scan. The values measured for some different sensor types are illustrated in Fig. 2.6. The pre-irradiation depletion voltages are higher for the oxygenated samples than for the non-oxygenated ones. The resistance of the routing lines was measured on two sensors and found to be $\approx 23 \Omega/\text{cm}$.

The breakdown voltages were determined by slowly increasing the voltage until the current reached a maximum allowed value of 15 μA . A total of 16 sensors were found to have breakdown voltages above 400 V, including both the oxygenated and non-oxygenated samples, and both of the thinnest (150 μm) sensors. The fraction of bad strips was measured by probing the coupling capacitance of each strip. A typical output of such a scan is shown in Fig. 2.7 for the PR02-R sensor 1976-

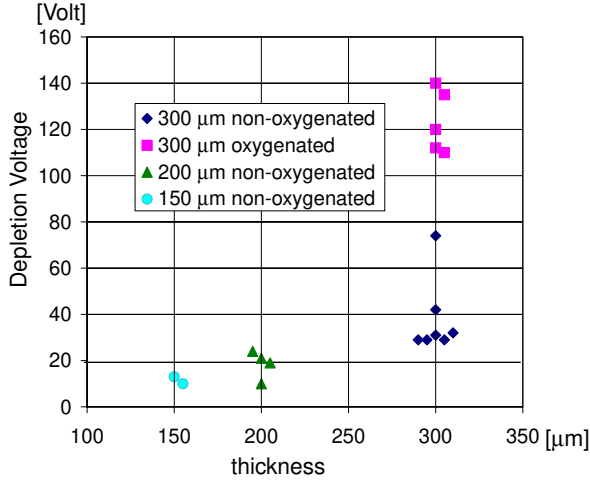


Figure 2.6: Depletion voltages on different sensor types.

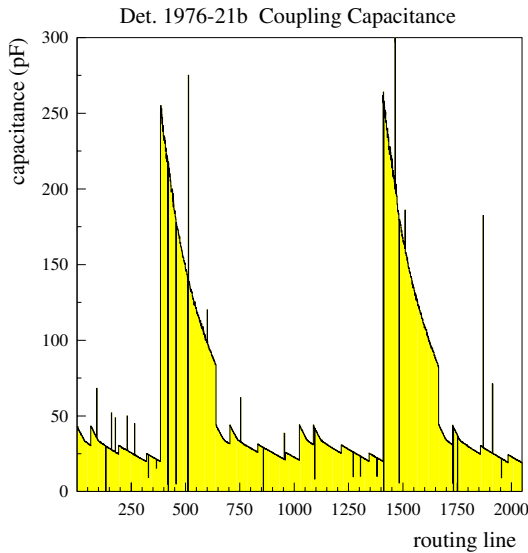


Figure 2.7: Coupling capacitance scan on a PR02-R prototype.

21-b. There is a wide variation in coupling capacitance seen due to the variations in the length and width of the strips. The number of strips which lie outside the normal distribution, due to shorts or open lines, was measured for each sensor. In general, a better performance was found for the 300 μm thick samples. The number of sensors with more than 98% good strips was 14 and the number of these which had a breakdown voltage greater than 400 V was 10.

Depletion Voltage	$< 70 \text{ V}$
Strip-Backplane resistance	$> 300 \text{ M}\Omega$ (at V_{dep})
Current @ $V_{\text{bias}} = 200 \text{ V}$	$< 0.5 \mu\text{A}$
Routing line resistance	$\sim 17 \Omega/\text{cm}$

Table 2.3: Laboratory measured parameters satisfied by all 12 tested PR-01 prototypes.

2.1.6 Test-beam results on non-irradiated sensors

A set of 12 PR01 sensors were equipped with VA2 electronics and used in three different large-scale configurations in 1998, 1999, and 2000, to check different aspects of the R& ϕ design. The 1998 configuration is illustrated in Fig. 2.8 and a photograph of the set up of the silicon sensors is shown in Fig. 2.9. The sensors were arranged in 3 $r\phi$ measuring planes behind a series of thin Cu targets in a beam of pions of 120 GeV momentum. The distance between the targets was designed to be similar to the mean B decay length at the LHC. This system allowed a test of the alignment, track reconstruction, primary vertex reconstruction and trigger algorithm with a similar geometry to that of the final VELO. In 1999 the targets were removed and the telescope was rotated in the beam line in order to make a detailed study of the sensor resolutions as a function of track angle.

Common mode and noise analysis

Due to the complex geometry of the LHCb sensors, it is expected that any pick-up due to HV or environmental variations will vary significantly over the surface of the sensor. In the test-beam environment it was shown [33] that by grouping channels into regions with smoothly varying strip and routing line lengths, it is possible to parameterize and suppress the common mode noise. A similar procedure will be applied in the final VELO. With a careful analysis of the noise, taking into account the parameters described in section 2.1.5, the capacitances of the strips

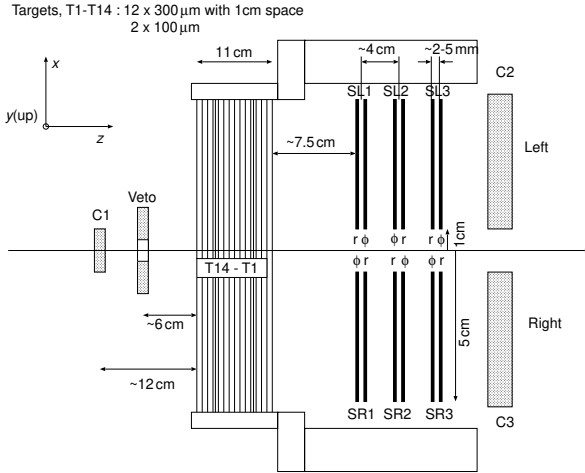


Figure 2.8: 1998 Test-beam setup.

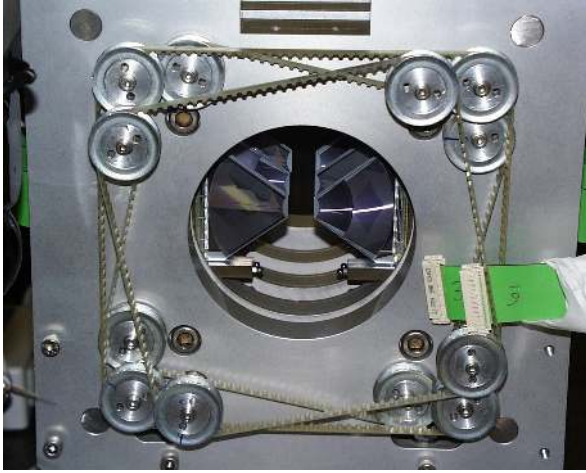


Figure 2.9: 1998 PR01 test-beam telescope.

were measured to be 3.9 pF/cm for the diodes and 3.2 pF/cm for the routing lines, for a geometry corresponding to PR01-R or PR01- ϕ . These values predict a likely range of capacitances for the final VELO R sensor design of 13 – 26 pF. The final ϕ detector is expected to have lower capacitances due to the different arrangement of the routing lines.

Track fitting and alignment

The track parameters were determined in an iterative procedure by approximating locally the circular strips by a straight line [34]. The positions of all sensors were measured using a microscope and a POLI machine (described in

Ref. [35]) before the test-beam. The alignment was performed using MINUIT [36] to minimize the χ^2 of the track residuals. The detector halves were aligned relative to each other using tracks originating from a common vertex. After the alignment the scatter of the residuals in the central plane of sensors was reduced to less than 1 μm [37]. Several important implications for the LHCb VELO alignment can be drawn from this study, including:

- Various alignment parameters and combinations of parameters are only loosely constrained by tracks. An analysis of these provides input into determining the mechanical precision to which the VELO must be constructed.
- The current alignment procedure must be speeded up for LHCb running, by more extensive use of analytic methods.

These topics will be addressed in future test-beam analysis and in simulation. After the MINUIT alignment the two-track vertices measured with the test-beam data were found to have a resolution of 230 μm , which when extrapolated to the conditions at the LHC would imply a primary vertex resolution of 70 μm , matching the requirement of the L1 trigger [38]. The distribution of reconstructed vertices is illustrated in Fig. 2.10.

Triggering

The test-beam data were also used to test various triggering algorithms in a realistic environment [39, 3]. The feasibility of triggering on low multiplicity displaced vertices was demonstrated, and conclusions were drawn on the alignment tolerances.

Resolution

An important motivation for the test-beam measurements was that of testing the resolution of the LHCb prototype design for a range of pitches and angles. In the LHCb VELO tracks from B-decays will cross the R sensors at typical angles to the strips of 80 mrad, and the

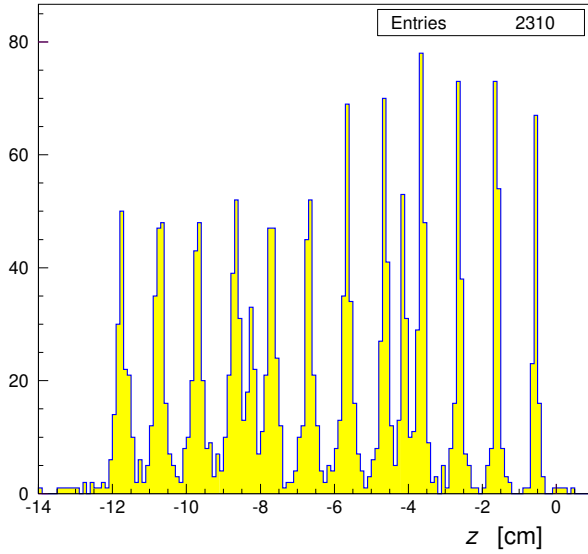


Figure 2.10: Reconstruction of primary vertices in the 1998 test-beam setup.

pitch	track angle	resolution
40 μm	80 – 120 mrad	3.6 – 3.9 μm
60 μm	> 200 mrad	4.0 – 4.6 μm

Table 2.4: Sensor resolution for two different pitches for the track angles giving best precision.

resolution is expected to benefit from charge sharing. As the track angles are roughly parallel to the ϕ strips this is not the case for the ϕ sensors.

In 1999 a dedicated test-beam run was performed with the telescope placed at varying angles in the beam. The sensor resolution was studied as a function of incident angle [40]. The best resolutions achieved in the PR01-R sensor, which had two different pitches, are given in Table 2.4. It was shown that the charge sharing for angled tracks leads to a strong variations in the resolution, as illustrated in Fig. 2.11.

The PR01- ϕ sensors, which have pitches varying continuously from 45 μm to 126 μm , were used to study the resolution as a function of pitch for perpendicular tracks [41]. A linear dependence was found, with agreement with the PR01-R sensors at 60 μm pitch. For the largest pitches the resolution is close to bi-

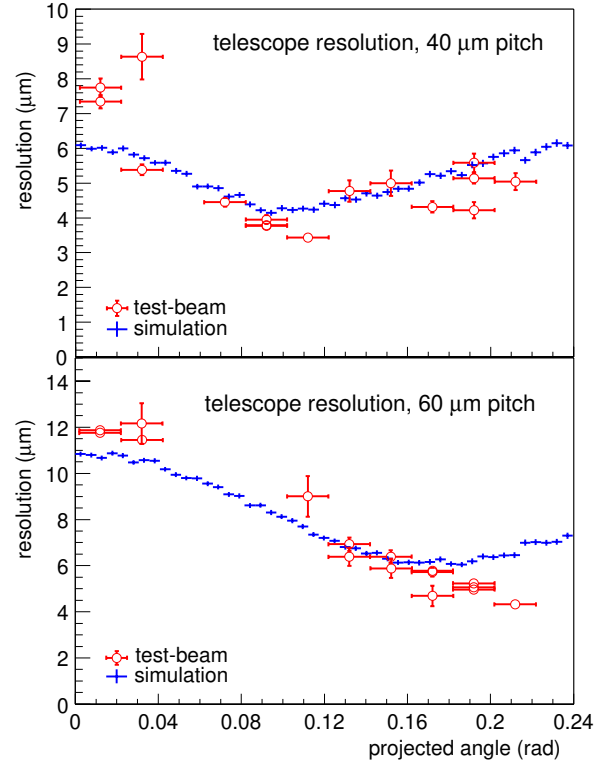


Figure 2.11: Resolution as a function of track angle, as measured from the test-beam data for PR01-R sensors, and compared with the full simulation

nary, i.e. $\text{pitch}/\sqrt{12}$, whereas for the 45 μm region there is significant charge sharing and the resolution is improved by a factor 2.

The results from the test-beam provide important input to the simulation of the charge collection process in the LHCb VELO silicon detectors. The modified simulation which will be used takes into account the charge distribution with full Landau modelling, lateral diffusion of charge carriers, knock-on electrons (δ rays) and charge sharing between strips due to capacitive coupling. The simulation was tuned to the test-beam data using a single free parameter, the fraction of two strip clusters for perpendicular tracks. The agreement between the improved model and the test-beam data is illustrated in Figs. 2.11 and 2.12.

SCT128A performance

The PR01 and PR02 prototypes were also used in the test-beam to evaluate the SCT128A per-

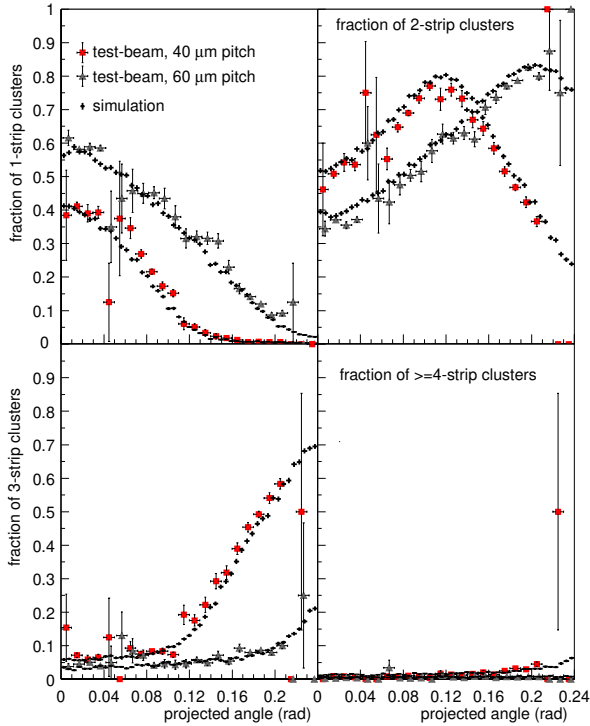


Figure 2.12: Simulated fractions of 1, 2, 3, and n -strip ($n \geq 4$) clusters versus track angle for two different strip pitches, for data and simulation.

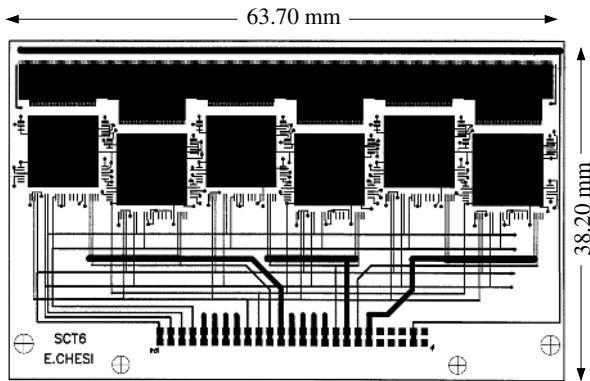


Figure 2.13: Layout of the 6-chip hybrid.

formance. For this purpose, and for testing the irradiated detectors, specially designed fan-ins and hybrids were fabricated. The fan-ins were manufactured on glass (1999 test-beam) and on ceramic (2000 test-beam). Two hybrid designs were used, which could accommodate 3 or 6 chips. The layout of the 6-chip hybrid is illustrated in Fig. 2.13.

The best S/N measured with the SCT128A and a $300\text{ }\mu\text{m}$ thick detector was 21.5. The re-

sults of the evaluation of the SCT128A pulse-shape are discussed in section 2.4.1.

2.1.7 Irradiation procedures

For the LHCb VELO prototyping a non-uniform irradiation was used. As the radiation damage will be dominated by charged particles, an irradiation in the 24 GeV proton PS beam was appropriate. The sensors were stationary throughout the irradiation with either a perpendicular or horizontal orientation with respect to the beam. The beam profile was measured to be a gaussian of a width of $6.1 \pm 0.3\text{ mm}$, hence a less irradiated region was always contained within the sensor. The dose was monitored during the irradiation using secondary emission counters, and was measured after the irradiation was finished by measuring the activity of small pieces of pure Al placed in front of and behind the sensor. As an example, Fig. 2.21 shows a schematic of the irradiation of sensor 1832-9-a. After the irradiation the sensor was equipped with electronics allowing areas from both the irradiated and the non-irradiated sides to be read out. More details about the irradiation can be found in Ref. [42]. The sensors were fully beneficially annealed after the irradiation, with the consequence that they were tested in a condition where a dose of $2 \times 10^{14}\text{ p/cm}^2$ 24 GeV protons corresponds to approximately one year of running for the innermost part of the VELO sensors.

2.1.8 Test-beam results on irradiated sensors

In the year 2000 the test-beam setup was modified to be suitable for testing irradiated sensors equipped with fast electronics. A cold box flushed with nitrogen was placed behind the telescope. Behind this box a second telescope was installed, consisting of 3 sensors, placed at angles to optimize the resolution. The trigger was provided by the coincidence of two scintillators. One of the telescope sensors was equipped with fast SCT128A electronics, so in the case of multiple track events the correct in-time track could be identified. A photograph of

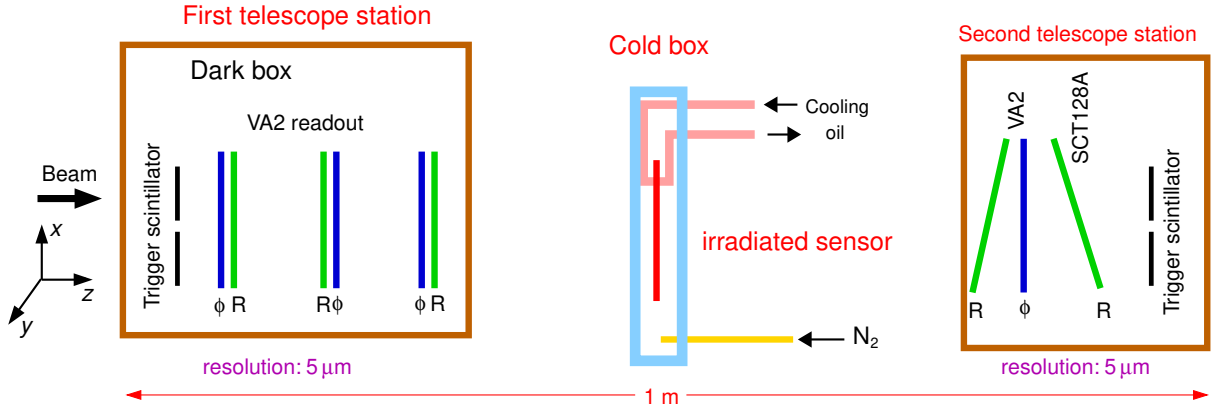


Figure 2.14: 2000 test-beam setup in the X7 beam line. 8 non-irradiated LHCb PR01 prototype sensors are used for precise beam position measurements, one SCT128A equipped sensor is used to identify the in-time tracks, and precise timing information is given by scintillator counters.

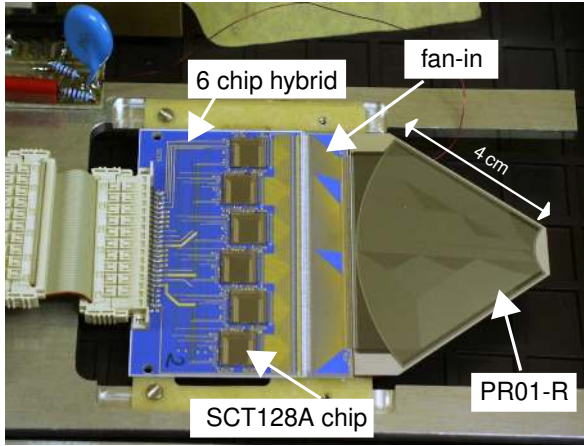


Figure 2.15: The photograph shows one non-irradiated detector equipped with 6 SCT128A-chips used to identify the in-time tracks and characterize the SCTA performance.

the sensor fully equipped with fan-in, hybrid, and SCT128A chips, can be seen in Fig. 2.15. The overall test-beam setup is illustrated in Fig. 2.14.

DELPHI-ds prototype

The purpose of the test on the DELPHI-ds prototype was to investigate the resolution of a double sided fine pitch sensor after irradiation, operated at cryogenic temperatures [19]. It was demonstrated that after irradiation there is a dramatic difference between the p-side and the n-side. The p-side degrades in resolution

as the charge collection falls off due to underdepletion after irradiation. However, under the same conditions the n-side clusters remained well focused. The results are shown in Fig. 2.16. With an empirical simulation it was demonstrated that the resolution degradation is more significant for a fine pitch sensor, such as the VELO sensors. The cryogenic operation was shown to be helpful immediately after biasing the sensor, but degrades after a period of time of the order of 30 minutes [27]. The irradiation of the sensor was non-uniform, and it was shown that in the regions where there was a transverse field due to rapidly changing effective doping characteristics the resolution was not altered.

PR01 prototypes

Two PR01 prototypes, h-13-R and h-14- ϕ , were irradiated to levels of $3.4 \times 10^{14} p/cm^2$ and $4.1 \times 10^{14} p/cm^2$ respectively and evaluated in the test-beam. We describe here the results of the tests on the h-14- ϕ sensor, for which the best statistics were collected. A photograph of the sensor equipped with overlapping 3-chip SCT128A hybrids is shown in Fig. 2.17.

A total of 11,000 tracks were accumulated traversing this sensor and used to show that the most irradiated region was fully operational, with a depletion voltage of 220 V [43]. The clusters were fully focused, hence giv-

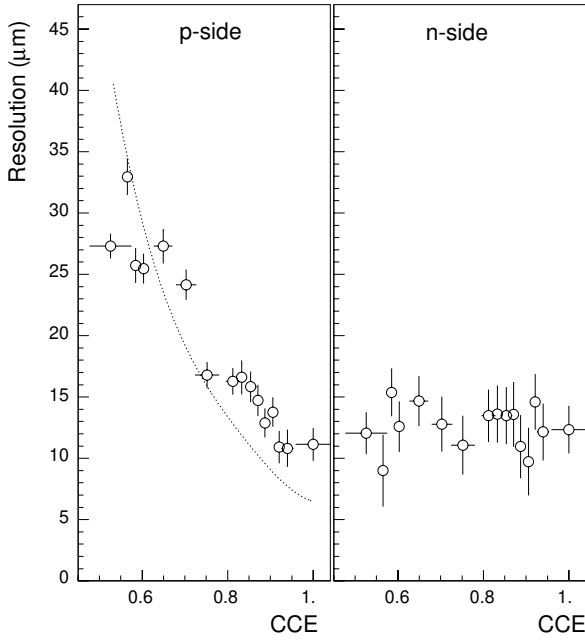


Figure 2.16: Resolution measured on the DELPHI-ds prototype, as a function of charge collection efficiency, for the p- and n-sides. The line is the result of an empirical simulation.

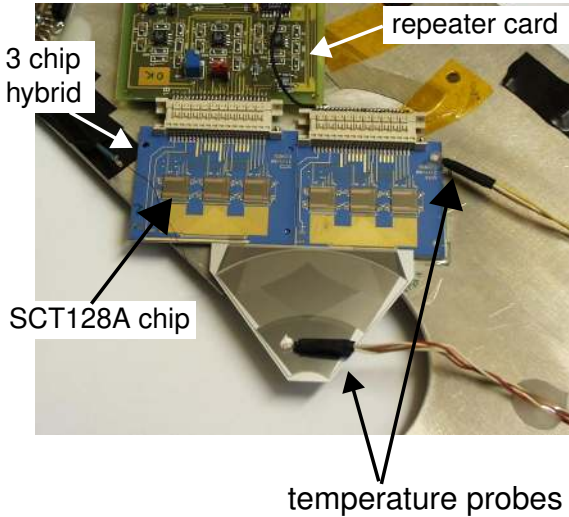


Figure 2.17: Photograph of the PR01 h-14- ϕ prototype equipped with SCT128A hybrids for evaluation in the 2000 test-beam. A temperature probe can be seen on the tip of the sensor.

ing the optimum resolution, both in the cases when the sensor was fully depleted and under-depleted. The efficiency, defined as the probability to find a cluster with a S/N greater than a certain cut within $200\,\mu\text{m}$ of a traversing

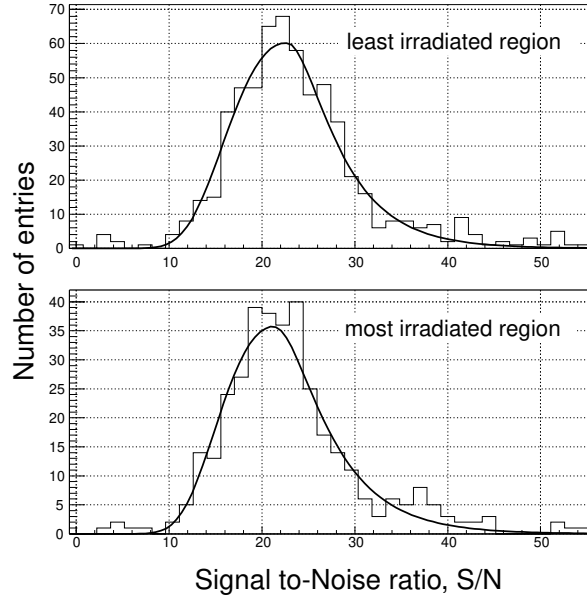


Figure 2.18: S/N measured in the PR01- ϕ prototype, for the least irradiated (upper plot) and most irradiated (lower plot) regions. The most probable value is 21.5.

track, is illustrated in Fig. 2.19, for three different S/N cuts. Even when the detector is underdepleted, the efficiency varies only slowly. The most irradiated area had a full depletion voltage of about 220 V, however with the bias voltage at 50 V the efficiency to reconstruct clusters with a S/N greater than 5 was already greater than 97%. The S/N distribution, measured by summing the charge on the strips around the track intercept, is shown in Fig. 2.18, for the most irradiated and least irradiated regions, at full depletion. The measured S/N was 21.5. The results show that the *n-on-n* design will survive for at least 2 years in LHCb conditions with negligible deterioration. Due to the safety factor given by the fact that the sensor appears fully efficient even when at $\sim 40\%$ underdepletion, 3-4 years operation could be envisaged.

PR02 prototype

The PR02 sensor 1832-9-a was irradiated non-uniformly to a maximum level of $10 \times 10^{14}\,\text{p/cm}^2$ and equipped with SCT128A electronics on both the irradiated and non-

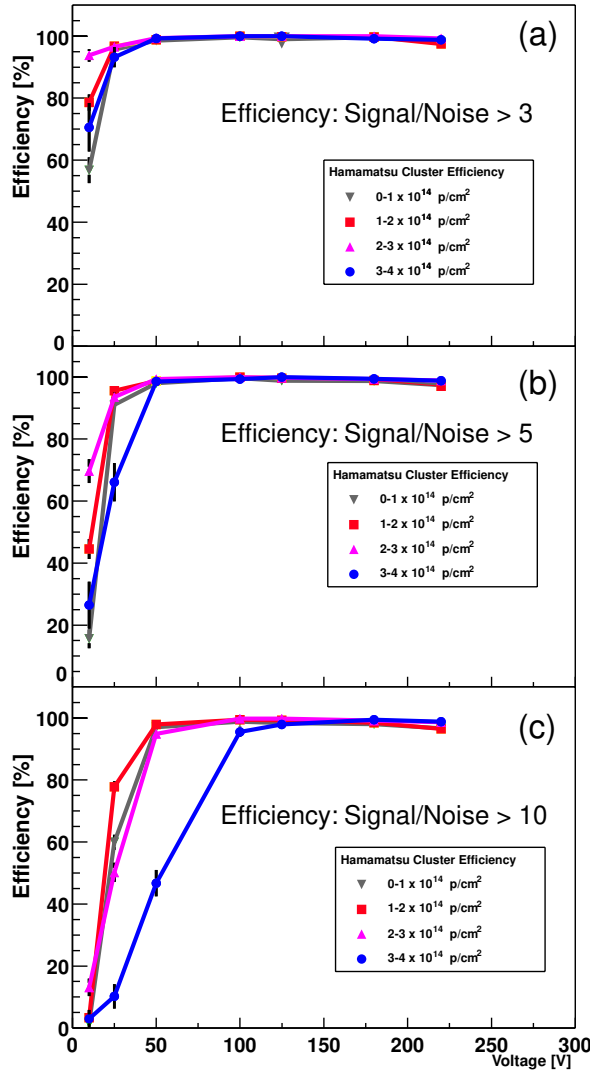


Figure 2.19: Cluster reconstruction efficiency of the PR01 h-14- ϕ sensor as a function of bias voltage for a range of irradiation fluences. In plot (a) the S/N of the cluster was over 3, for (b) greater than 5, and for (c) greater than 10.

irradiated sides (Fig. 2.20). After installation in the test-beam telescope, about 44,000 tracks were reconstructed traversing the sensor and used to analyze its performance.

The efficiency, defined in the same way as for the PR01 tests, is shown by the area of the grey boxes in Fig. 2.22. Two features are immediately apparent - the line of inefficiency displaying the damage caused by the irradiation (cf. Fig. 2.21), and the fact that the outer section, where there is a double metal layer of routing

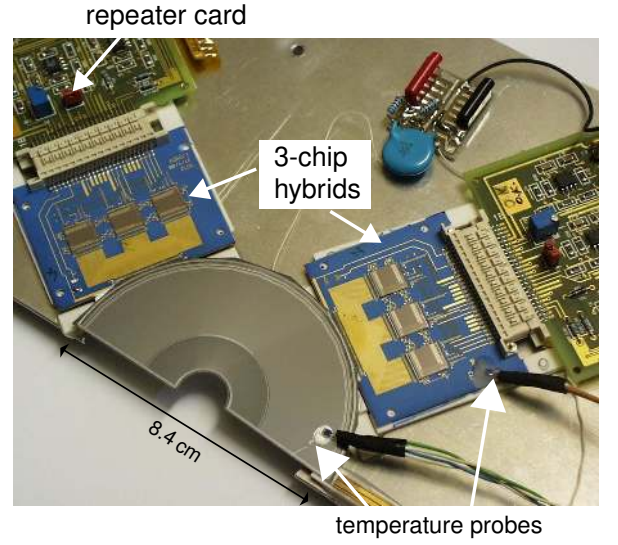


Figure 2.20: Photograph of the PR02 1832-9-a sensor equipped with SCT128A hybrids for evaluation in the 2000 test-beam.

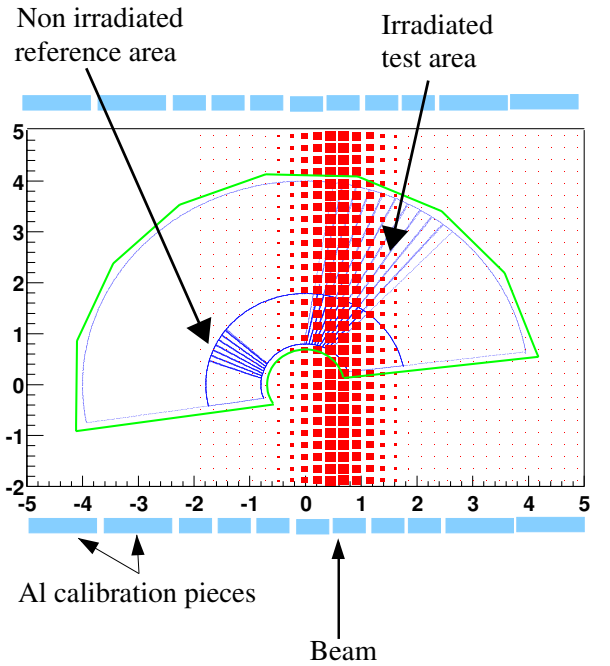


Figure 2.21: Typical irradiation set-up, illustrated for sensor 1832-9-a. The beam intensity was proportional to the size of the shaded squares.

lines, as illustrated in Fig. 2.4, is less efficient than the inner section. This difference in efficiency cannot come from capacitive charge loss to the routing lines, or cross-talk, which would affect equally both the inner and outer region.

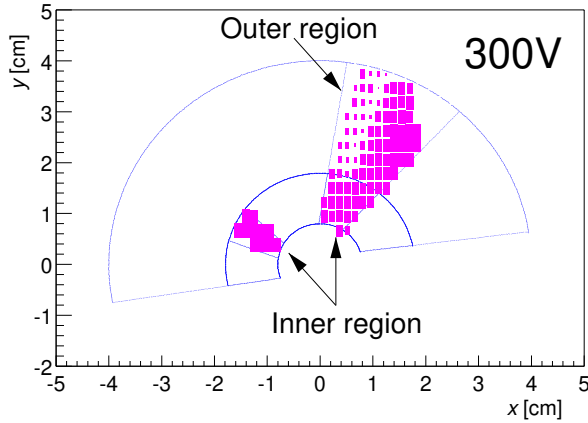


Figure 2.22: Efficiency of the PR02 1832-9-a sensor at $V_{\text{bias}}=300\text{ V}$. The size of the boxes is proportional to the efficiency. The irradiated side of the sensor shows an inefficiency along the line of the irradiation. The additional effect of charge loss to the double metal layer, which is only present in the outer region, is also clearly visible.

It is a signature of an underdepleted layer next to the p-strips, as illustrated in Fig. 2.1. Due to the unique geometry of this sensor it is possible to measure the charge picked up in the double metal layer, as the lines concerned run parallel to the strips. The measurement is illustrated in Fig. 2.23. When the sensor is underdepleted the charge picked up in the second metal layer rises to 20%. Note that for the R geometry, where the double metal lines cross the strips perpendicularly, any lost charge is unrecoverable. It was shown [44] that the clusters spread, as illustrated in Fig. 2.1, and the resolution will degrade as soon as the sensor becomes underdepleted.

For the same reasons the sensor efficiency also shows a very sharp dependence on bias voltage and irradiation. In Fig. 2.24 the efficiency measured at a bias voltage of 300V is illustrated for different irradiation levels.

In the regions with a dose corresponding to about one year of LHCb operation, the depletion voltage rose to about 300 V, which is relatively high for a 200 μm thick sensor.

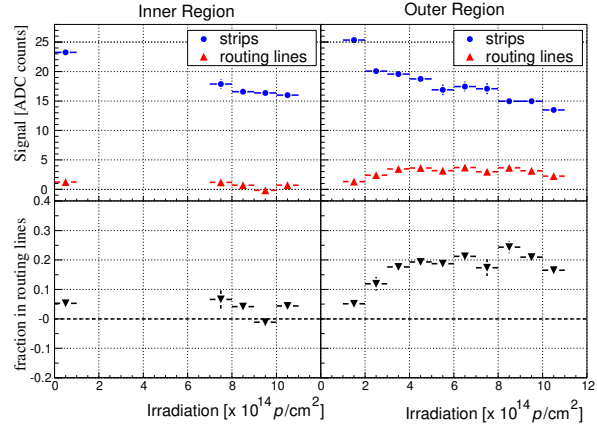


Figure 2.23: Charge from strips, routing lines, and the relative fraction (defined as routing line charge divided by total charge), for the inner (left) and outer (right) regions, at $V_{\text{bias}} = 300\text{ V}$.

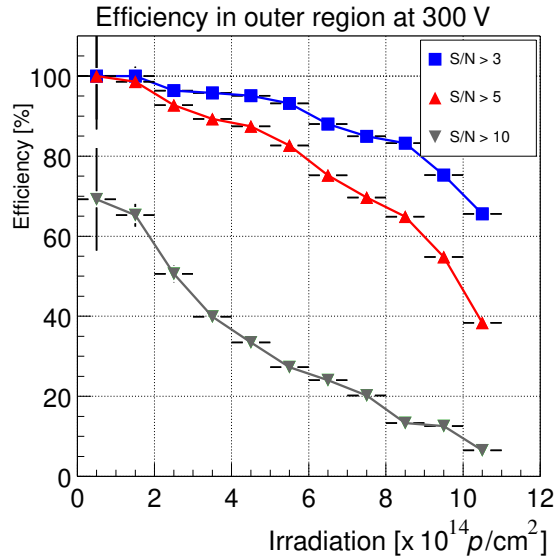


Figure 2.24: Efficiency of the PR02- ϕ 1832-9-a outer region at $V_{\text{bias}} = 300\text{ V}$ vs. irradiation.

2.1.9 Measurements with a laser

In addition to the measurements with a high energy beam, an infrared laser system was used for detailed performance studies [45]. An oxygenated *p-on-n* PR02-R sensor, 1968-17-c, non-uniformly irradiated up to a maximum level of $4.8 \times 10^{14} \text{ p/cm}^2$ of 24 GeV protons, was characterized. The sensor was read out

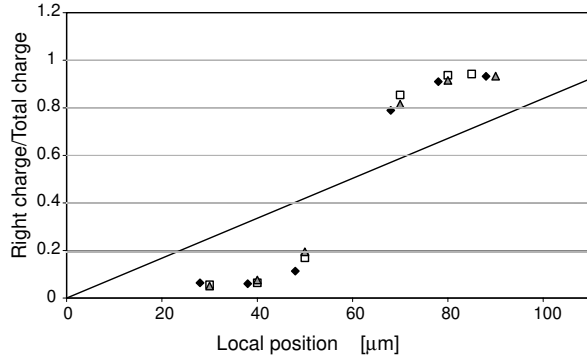


Figure 2.25: Comparison of the laser scan across adjacent strips located in the non irradiated, irradiated with positive gradient of V_{fd} and irradiated with negative gradient of V_{fd} regions respectively.

with a SCT128A chip [31] clocked at 40 MHz.

The system allows the study of the charge collection properties of the sensor as a function of the position, and in particular a possible distortion of the electric field of the sensor in regions of steep gradient in V_{fd} , the full depletion voltage, perpendicular to the strips due the non-uniform irradiation. To study the consequence of such a field on the resolution, the charge sharing between adjacent strips was measured by scanning the laser light across the strips in $10\mu\text{m}$ steps. Fig. 2.25 shows the results of the scan in terms of the η function, defined as $\eta = H_R/(H_R + H_L)$, where H_R and H_L are the signals observed on the two adjacent strips. The scans were performed in regions with opposite sign of the gradient and for strips located in the non-irradiated part. The measurements in the three different regions superimpose well, indicating that the distortion of the electric field does not noticeably influence the charge sharing and therefore the resolution.

The laser set-up was also used to confirm the charge-loss to the second metal layer routing lines in case of under-depletion of the p -on- n sensor, as described in section 2.1.8. Fig. 2.26 shows the fraction of the charge observed in the routing lines for a range of radiation doses and voltages.

In addition, evidence was found for micro-discharge in low irradiation areas of PR02-

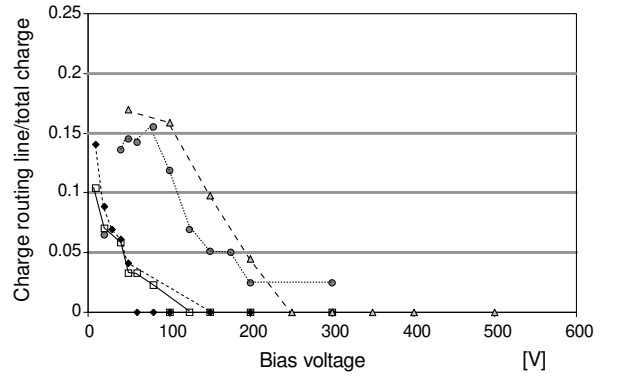


Figure 2.26: Ratio between the charge collected by the routing line to the total collected charge for four strips with different irradiation levels.

R sensor 1968-17-c, while operating above 200V. More details can be found in Ref. [45].

2.1.10 Summary

The LHCb VELO silicon sensor design has been extensively prototyped.

Both p -on- n and n -on- n implementations have been prototyped and tested. Test-beam results with a double sided DELPHI-ds prototype showed that the p -side resolution degrades when the sensor is underdepleted but the n -side resolution remains constant. It was confirmed with test-beam data that the resolution of the p -on- n PR02 design degrades when underdepleted but the n -on- n PR01 design shows consistently good resolution. The degradation in the p -on- n design is accompanied by a fall-off in efficiency. It was also demonstrated, both in the test-beam and using a laser, that the irradiated p -on- n PR02 sensor loses charge to the double metal layer when underdepleted.

Various performance numbers of the prototypes are summarized in Table 2.5. The n -on- n PR01 prototype showed a very good performance with no significant deterioration after doses corresponding to at least two years of LHC operation. The prototyping leads naturally to a choice of n -on- n for the technical design.

	PR01- ϕ	PR02- ϕ	PR02- ϕ
Name	h-14- ϕ	1832-9-a	1968-17-c
Thickness (μm)	300	200	300
Oxygenated	No	No	$2.5 \times 10^{17} \text{ atoms/cm}^3$
Electronics	SCT128A	SCT128A	SCT128A
S/N for a MIP	58:2.7	30:2.0	–
V_{dep} after $2 \times 10^{14} p/\text{cm}^2$	50V	300V	150V
efficiency at $V_{\text{bias}} = 200 \text{ V}$ after $2 \times 10^{14} p/\text{cm}^2$	99%	75%	–

Table 2.5: Performance numbers for the irradiated PR01 and PR02 prototypes. The S/N is given in ADC counts, where one count is equivalent to 380 electrons.

2.2 Hybrid

The VELO hybrid is part of the VELO module (Fig. 2.27) and provides the electronic and mechanical support for the 16 front-end chips and the sensor. In addition, a high thermal conductance is needed to enable the removal of heat from the front-end chips and sensor. Furthermore, a low mass design is required, because most of the hybrids are within the LHCb acceptance (Fig. 1.3). For these reasons, a prototyping programme was defined to study the crucial items.

The layout of the hybrid is such that:

- it allows bonding and rebonding of the sensor and front-end chips;
- the pitch adapter between sensor and front-end chips introduces a minimal stray capacitance;
- there is good isolation between the analog supply lines and digital tracks to minimize noise;
- the grounding is consistent with the overall LHCb VELO grounding scheme (section 3.3.5).

We have considered two basic technologies for the implementation of a hybrid (Fig. 2.28):

- Baseline design: A multilayered kapton bonded to a carbon-fibre substrate (KCF).

- Backup design: A ceramic design.

The kapton design has the advantage that the kapton itself is low mass and thin enabling it to be bonded to a wide range of substrates (CF, ceramic or even metal) without encountering difficulties due to different coefficients of thermal expansion. We have chosen carbon-fibre for its thermal and mechanical properties. The backup technology has the disadvantage that large ceramics (for the VELO we require a ceramic of $14 \text{ cm} \times 10 \text{ cm}$) are not readily available. Beryllia, for example, is difficult to obtain in large sizes and has substantial safety implications in its handling (making it expensive to produce). A ceramic substrate of the correct size and dimensions for the VELO has been fabricated from aluminium nitride, since it is more easily available.

In order to produce a prototype hybrid we have produced a design (laid out for the SCT128A chip) fabricated using traditional techniques on $300 \mu\text{m}$ thick FR4⁴ which may be bonded to CF and which is capable of being manufactured as a kapton. This version (Fig.2.29) will allow us to check the layout, grounding scheme and verify the ability of our production bonders to bond a sensor given the mechanical layout of the hybrid (e.g. connector clearances). In addition, this prototype will be used to check the quality and suitability of connectors. A second generation of hybrids, which builds on the existing work but is fabri-

⁴glass-epoxy PCB base material.

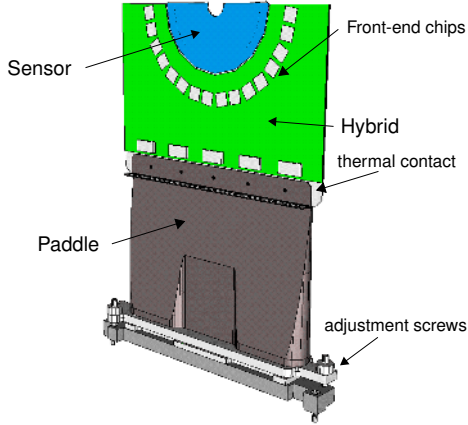
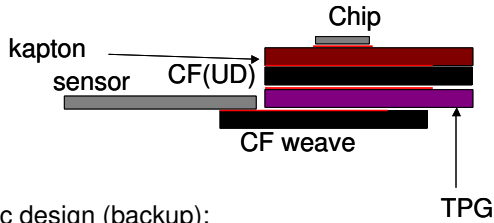


Figure 2.27: One VELO Module, showing the sensor and the hybrid with 16 front-end chips.

KCF design (baseline):



Ceramic design (backup):

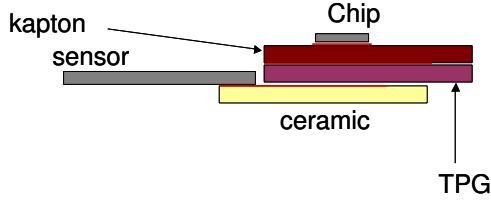


Figure 2.28: Schematics of the two hybrid designs.

cated on kapton, is under design. This hybrid will be able to carry the SCTA-VELO chip.

2.3 VELO modules

The thermal properties of the LHCb VELO module are vital to control the operating temperature of the VELO sensors. The VELO detectors will be exposed to a maximum flux of particles equivalent to $0.5 - 1.3 \times 10^{14} n_{eq}/cm^2$ per year, which will lead to increased depletion voltage and bulk current. The total power dissipation per sensor is expected to stay below 0.3 W when operating the detector below $0^\circ C$ during their lifetime. However all heat

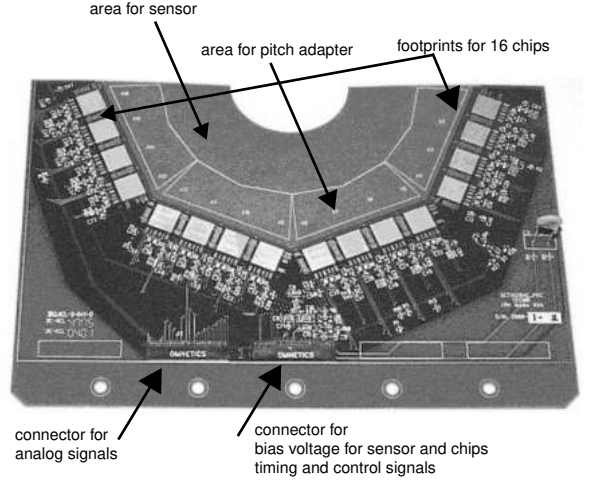


Figure 2.29: Photograph of a prototype PCB-hybrid for SCT128A chip.

will be dissipated close to the beam-line, and the silicon itself will be used to provide the thermal link to the edge of the sensor to avoid extra material. Power dissipation in the silicon bulk heats the detector causing a local increase in bulk current, which will then result in larger currents. At temperatures below $0^\circ C$ the currents will not contribute significantly to the electronics noise, however increased power dissipation due to higher currents could lead to thermal runaway. On the long term higher temperatures will lead to larger depletion voltages. The main power dissipation is due to the readout electronics of the VELO detector, which is designed to stay below 12 W per hybrid. Hence the total power dissipation in a module will be 24 W. Applying a safety factor of 1.5, the cooling system should be able to cope with 36 W per module.

The prototype module design [46] incorporates several key features to be able to guarantee the desired operating temperature of the silicon sensor and electronics.

- A carbon fibre (CF) weave substrate that carries the front-end electronics and provides the mechanical and thermal link to the sensors. The CF is bonded with a thin ($300 \mu m$) layer of thermo-pyrolytic graphite (TPG, $1700 Wm^{-1}K^{-1}$) and a layer

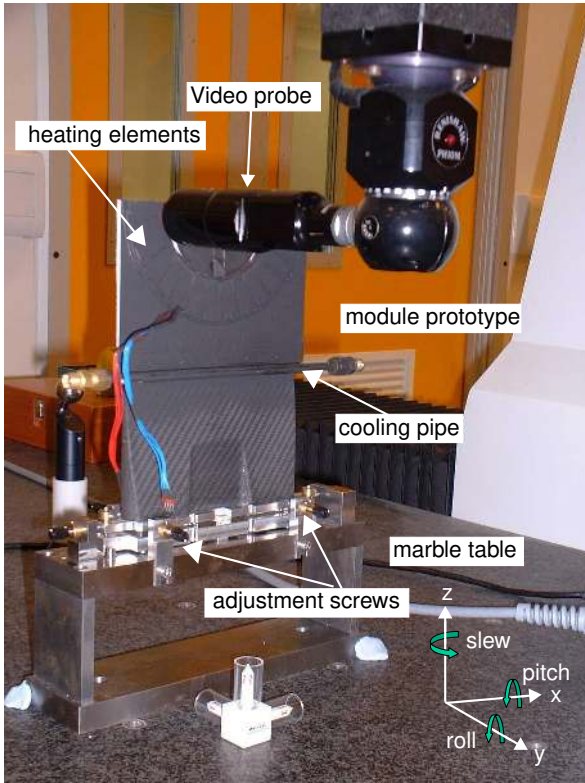


Figure 2.30: Photograph of a module prototype which is used for alignment studies and thermal tests. The video probe of the survey machine is also seen.

of highly conductive ($600 \text{ Wm}^{-1}\text{K}^{-1}$) uni-directional carbon fibre that carries the sensors.

- A connection to the CO_2 cooling system is made through an aluminium (or titanium) coupler and a soft-metal indium joint.
- The sensors are bonded to the CF using a $100 \mu\text{m}$ thick glue layer. The length of the glue bond is a parameter of the prototyping, since it has to strike a balance between good heat transfer and deformation due to different expansion coefficients.

A thermal simulation [47] of the module has been performed to establish that the prototype is capable of keeping the sensors in the temperature range -10° to 0°C . The ANSYS⁵

⁵ANSYS 5.6, ANSYS Inc., <http://www.ansys.com>

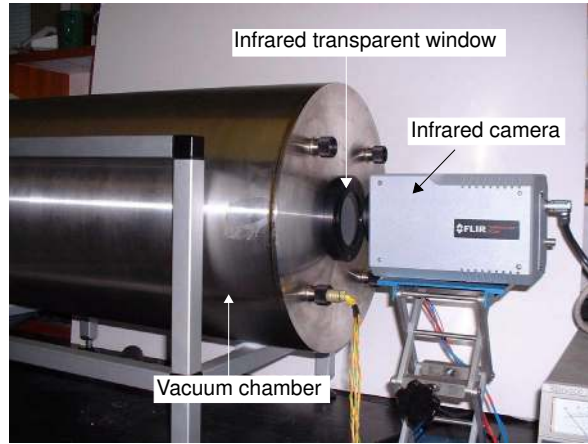


Figure 2.31: Photograph of the vacuum chamber and the infrared camera used for the thermal measurements.

program was used to model the temperature profile of the sensors under the expected and required thermal loads of 24 W and 36 W from the front-end chips. A conservative estimate of 0.3 W in the silicon and a CO_2 cooling temperature of -25°C was assumed. Table 2.6 shows the results of the simulation. In the CF hybrid baseline design using a full glue bond the silicon is kept below the required operating temperature. The backup designs also fulfill this requirement.

Measurements of the temperature profile of the silicon were made using an infrared (IR) camera and a prototype module constructed with an aluminium nitride substrate. The module was operated in vacuum (Fig. 2.31) in order to remove convective cooling (simulating the LHCb environment). The FE-electronics were replaced with small heating elements. Figure 2.32 shows an IR photograph for a power dissipation of 4 W in the heating elements. Preliminary results show agreement between simulation and the measurements performed with the IR-camera to within 1°C .

Two prototype modules with aluminium nitride substrates have been built. Using a non-contact method with a video probe attached to a coordinate measuring machine (Fig. 2.30) it has been shown that the sensors may be reproducibly positioned relative to the location surfaces to a precision of about $5 \mu\text{m}$

Carbon Fibre Composite	T_{cool}	Heat(Chips)	Heat(Si)	Max(Si)	Min(Si)	Max(Chips)
300 μm TPG(baseline)	-25	24W	0.3W	-7.3	-9.9	3.3
	-25	36W	0.3W	-4.2	-7.0	8.9
Aluminium Nitride/TPG	-25	36W	0.3W	-7.5	-8.2	24.5
Beryllia Hybrid/TPG	-25	36W	0.3W	-7.5	-9.6	2.7

Table 2.6: The maximum and minimum temperatures on the sensors and chips for a CO_2 temperature of -25°C , and 0.3W power dissipation in the sensors.

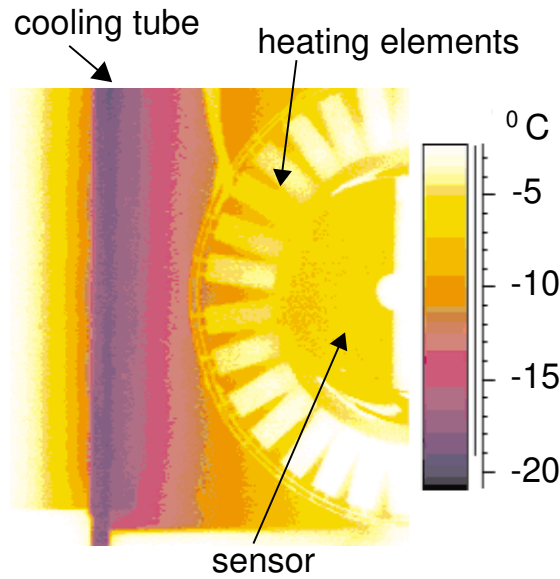


Figure 2.32: Photograph of a prototype VELO thermal module (in vacuum) showing the temperature distribution on the front surface.

in x , y and z (Table 2.7). The alignment involved using fiducial marks on the sensors and depth of focus.

The prototypes were also used to check the thermal stability of the module. Although the sensors were aligned relative to the location surfaces at a controlled temperature of 23°C in operation the cooling system will be at about -20°C and the sensors and electronic will operate between -10°C and $+10^\circ\text{C}$. The materials used do not have identical coefficients of thermal expansion leading to shifts in the position of the sensors relative to the location surfaces. To measure this effect a prototype thermal module was assembled and aligned at 21°C . Initial measurements have studied the effect of heating the base relative to the loca-

	Range	Precision
Translations		
x	0.66 mm	4 μm
y	0.87 mm	6 μm
z	0.24 mm	3 μm
Rotations		
Pitch (x -axis)	0.76°	52 μrad
Roll (y -axis)	0.52°	35 μrad
Slew (z -axis)	1.76°	35 μrad

Table 2.7: Range of adjustments and precisions achieved with adjustment screws. See Fig. 2.30 for the definition of the coordinate axis and angles.

tion surfaces to study the performance of the base structure. With a 10°C increase in temperature of the base with respect to the alignment jig (platform) less than $10\mu\text{m}$ shift was observed in the sensor fiducial relative to the 21°C position in the x and z -positions only. However, shifts of $100\mu\text{m}$ in the y -direction were observed. Both the design and properties of the materials are being studied to understand the source of this large movement.

2.4 Front-end electronics

2.4.1 Front-end chip

Since a fast readout chip satisfying the LHCb requirement as discussed in section 3.3.2 was not available, it was decided to develop one within the collaboration. Possible candidates to start from were the SCT128A chip [31] developed for ATLAS and the HELIX chip [48] developed for the HERA-B experiment. The former was built in the radiation hard DMILL [49] silicon-on-insulator pro-

cess, the latter is realized in a standard $0.8\text{ }\mu\text{m}$ CMOS process with a radiation tolerant design. Both chips are based on the RD20 architecture [50] shown in Fig. 2.33, which contains a low-noise charge-sensitive RC-CR preamplifier/shaper stage, an analog pipeline, a de-randomizing buffer for triggered events and a multiplexer.

In the meantime access became available to the $0.25\text{ }\mu\text{m}$ CMOS technology. Due to reduced threshold voltage shifts under irradiation this technology provides an enhanced intrinsic radiation hardness. Using appropriate design rules, like enclosed gate structures [51], consistent use of guard rings [52], and forced bias currents, it can be made at least as radiation hard as the DMILL technology. It thus appeared to be the technology of choice for the development of an LHCb front-end chip. To minimize the risk related to switching to a new technology, it was decided to pursue a dual approach:

- modify the existing SCT128A chip such that it fulfills the requirements for the readout of LHCb. This chip will be referred to as SCTA_VELO,
- develop a new chip, the Beetle, in $0.25\text{ }\mu\text{m}$ CMOS technology.

R&D work towards the final front-end chip encompasses measurements with the existing SCT128A chip, the predecessor of the SCTA_VELO, studies of test chips with components of the Beetle and results from the first prototype of the complete chip, the Beetle1.0. The final version of the SCTA_VELO and an improved version of the Beetle have been submitted at the end of 2000 and in March 2001 respectively. Both chips are expected back before the summer of 2001. The final decision which chip to use for the VELO at the startup of LHC will be taken mid 2002 at the latest.

The SCT128A and SCTA_VELO chips

Measurements were performed with the SCT128A chip, which has a similar front-

end amplifier as the SCTA_VELO. A PR01-R prototype sensor was equipped with several SCT128A chips (Fig.2.15) and was readout in a test-beam run. Figure 2.34 shows the measured pulse shape based on 150,000 high momentum particles crossing the detector. The timing information was given by a scintillator signal. The input capacitance varied between 15 and 22 pF. One observes a rise time from 10% to 90% of 19 ns and a remainder of about 38% of the peak height after 25 ns [53]. This remainder is expected to be suppressed to 20% in the SCTA_VELO (Fig. 2.34, lower plot).

In addition Fig. 2.34 shows a significant undershoot of up to 18% of the peak height, which takes up to 600 ns to settle on the baseline, but has a negligible impact on the performance of the VELO due to the low occupancy.

The equivalent noise charge (ENC) of the SCTA_VELO is expected to be $\text{ENC} = 600\text{ e}^- + 30\text{ e}^-/\text{pF}$. Details about the design of the chip can be found in Ref. [54].

The Beetle chip

The development of the Beetle is described in detail in [55]. Before assembling the complete chip, individual components were submitted and tested on separate chips.

For the bias settings given in [56], the equivalent noise charge (ENC) has been measured as $\text{ENC} = 790\text{ e}^- + 17.5\text{ e}^-/\text{pF}$. Figure 2.35 shows a comparison between a measured and simulated pulse shape for a given bias setting. For this measurement a charge of 15,600 electrons was injected at a capacitive load of 3 pF. There is a reasonably good agreement between the measurements and the simulation. The rise time is measured to be 15 ns, the remainder 25 ns after the peak is about 20% of the peak pulse height. Figure 2.36 shows the expected behavior of the Beetle1.1 chip for load capacitances between 10 and 40 pF. The peaking time is essentially independent of the load, but the fall time increases while the peak pulse height decreases with growing capacitance.

To illustrate the working of the entire chip,

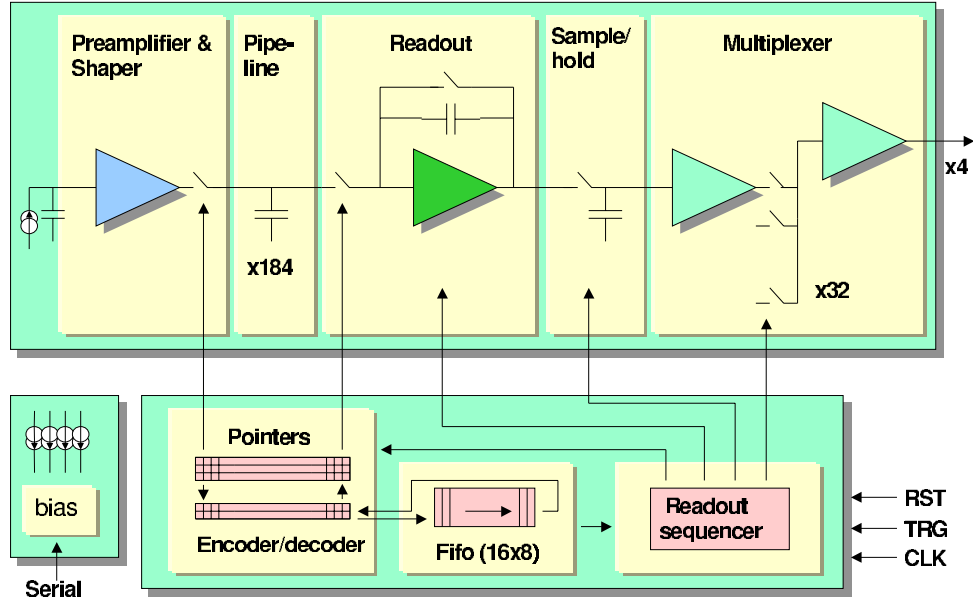


Figure 2.33: Schematic block diagram of the RD20 chip architecture as implemented in the SCTA-VELO front-end chip.

Fig. 2.37 shows the output signal of the complete analog chain for Beetle1.0. All 128 channels are multiplexed on one port. The figure is an overlay of different events with input signals corresponding to 1, 2, 3, 4 and 7 MIPs applied to 7 single and a group of 4 adjacent channels of the chip. On the figure the different input levels are most clearly visible on the group of 4 channels. The baseline shift is due to a voltage drop on the bias line of the pipeline readout amplifier, which has been corrected for in the current submission of the Beetle1.1.

A test-chip containing the front-end amplifier was tested in detail before and after irradiation to 10 Mrad using an X-ray source. After the irradiation the chip was still functional [56].

2.4.2 L1 Electronics

The use of the VELO information in the L1 trigger requires custom-made electronics of high integration which are able to receive analog data at 40 MHz, digitize and perform zero-suppression before sending the digital data to the L1 processors. It also needs to test event synchronization. A prototyping programme

has been executed to study some of the critical tasks:

- the analog transmission and digitization at 40 MHz of event data coming from the front-end chip at the L0 trigger rate of 1 MHz;
- the preprocessing of digitized data (pedestal subtraction, common mode correction) before sending them to the L1 trigger;
- the interfaces to the TTC, ECS and DAQ systems of LHCb.

A first prototype board, Read-out Board 2 (RB2) [57], had been built which is 1/16 of the final board. The RB2 is made of a VME 6U mother board and several interchangeable daughter boards (Fig. 2.38).

The daughter boards implement many of the L1 electronics features:

- The TTCrx daughter board carries one TTCrx chip [58] which decodes the 40 MHz system clock and the trigger commands sent via optical fiber.

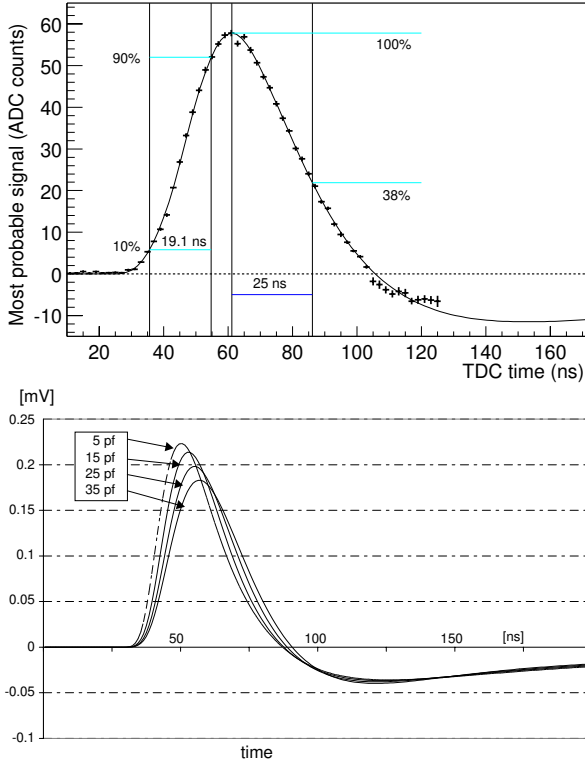


Figure 2.34: Pulse shape of the SCT128A readout chip. The upper figure is a result obtained with the SCT128A in the readout of a prototype sensor in a test-beam of MIP particles [53]. The lower figure shows the expected pulse shape of the SCTA.VELO readout chip for different capacitive loads at the input.

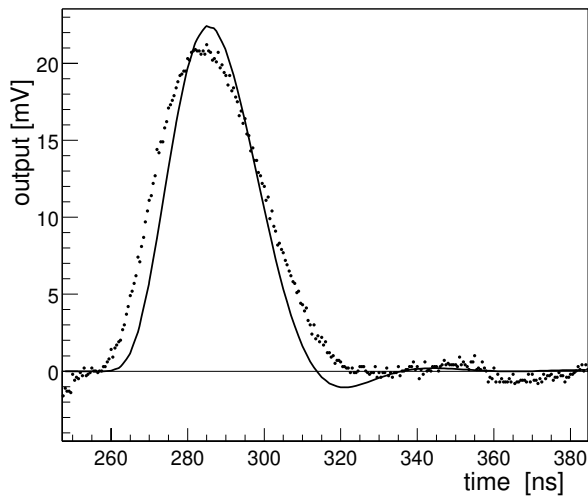


Figure 2.35: Comparison between measured (dots) and simulated (full line) pulse shape of the Beetle1.0 for a particular bias setting and 3 pF load.

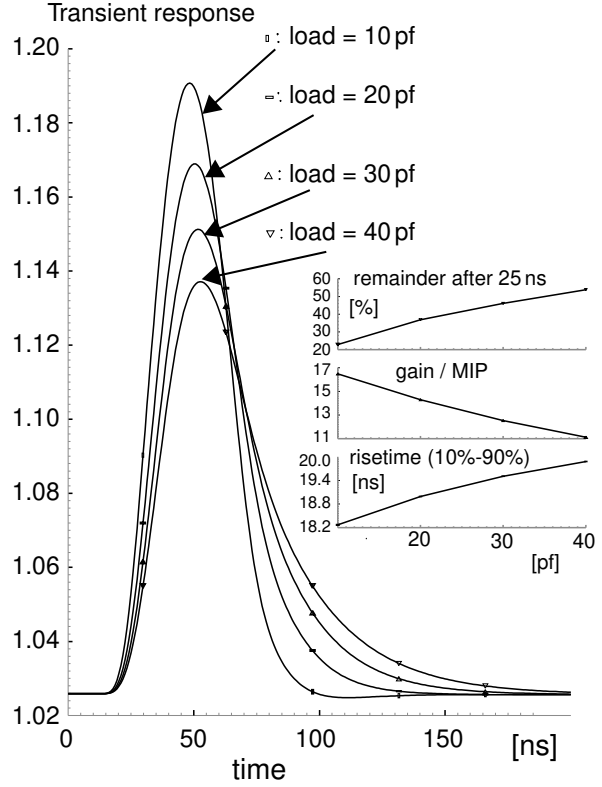


Figure 2.36: Expected pulse shape for the Beetle1.1 for load input loads between 10 and 40 pF.

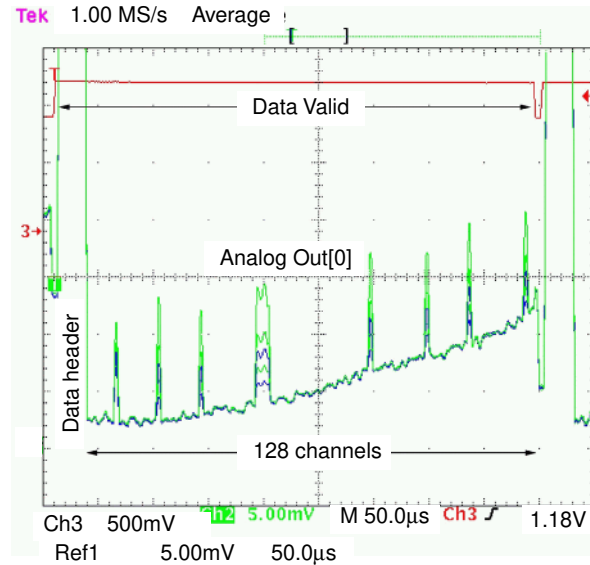


Figure 2.37: Output of the complete analog chain showing test pulse patterns applied to the inputs of the Beetle1.0 chip.

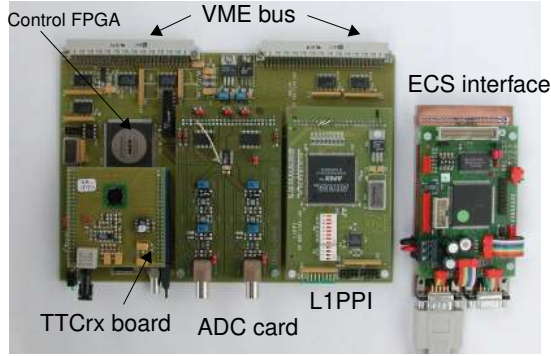


Figure 2.38: RB2 board with its various components.

- The FADC cards, equipped with the 8-bit ADC chips AD9059 [59], sample the analog data from the front-end at 40 MHz. An SMD version of this card which carries the line equalizer for long cable transmission operations has been produced.
- An Experiment Control System (ECS) interface prototype based on the 68HC12D60 micro-controller allows remote access to the RB2 board via serial interface or CANbus for the following operations:
 - reprogramming of EPROMs, which store the FPGA configuration data, using the JTAG interface [60],
 - downloading parameters to the devices on the board (DAC, TTCrx) using the I²C interface.
- A Level1Pre-Processor Interface card equipped with an APEX100K-2E FPGA working at 80 MHz to execute the zero suppression algorithm [61].

The performances of the analog to digital front-end data conversion have been studied [62] with the RB2 board reading data from a prototype sensor (section 2.1 and Fig. 2.15) equipped with SCT128A chips. The measurements have been done in laboratory conditions with a short cable connection between the sensor and the FADC cards. The analog data was read out and sampled at 40 MHz. Test-beam

Part	Latency time (μ s)
Pedestal	0.5
Faulty channels	0.5
Common mode suppression	< 10.0
Reordering	0.5
Cluster encoding	1.0
Encapsulation	1.0
Link	3.0
Total	< 16.5

Table 2.8: Latency times in the L1 PreProcessor.

data was used to obtain the absolute calibration (in electrons) of the FADC cards. A 1280 e^- noise level has been measured compared to 1100 e^- using a commercially available digitizer board [63] and a readout and sampling speed of 5 MHz. A possible reason for the increased noise of the RB2 is the insufficient electromagnetic shielding of the analog part from the clock and power supply lines. This will be improved for the next prototype board [64].

The RB2 equipped with a passive line equalizer has been used to perform a study [65] of driving analog data over a distance of 60 m (Fig. 2.39). Test pulses corresponding to a 1 MIP particle with a width of 25 ns and a rise time of 2 ns were generated with a pulse generator (Fig. 2.40) and with a SCT128A chip. A 7 ns rise time has been measured at the receiver end. The observed cross talk between neighbouring samples was 3% and is similar to using 8 m long cables without a line equalizer [66]. However, the measured S/N performance turned out to be degraded by about 10% which was not expected and is under investigation.

A prototype of the L1 PreProcessor (L1PP) has been used [61] to test fast zero-suppression algorithms for the L1 interface. The L1PP prototype processes 128 channels (1/4 of the final L1PP) using an APEX100K-2E FPGA working at 80 MHz. Test-beam data and particle signals from a Monte Carlo generator were used as input. The output of the FPGA agreed with the simulation [61]. The measured contributions to the L1 latency time

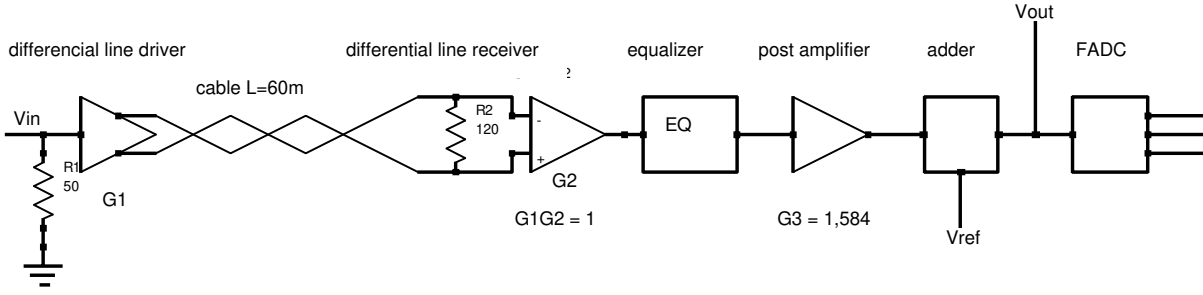


Figure 2.39: Setup of the 60 m analog transmission line.

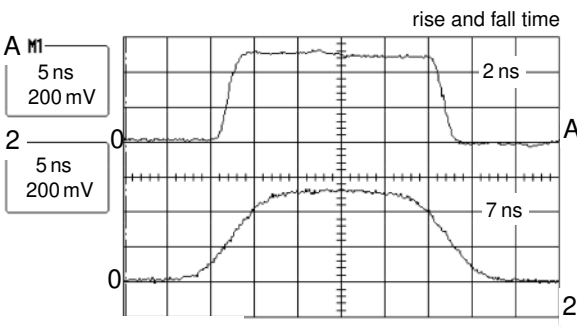


Figure 2.40: Test pulse of 25 ns width measured before and after 60 m.

are listed in Table 2.8. The total latency time is below $17\mu\text{s}$, which is less than 1% of the total available latency.

Low level software has been written for the ECS prototype interface board. The JTAG and the I²C interface have been tested with the LIPP prototype card.

2.5 Mechanics, wake fields, cooling and vacuum

Here, we report on the R&D work related to operation of the silicon detectors and to VELO-LHC integration issues, which include mechanics, vacuum, and wake fields. Much of this effort was focused on the design and optimization of the secondary vacuum containers, the protection schemes of the vacuum system, and the proof-of-principle of the chosen cooling scheme.

2.5.1 Mechanical aspects of the secondary vacuum container

The secondary vacuum container represents one of the most critical parts of the VELO structure. The container must be radiation resistant and act as a wake field suppressor (electrical properties). In addition, the container provides a separation between primary and secondary vacuum (ultra-high vacuum compatibility). The container walls located within the LHCb acceptance must be manufactured from low-mass material. Further, this thin-walled structure must allow for a small overlap between the silicon sensors of the two opposite halves, implying the use of a complex corrugated structure, and it must accommodate the motion of the detector halves. In our design, this is achieved by interfacing the thin-walled structure with the vacuum vessel via large rectangular bellows.

The mechanical properties of the thin-walled structure, in particular its behavior under the event of a pressure difference between primary and secondary vacua, were investigated by numerical simulations. Fig. 2.41 shows the results of a finite-element analysis (FEA) for the maximum displacement of the foil surface (before permanent deformation occurs), for aluminium. In normal operation the pressure difference is less than 1 mbar. The FEA results show that a 0.25 mm aluminium structure would sustain a pressure difference of up to 17 mbar without undergoing plastic deformation. The results of such calculations must be interpreted with care, as the actual mechanical properties of the treated

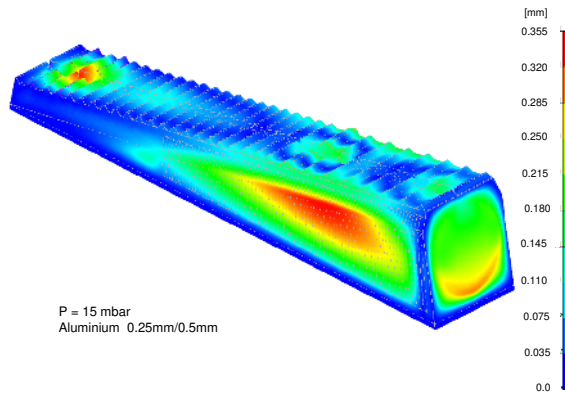


Figure 2.41: FEA results showing the displacement on the aluminium encapsulation for a pressure difference of 15 mbar.

material can differ substantially from the assumed values. A first measurement of the rupture pressure was performed on a small prototype encapsulation with a 0.1 mm corrugated aluminium wall welded onto 0.3 mm thick aluminium side walls. The rupture pressure was found to be about 80 mbar, whereas the plastic deformation pressure was measured to be around 1 mbar (in reasonable agreement with FEA calculations). Further tests will be carried out on the encapsulations fabricated according to the final design.

The fabrication of such complex thin-walled encapsulations is delicate and time-consuming. An extensive prototyping programme is ongoing, in which various techniques are being studied to realize the desired shape. Fig. 2.42 shows the current status of these developments. The corrugated foil was manufactured from a 0.25 mm aluminium 3004 sheet (99 % purity) using two moulds and repeating about 20 cycles of pressing and annealing.

The large rectangular bellows (36 cm width \times 126 cm length) separating the two vacua must accommodate the 30 mm displacement in the horizontal plane (compression of the bellows) as well as for a ± 6 mm lateral displacement in the vertical plane. For the latter reason, a pair of bellows separated by a flat section of 80 mm is used (see Fig. 1.6 and Fig. 3.14).

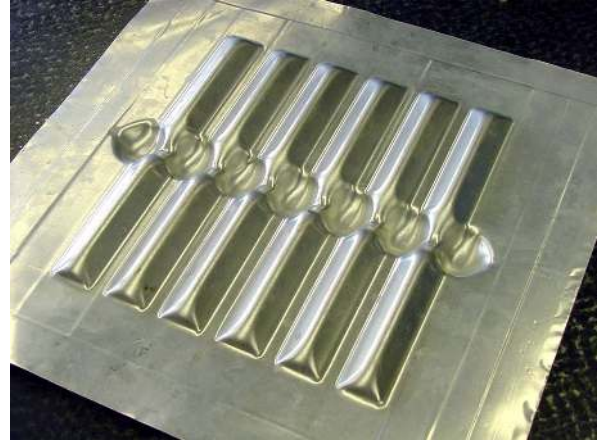


Figure 2.42: Sample 0.25 mm thick aluminium encapsulation.

These bellows do not need to sustain a differential pressure of 1 bar, hence a dedicated production method was developed which starts from preformed 0.15 mm thick stainless steel sheets (membrane width of 5.5 cm): in a first step the sheets are spot-welded around the edges with a Nickel-alloy (brazing) foil pinched between the two surfaces; in a second step, the Nickel-alloy foil is molten in a vacuum oven. This results in a smooth solder joint. This technique has been demonstrated on a small sample, see Fig. 2.43. The prototyping programme is now continuing with the production of a circular bellow, the mechanical properties and vacuum tightness of which will be tested thoroughly.

2.5.2 The secondary vacuum container as a wake field suppressor

Beam bunches passing through the VELO structures will generate wake fields as a consequence of the geometrical changes and/or of the finite resistivity of the wall materials. The generated wake fields can affect both the VELO system (RF pick-up, heat dissipation) and LHC beams (instabilities). Hence, the design must take into account minimization of heat dissipation, of the coupling impedance, and of the electromagnetic fields inside the detector housing.

The issue of RF pick-up by the silicon de-

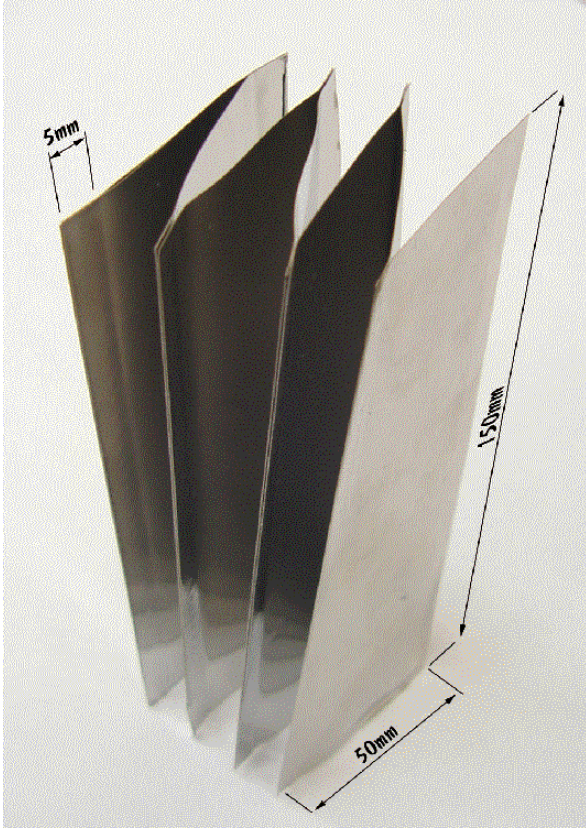


Figure 2.43: Sample 0.15 mm thick stainless steel membrane manufactured according to the method described in the text.

tector modules was addressed by estimating the attenuation of the LHC electromagnetic fields through the thin aluminium shield [67]. The use of a 0.1 mm thick aluminium foil, as proposed in the TP [1], might be insufficient to protect the detectors against high-frequency pick-up noise. Present calculations yield a minimum thickness of 0.18 mm. Pending a more accurate determination based on measurements with a fully equipped detector module, the thickness has been increased to 0.25 mm.

We addressed the issues related to the longitudinal loss factor and coupling impedance by simulations with the codes MAFIA⁶ and ABCI [68] which numerically solve Maxwell's equations to obtain the wake fields. Calculations in the frequency and time domain were

⁶MAFIA Collaboration, CST GmbH, Lautschlagerstr 38, 64289 Darmstadt.

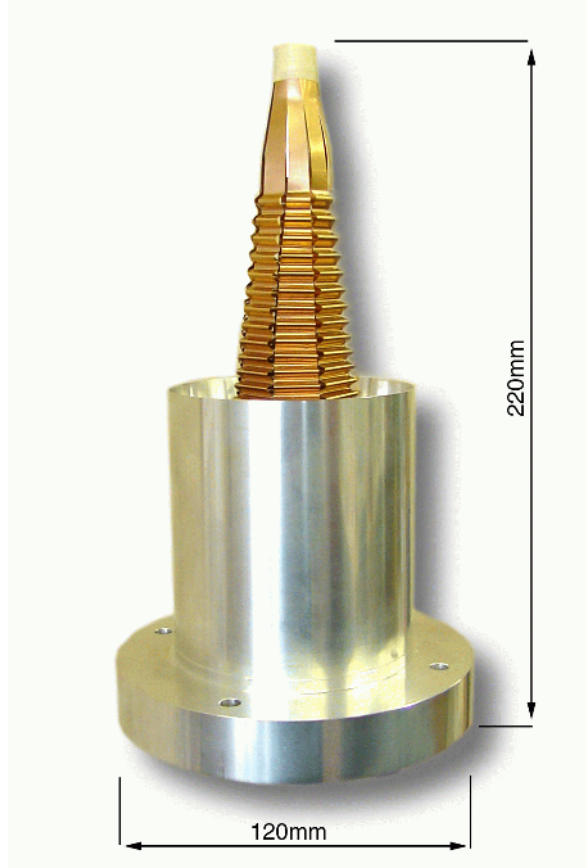


Figure 2.44: Photograph of a prototype wake field suppressor made of copper-beryllium alloy.

performed to study both resonant and transient effects. In the design of the VELO, wake field suppression is achieved by enclosing the silicon detector modules in a shielding box made of aluminium and ensuring that a continuous conductive surface guides the mirror charges from one end of the VELO vessel to the other. The end connections consist of segmented half tapers fabricated from (19 cm long, 70 μm thick) corrugated copper-beryllium strips (see Fig. 2.44 and Fig. 3.13). The corrugations are needed to allow for mechanical motion of the detector housings relative to the vacuum vessel and exit window.

In the LOI [69] and TP [1] designs the silicon detector modules are individually enclosed in thin aluminium boxes which form a continuous wall structure with deep cavity-like corrugations. A first study with MAFIA in the frequency domain showed that such deep cor-

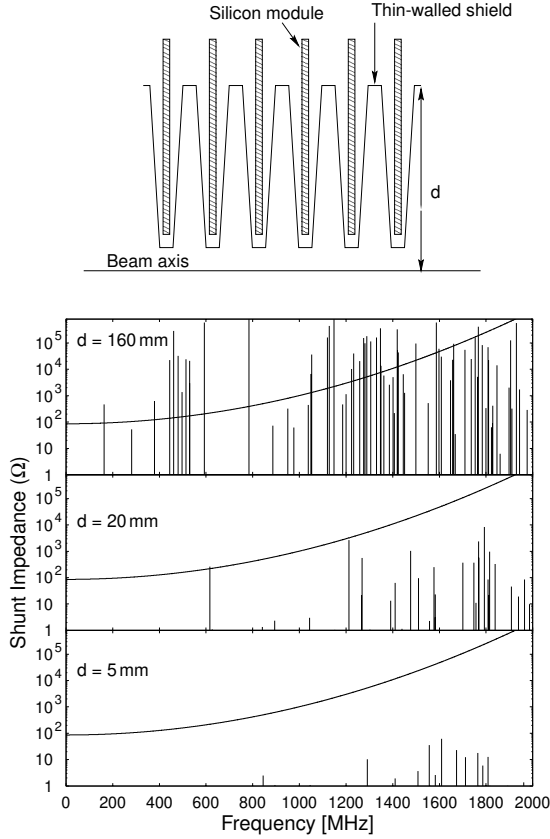


Figure 2.45: Top: Sketch defining the corrugation depth d . Bottom: Shunt impedance versus frequency calculated with MAFIA showing the resonance spectrum for various corrugation depths.

corrugations result in a dense spectrum of resonant modes with large shunt impedances [11]. The use of thin conducting ribbons throughout the vertex detector primary vacuum vessel [12] to screen these complex structures from the beams is technically difficult, given the constraints of multiple scattering and resistive wall losses. Instead, we studied the alternative solution of reducing the corrugation depth to a value which sufficiently suppresses wake fields [13]. The spectrum of resonant modes was analyzed for three different corrugation depths (160, 20 and 5 mm). The results of these calculations are shown in Fig. 2.45 (shunt impedance versus frequency). The curve indicates the shunt impedance for which a maximum power of 100 W could be deposited



Figure 2.46: Full scale model of the VELO structure for RF tests.

by the beams assuming the frequency matches with a multiple of the bunch repetition frequency (40 MHz). It is seen that for a corrugation depth of less than about 20 mm the risk to deposit such an amount of power into a single mode of the VELO structures disappears. Based on these results we decided to pursue this option and studied similar structures with a shape optimized for minimum multiple scattering [13].

In a second step, we study the effect of the VELO structures on the beams. Time domain calculations with ABCI and MAFIA are under way. Preliminary results for the detectors in the closed position [14] indicate that the low-frequency slope of the imaginary part of the coupling impedance is of the order of $5 \text{ m}\Omega$ ⁷. Calculations for the detectors in the open position will be carried out as well. In this position, the top and bottom gaps can be screened if needed by connecting the two halves with flexible metallic strips.

We intend to supplement our simulations with a series of measurements on a one-to-one scale model of the VELO. Fig. 2.46 shows a photograph of the setup. Realistic wake field suppressors and detector encapsulations are implemented in this vessel. Several loop antennas are used to monitor the components of

⁷To give a scale for comparison, the LHC shielded bellows and monitor tanks contribute about $0.12 \text{ }\Omega$ to the effective impedance budget [70].

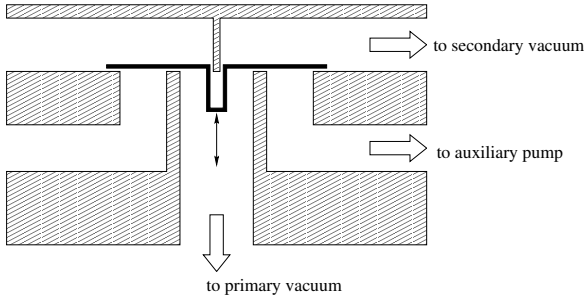


Figure 2.47: Sketch illustrating the principle of the gravity-controlled valve.

the (oscillating) magnetic fields tangent to the wall surface. Measurements of the resonant modes and coupling impedance of the mock-up will be performed by using network analyzers and the wire-method [71]. Shielding efficiency measurements will be carried out with prototype detector modules.

2.5.3 Protection of the secondary vacuum container

The thin-walled secondary vacuum container is a critical item in the VELO system. As discussed in section 2.5.1, the thin separation foil is expected to deform irreversibly under the effect of a pressure difference exceeding 17 mbar. As a consequence, the design must include a protection scheme against possible failures that would lead to an increase of the differential pressure across the thin wall. Electrically activated valves controlled by differential pressure switches will be applied. In addition, a protection valve has been developed that does not depend on any sensing device or external supply (power and compressed air). The principle of the valve, illustrated in Fig. 2.47, consists essentially of a light aluminium disc resting on the end of a tube under the action of gravity. In case of an increase of pressure in the primary vacuum section, the disc moves up directly under the effect of the pressure difference and equalizes the pressures in the two volumes. To reduce the residual valve conductance between the two vacua in normal operation, the valve is differentially pumped by an auxiliary pump.



Figure 2.48: Vacuum test setup.

The valves are used in a ‘tandem’ scheme to protect the foil against a possible increase of pressure on either side of the foil. A first prototype valve was designed, constructed and tested (Fig. 2.48). The results of the test showed that a residual conductance of $10^{-5} \ell/s$ ($10^{-3} \ell/s$) can be achieved for air at room temperature with (without) pumping with the auxiliary pump. The valve was also successfully tested against a sudden burst of air into one of the vacuum systems. The differential pressure remained under about 6 mbar. This prototyping and test programme will be continued on a more sophisticated vacuum setup as the VELO design evolves.

2.5.4 Proof-of-principle of the CO₂ cooling system

The choice of CO₂ as a coolant for the VELO silicon detectors was motivated mainly by its excellent cooling properties and radiation resistance. A two-phase cooling system was chosen in which the heat from the source is absorbed in the evaporation process of the (liquid) cooling agent. Near the heat source, the coolant is kept in mixed-phase equilibrium by controlling the return pressure, which automatically determines the operating temperature. Each module will be cooled down by a cooling capillary. Liquid CO₂ will be distributed in parallel to each capillary from a manifold. To avoid coupling between the vari-

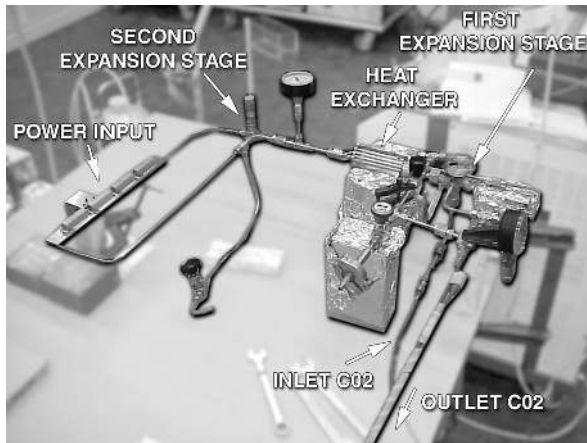


Figure 2.49: CO₂ cooling test setup.

ous capillaries, each will be preceded by a flow restriction.

Measurements were carried out with a test setup which demonstrated that (a) a cooling capacity of 30 W per capillary can be achieved, and (b) that, when cooling down in parallel multiple sources with different heat inputs, the operating temperatures can be kept stable. The first tests were performed with a stainless steel cooling capillary of 1.0/1.3 mm inner/outer diameter [72]. A cooling capacity of up to 5 W/cm was obtained. Hence, with a 10 cm long capillary one can comfortably accommodate a cooling power of 50 W. Operation in parallel was checked with 5 identical capillaries loaded with various heat sources. Fig. 2.49 shows a photograph of the test setup. In a next step, a full-scale setup with 27 stations, operated in vacuum, will be constructed and tested.

3 Technical design

The technical design of the VELO is based as far as possible on the experience and results obtained with the prototypes described in the previous chapter. The description will be organized as follows: first the design of the sensors, which will be based on the n -on- n implementation, together with their expected lifetime will be given. The designs for the hybrids and mechanical stands have not been finalized, but will follow closely the prototypes presented in the previous chapter. Here, the design descriptions are not repeated, but the overall constraints and chosen materials are presented. The architecture of the electronics will be presented next, where it should be noted that there are two candidate FE-chips, and that most of the electronics will be located behind the shielding wall to avoid radiation, and SEU (Single Event Upset) in particular. A detailed description will be given of the mechanical structure which houses the VELO, its interference with the LHC beam and primary vacuum, and the cooling system to assure low Si-bulk currents and to suppress the inverse annealing of the sensors after irradiation. The total material budget which is the consequence of the design, and the strategy to be able to align the detector will complement this chapter.

3.1 Sensors

The design of the sensors combines the features of the prototype detectors as described in section 2.1. Since the n -on- n implementation has been chosen, the strip layout reflects the prototypes PR01-R and PR01- ϕ , while for the total size and number of channels prototypes PR02-R and PR02- ϕ have served as guidance.

A design for which all the design features have been achieved in one of the prototype detectors is called a 'realistic' sensor. This realistic sensor is what is used for the performance studies described in section 4. However, it was found that with some more R&D, improvements could be achieved [4], both in radiation hardness and physics performance. These sensors are referred to as 'ultimate' sensors. The requirements and constraints for the sensors can be summarized as follows:

- The size of the sensors must be limited to fit into a 100 mm diameter wafer. This avoids limiting the number of manufacturers, and does not exclude the purchase of the ultimate 200 μ m thick sensors, rather than the 300 μ m realistic sensor. The sensor has to cover one half station, rather than having to achieve this coverage with several detectors, which avoids an increased complexity both in the construction and alignment of the stations. This limits the largest radius to 42 mm.
- The VELO has to provide stand alone tracking for the L1-trigger, hence the VELO needs three independent views. To simplify and accelerate the L1-algorithm, the three views are one R-measurement and two quasi ϕ -measurements for which the strips have a stereo angle. The L1-algorithm also requires the R-strips to be segmented in ϕ , to allow the determination of the primary vertex position in the plane perpendicular to the beam, based on the R-measurements alone. A segmentation better than 60° has been shown to be

sufficient.

- The implants must be AC coupled to the amplifiers to avoid large pedestal variations due to current induced by the non-uniform irradiation.
- The minimum strip pitch achieved (prototypes PR01-R) is $40\text{ }\mu\text{m}$. This allows individual p-stops per n-strip to interrupt the electron accumulation layer on the ohmic side of the sensors. In the ultimate sensors the pitch could be reduced by using p-spray rather than p-atolls.
- The occupancy per channel should be kept as low as possible, to allow efficient and ghost-poor tracking in the L1-trigger. By decoupling the strip layout from the readout by using a double metal layer to route the signals to the edge of the detector one could in principle adjust the strip pitch and length to achieve an equal occupancy on all channels. However, the measurements closest to the primary vertex contribute most to the impact parameter error, implying that the smallest pitch should be used for at least the first few measurements. Figure 3.1 shows the radii of the first two measurements of a track, hence typically the smallest pitch should be kept for radii below 20 mm.
- The number of electronic channels per sensor should be a multiple of 128, and the number of FE-chips should fit at a radius reasonable close to the maximum sensor radius. This leads to 16×128 channels per sensor, as has been used for PR02-R and PR02- ϕ .
- The biasing of the sensors is achieved using poly-silicon resistors rather than FOXFET-biasing because of radiation resistance [73].
- After irradiation the necessary large depletion voltages might lead to micro-discharges, especially at the end of the

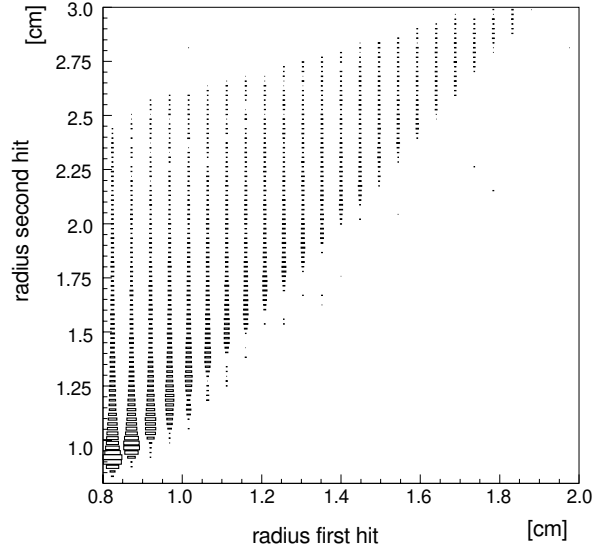


Figure 3.1: Radii of the two measurements of a track closest to the primary vertex.

strip. Hence all strips have to be rounded to avoid local high field regions.

Figure 3.2 shows a cartoon of the layout of the strips on the realistic R-sensor and the ultimate ϕ -sensor. The realistic ϕ -sensor cartoon is shown in Fig. 1.5.

The strips on the R-sensor are subdivided in to four strips for smaller radii, while for larger radii the subdivision is only two. The area of the sensor at small radius has the highest particle flux, and the strixel¹ length can be as small as 6 mm. The n-implants are AC-coupled to Al readout strips, which in turn are connected with via's to the routing lines on a second metal layer which bring the signal to the readout chips. The second metal layer is insulated from the readout strips with a 2–5 μm SiO₂ or poly-amide dielectric layer. Due to this second metal layer no floating strips can be used in the R-sensor design, since this would lead to significant charge loss [74].

The ϕ -sensor uses strixels in a region at small radius, and longer strips for the outer region of the detector. In the ϕ -sensor floating strips could in principle be used, since the second metal layer lines which route the sig-

¹A name invented by B. Henrich for the grey area between pixels and strips.

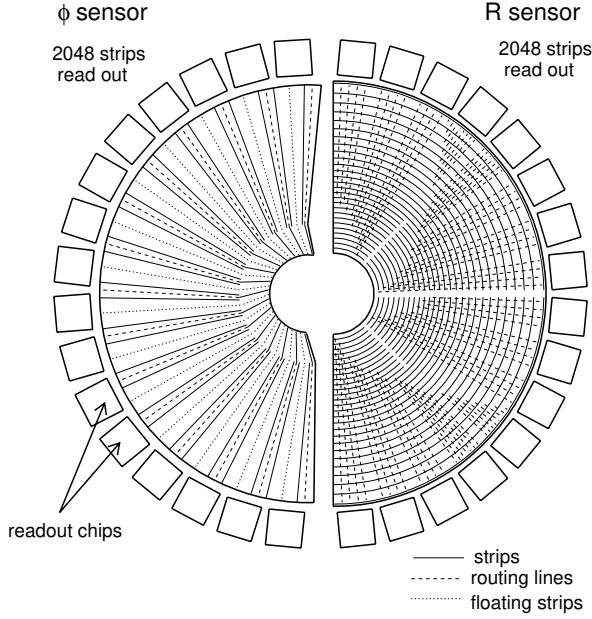


Figure 3.2: Schematics of the strip and routing line layout of the realistic R-sensor and the ultimate ϕ -sensor.

nal from the strixels to the electronics could be oriented so as to avoid any crossing with floating implants. However, for the realistic detector design no floating strips will be used. The ultimate sensor with floating strips would give an improved resolution since the charge sharing in the ϕ -strips is practically only due to diffusion, while in the R-sensor the charge sharing is a convolution of the diffusion and the spread of the charge due to the polar angle of the tracks. The ϕ -strips have a 20° stereo angle in the inner region, and -10° in the outer region. The choice of the angle in the inner region is driven by the track reconstruction efficiency and ghost rates in the L1-trigger, as is shown in Fig. 3.3. The size and opposite sign of the stereo angle in the outer region follows from the condition to minimize the depth of the corrugations in the RF-shield.

Figure 3.4 shows a more detail schematic of the layout of the implants of the realistic R and ϕ -sensor. The R-sensor covers a few degrees more than 180° with its sensitive area to facilitate the alignment of the two halves of the VELO. For the ϕ -sensor it is not necessary to extend the sensitive area beyond 180° since

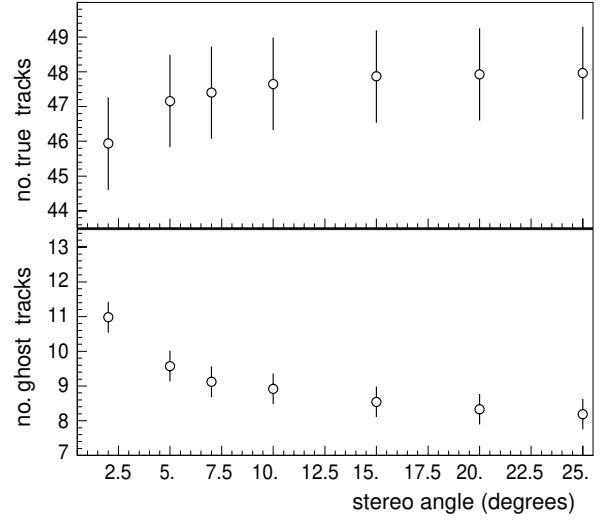


Figure 3.3: Performance of the track finding algorithm in the L1-trigger as a function of the size of the stereo angle in the ϕ -sensors. The same 500 events have been used with different stereo angles imposed, hence the errors are correlated.

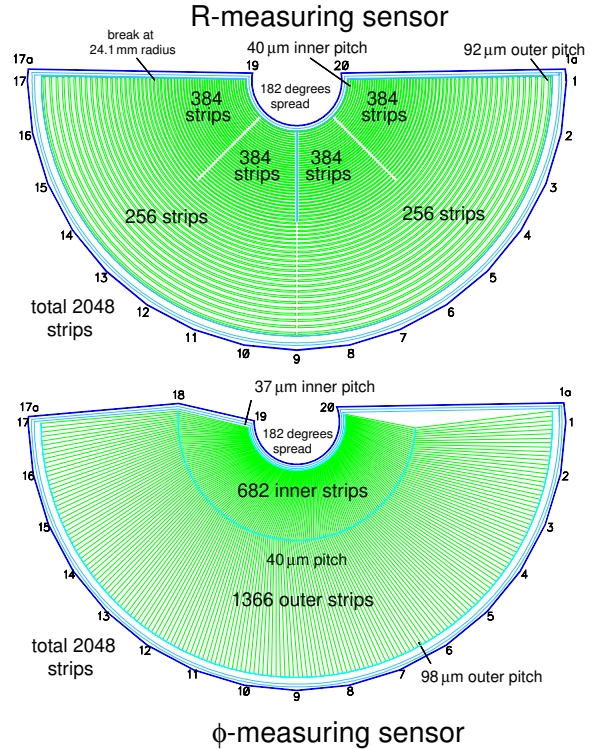


Figure 3.4: Schematic of the strip layout of the realistic R and ϕ -sensors, not showing the routing lines.

due to the stereo angle odd and even stations of opposite VELO halves will have a sufficient overlap for the alignment anyway. The guard rings which degrade the high voltage from the backside of the detector to the strips surround the whole detector and occupy a 1 mm wide band.

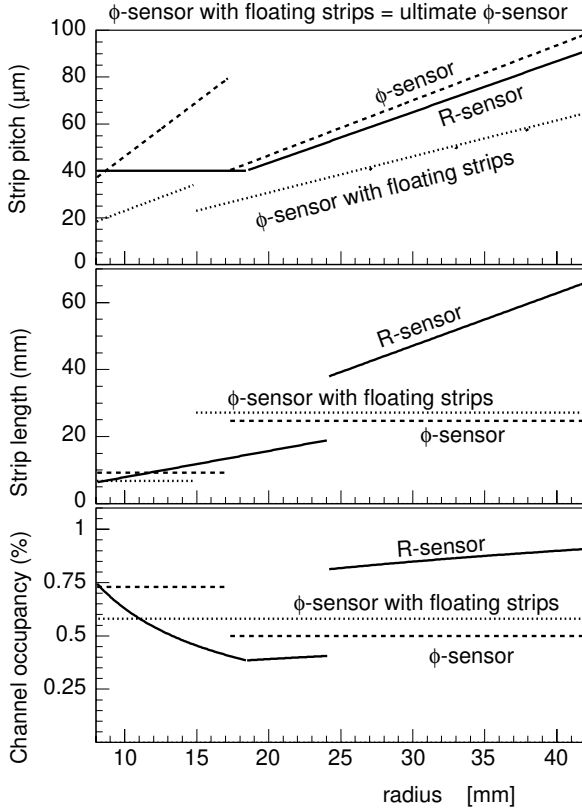


Figure 3.5: The strip pitch, strip length and occupancy for the realistic R-sensor, and the realistic and ultimate ϕ -sensor designs.

Figure 3.5 shows the strip pitch, length and expected occupancy for $2 \times r^{-1.8}$ particles/cm² per event (section 4.3) for the design shown in Figure 3.4. The pitch of the R-sensor is kept at 40 μ m below a radius of 18.5 mm, hence assuring that all tracks will have a first hit with the best resolution (see Fig. 3.1). At larger radii the pitch is gradually increased to a maximum pitch of 92 μ m at a radius of 42 mm. At a radius of 24.1 mm the strip length is doubled to reduce the numbers of channels, while keeping the occupancy below the 1% level. The realistic ϕ -sensor has strixels of 9 mm long in the

inner part, starting at a pitch of 37 μ m. The boundary between inner and outer part at a radius of 17.2 mm has been driven by the minimum pitch of around 40 μ m and the remaining allowed number of channels. In the ultimate ϕ -sensor design this condition would not be present, and in this case the boundary has been chosen to obtain a uniform occupancy. The ϕ -implants are tapered (similarly to the PR02- ϕ) to avoid low field, and consequently ballistic deficit, areas for the largest strip pitch region.

3.1.1 Operating conditions for the silicon sensors

A finite element analysis program has been used to simulate the temperature, depletion voltage and current flow for a non-oxygenated 300 μ m thick sensor [28]. The operating temperature was assumed to be the temperature of the part of the sensor glued to the hybrid. The operating conditions at the LHC have been simulated by a constant fluence for 100 days while keeping the sensor at -5° , followed by a warm up and access period of 14 days at $+22^\circ$ C, and by a cold (zero-flux) period for the rest of the year. The expected depletion voltage as a function of time is shown in Fig. 3.6.

Two fluences per year have been simulated, corresponding to the expected doses at 8 mm radius for the stations 7 (1.3×10^{14} n_{eq}/cm^2) and station 25 (0.5×10^{14} n_{eq}/cm^2). Varying the initial resistivity of the silicon and the assumptions about the parameterization of the damage effects in silicon does not change the results significantly. The model predicts depletion voltages almost twice as large as those measured for the prototype n -on- n sensors (see section 2.1.8). The spread in the depletion voltages of non-oxygenated sensors from different manufactures is known to be large. The behavior of the PR01 sensors is in better agreement with oxygenated sensors [43], for which a twice lower depletion voltage is expected compared to the one predicted for non-oxygenated sensors by the simulation package.

The bias voltage affects the amount of

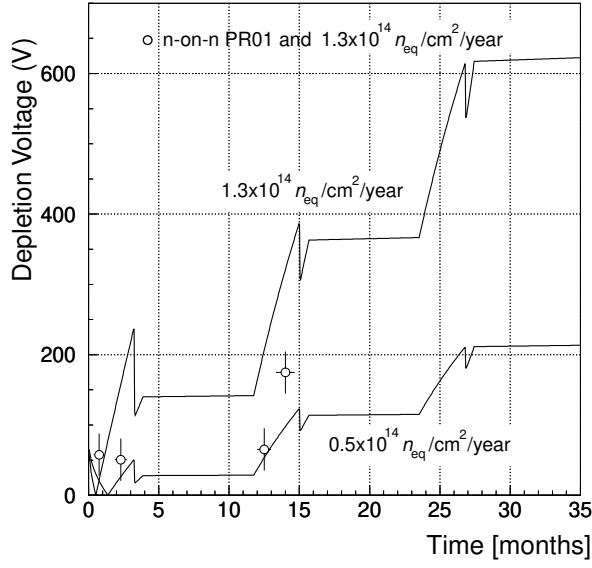


Figure 3.6: Predicted depletion voltages for a $300\ \mu\text{m}$ thick sensor as a function of time with an initial depletion voltage of $70\ \text{V}$ operated at -5° for a simple model of the LHC cycle and two different fluences per year. The data points are from sensor PR01, where the fluence has been converted to months of running by assuming $1.3 \times 10^{14}\ n_{\text{eq}}/\text{cm}^2$ per year.

power dissipated within the sensor. For detectors operating below 0°C a maximum of $0.1\ \text{W}$ is generated within the sensor. For operation in the temperature range -10°C to 0°C , bias voltages of up to $600\ \text{V}$ may be applied without changing the maximum temperature of the sensors by more than 1°C .

Under these conditions we predict that the realistic (even non-oxygenated) sensors may be operated fully depleted at these temperatures with a bias voltage of $400\ \text{V}$ for at least two years for the most conservative case. A bias voltage of just over $600\ \text{V}$ would be sufficient to fully deplete all types of sensors even after three years. The evaluated prototype *n-on-n* detectors (see section 2.1.8) are expected to survive up to four years at full depletion, while a 40% under-depletion is not expected to affect their performance significantly (Fig. 2.19), extending their lifetime even further.

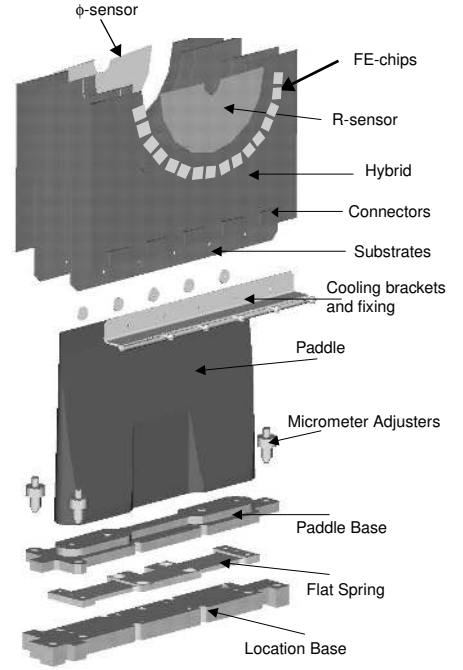


Figure 3.7: Schematic view of the module layout.

3.2 Modules

The LHCb VELO module performs three functions:

- it provides the mechanical infrastructure to support the sensors rigidly, stably and in a known position,
- it acts as the base on which the electronic readout for the sensor can be mounted,
- it allows the removal of heat from the front-end chips and sensor.

The key components (see also Fig. 3.7) of the module are:

- the silicon sensor,
- the FE-chips, mounted onto a thin kapton that is glued to a substrate,
- the substrate, which is attached to a cooling bracket,

- the substrate assembly, which is mounted onto a low mass carbon fibre paddle that separates the sensors from the platform,
- the paddle, attached onto a paddle base made of aluminium. The base is connected via a flat spring to a location base.

A summary of the material used in the module is given in Table 3.1.

The module is designed to allow the precision alignment of the sensors relative to the platform on which all modules are mounted. This is made possible by the incorporation of precisely machined location surfaces into the module (on the location base). The sensors can be moved in 3 directions (x , y , z) and rotated about three axes relative to the location surfaces. During the assembly the paddle is first glued to the paddle base and then the height and tilt of the sensors are adjusted with the micrometer screws relative to the location base.

3.3 Front-end electronics

3.3.1 System architecture

The key components of the front-end electronics architecture are shown in Fig. 3.8. One silicon sensor is read out by 16 front-end chips mounted on one hybrid. Five repeater cards per hybrid are mounted directly on the outside of the vacuum tank. Four cards drive the analog signals over twisted pair cables to the digitizer boards in the counting room at a distance of 60 m. One other repeater card receives the timing and control signals and the low voltage for the front-end chips as well as the bias voltage for the sensor. All analog data of one sensor are received and processed by one digitizer board. The low voltage and high voltage power supplies are situated behind the shielding wall in a radiation safe environment. The electronics can be divided into L0 electronics (front-end chips, hybrids) and L1 electronics (analog links, digitizer boards).

3.3.2 L0 Electronics

The L0 electronics deal with data before the L0 decision.

Front-end chip

A front-end chip for LHCb has to sample detector information with the LHC bunch crossing frequency of 40 MHz. The data have to be stored in the chip for the $4\mu\text{s}$ latency of the L0 trigger decision. In order to ensure safe operation of the VELO, the decision has been taken to store analog information, which allows the monitoring of pedestals and noise on a channel by channel basis and to subtract common mode noise in the digitizer boards as part of the hit finding algorithm. The most important design parameters for the chip are listed in Table 3.2 (for more details see Ref. [76]). The requirement about the tolerable signal left over after 25 ns (pulse spill-over) is derived from a study of the L1 trigger efficiency. If the signals left over are too high, the L1 trigger starts to reconstruct tracks from the previous bunch crossing and assign them a large impact parameter. The output of the L1 trigger will then be saturated by fake b-events. It had been shown [17, 77], that the trigger efficiency is not affected by a spill-over of less than 30%. With 30% spill-over, the number of clusters increases by $(2 - 3)\%$.

Two front-end chip candidates (SCTA_VELO and Beetle) will be described in this section. The final decision which chip to adopt for the VELO at the startup of the LHC will be taken in March 2002 at the latest after testing the functionality of both chips before and after irradiation.

SCTA_VELO: The SCTA_VELO front-end chip (Fig. 2.33) is derived from the SCT128A design [31] with the following main modifications:

- The pipeline is extended to 184 cells including 16 cells of de-randomizing buffer, in order to accommodate a latency of $4\mu\text{s}$.

	Material	Radiation length(cm)	Thickness (μm)	CTE ($\times 10^6$)	Conductivity $\text{Wm}^{-1}\text{K}^{-1}$
Sensor	silicon	9.3	300	2.8	130
Hybrid baseline composite backup composite	kapton	32.5	100	4	50
	CF(UD)	≈ 24	95	< 1	800
	TPG	24.9	300	< 1	1700
	CF(weave)	≈ 24	150	< 1	10
	beryllia	14.4	300	8.3	280
	TPG	24.9	300	< 1	1700
Thermal connector baseline backup	aluminium	8.9	300	23	202
	titanium	3.6	300	8.6	157
Paddle	CF2	≈ 24	200	< 1	10
Paddle base	aluminium	8.9	$\mathcal{O}(3\text{cm})$	23	202
Spring	steel	1.8	$\mathcal{O}(3\text{cm})$	12	669
Location base	steel	1.8	$\mathcal{O}(3\text{cm})$	12	669

Table 3.1: Material of module.

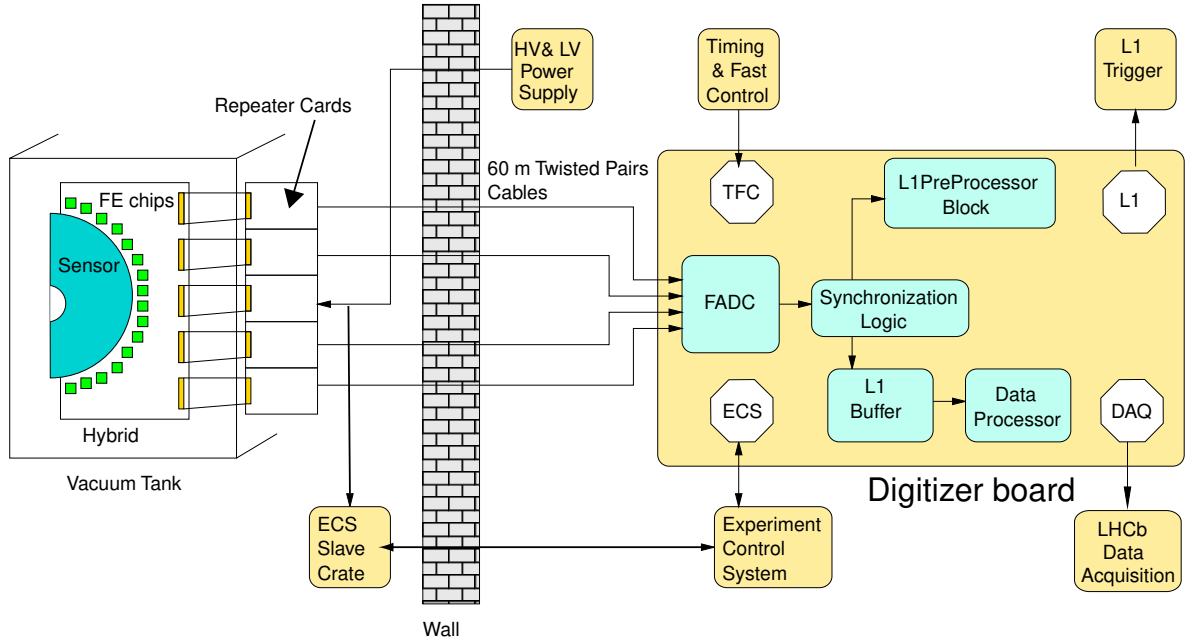


Figure 3.8: Front-end electronics architecture.

readout pitch	40-60 μm
channels per chip	128
detector capacitance	10 – 30 pF
required S/N	> 14
radiation hard to	$> 10 \text{ Mrad}$
power consumption	$< 6 \text{ mW/channel}$
peaking time	$\leq 25 \text{ ns}$
pulse spill-over	$< 30\%$ after 25 ns
dynamic range	$\pm 110,000$ electrons
required linearity	$\leq 5\%$ over full range
sampling frequency	40 MHz
L0 trigger rate	1 MHz
consecutive L0 triggers	yes
de-randomizing buffer	16 events
max. latency	4 μs ($160 \times 25 \text{ ns}$)
readout time	$\leq 900 \text{ ns/event}$
ECS interface	write and read of parameters I ² C [75] recommended

Table 3.2: Principal requirements of the front-end chip.

- In addition to splitting the multiplexer into four lines, the readout amplifier is redesigned to reach the required readout speed of 900 ns for a single event.
- Two samples with header information are added for each multiplexer, which allows the read out of the pipeline column number (PCN) in addition to the analog data of a triggered event.
- To program the chip and to read back the configuration parameters, a serial interface is added, which runs a reduced JTAG protocol [60].
- Finally, triggering on consecutive events is implemented.

The simulated pulse shape of the SCTA-VELO was already discussed in section 2.4.1. The total power consumption of the chip is expected to be $< 5.7 \text{ mW/channel}$.

Beetle: The block diagram of the Beetle chip [78] is similar to that of the SCTA-VELO. The chip can be operated as an analog, the

mode which will be used for the VELO, or alternatively as a binary pipelined readout chip. Current drivers transmit the serialized data and the pipeline column number off the chip within a readout time of 900 ns. The output of a dummy channel is subtracted from the analog data to compensate for chip induced common mode effects. All amplifier stages are biased by forced currents. On-chip digital-to-analog converters (DACs) with 10 bit resolution generate the bias currents and voltages. For test and calibration purposes a charge injector with adjustable pulse height is implemented for each channel. The bias settings and various other parameters such as trigger latency can be controlled via a standard I²C-interface. Details about the design and the performance of the chip are given in references [78] and [55], respectively.

The layout of the Beetle with the corresponding floor plan is depicted in Fig. 3.9. The die size is $(6.1 \times 5.5) \text{ mm}^2$. The analog input pads have a pitch of $41.2 \mu\text{m}$. A value below 2 mW/channel was found for the power consumption of the front-end amplifier. For the

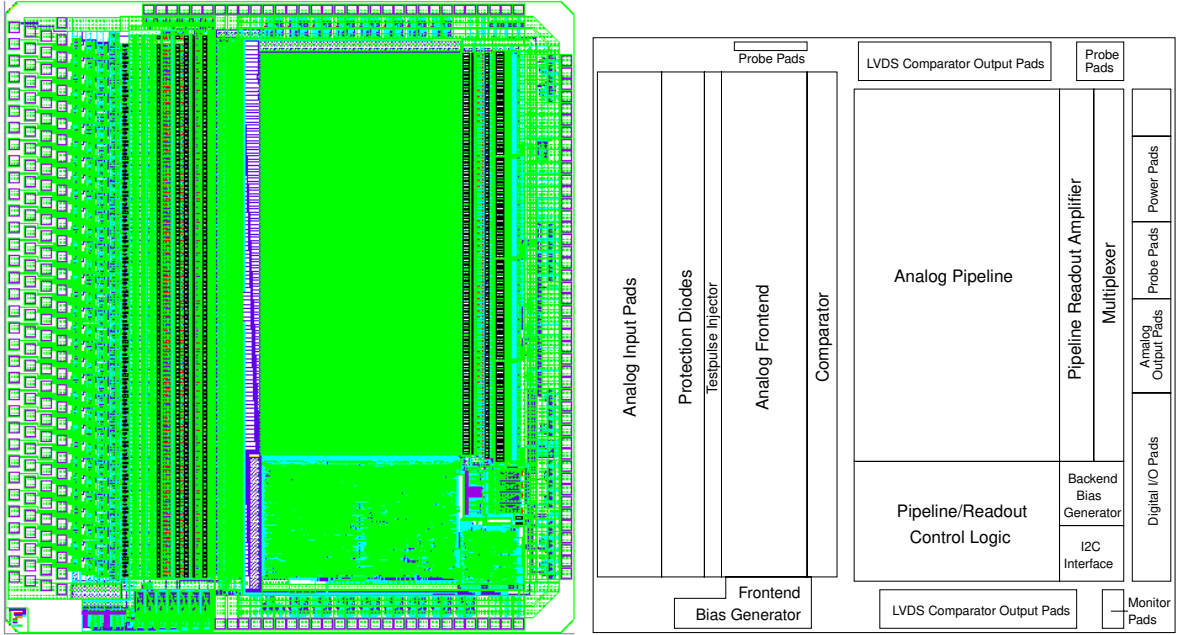


Figure 3.9: Layout of the Beetle readout chip with its corresponding floor plan.

complete chip a value of 4 mW/channel is expected.

The ECS interface

An important issue for the operation of the LHCb VELO is the slow-control interface or more generally the integration to the experiment control system ECS. In LHCb, the SPECS system derived from the SPAC bus [79] has been chosen as the preferred solution for the interface between front-end electronics and ECS. The chosen protocol for programming and reading the registers of the front-end electronics provides interfaces to both I²C and JTAG.

SPECS is a one-master n-slaves bus where the master is implemented in a PCI board sitting in a PC in the counting room. The bus requires four unidirectional differential pairs. The SPECS bus is fast (10 Mbit/s) and can extend up to 100 m. Up to 112 SPEC slaves can be addressed by one master [79].

Details about the design of the complete system are described in [80]. It is important to emphasize that the system is flexible enough to handle both the SCTA_VELO and

the Beetle front-end chips. For the cabling, cheap AWG26 Cat5 cables have been found to work for distances up to 100 m [81]. The SPECS master is implemented in an Altera 10k50E FPGA, whereas the slave will be implemented in an SEU immune antifuse technology. The slave acts as a transceiver and provides the necessary I²C/JTAG buses up to a length of 12 m. This allows the placement of the SPECS slaves at a distance where the radiation dose is below 100 Rad/year. On the front-end board the signals are repeated by active, radiation hard electronics. These repeater boards sit at the outside of the VELO tank and also carry a TTCrx chip [58] that provides trigger and timing information to the hybrid. The TTCrx chip is programmable via the I²C protocol.

Due to the compact design of the VELO, 7 SPECS slave boards providing up to 112 I²C/JTAG links can be located in a single crate close to the detector in order to connect 100 repeater boards, one per hybrid, to the SPECS bus. Only one link is needed to connect the crate to the SPECS master located in the counting room. The whole scheme is depicted schematically in Fig. 3.10.

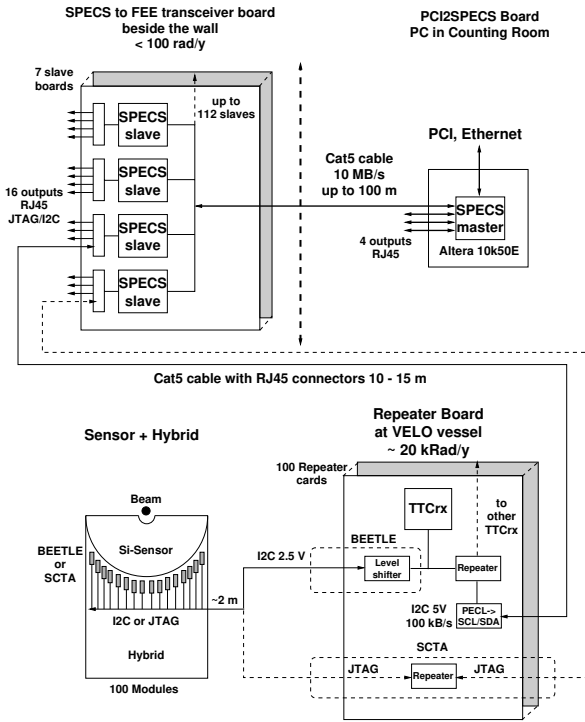


Figure 3.10: SPECS based front-end control. Dashed boxes show front-end chip specific parts.

Hybrid

Apart from providing the electronic support for the 16 front-end chips and the bias voltage for the sensor, the VELO hybrid acts also as mechanical and cooling support for the sensor. A prototype of an LHCb VELO hybrid has been built (Fig. 2.29). Its technical design is described in section 2.2. A second generation of prototypes is under design, which builds on the existing work but is fabricated on kapton. This hybrid will be able to carry the SCTA-VELO chip. The final hybrid will be based on these prototypes and is expected to differ only in details from the present design.

3.3.3 L1 Electronics

The L1 electronics deal with the data after the L0 decision. Its purpose is to digitize the analog data, preprocess data for the L1 trigger, store data during the L1 latency, do data reduction (zero suppression and common mode correction) and transmit the data to the LHCb data acquisition system after L1 accept. The

L1 electronics performs also data synchronization checks. The different components of the L1 electronics are:

- repeater cards located on the outside of the vacuum tank (Fig. 3.8),
- 60 m analog data transfer,
- digitizer boards in the counting room.

Repeater cards

The 64 analog outputs of one hybrid are connected to one digitizer board via four data repeater cards. One additional power/control card per hybrid provides low voltages to the front-end chips and the high voltage to bias the silicon sensor. In addition, each power/control card has a link to the ECS and to the TTC system to provide the front-end chips configuration and control signals. One TTC optical link connects the TTC system to a TTCrx chip on the power/control card, which converts the optical signal into LVDS Clock, Reset and L0 trigger signals.

Analog data transmission

The analog data are transmitted at 40 MHz rate via twisted pair cables to the digitizer boards which are placed at a distance of about 60 m in the counting room. A rad-tolerant amplifier [82] inside the repeater card is used to drive the small channel voltage levels (80 – 100 mV) of the front-end chips. A passive line equalizer in the link receiver compensates for the cable losses as described in section 2.4.2.

Digitizer board

The digitizer board (Fig.3.8) has, in addition to the 64 analog data links, four more input-output interfaces:

- Timing and Fast Control (TFC).
- Experiment Control System (ECS).
- L1 trigger (L1): An s-link interface [83] connects the digitizer boards with the L1 trigger farm.

- **Data Acquisition (DAQ):** An s-link interface that connects the digitizer board to the LHCb data acquisition system.

The Link Receivers digitize the analog data at a frequency of 40 MHz. The Synchronization Logic groups the event data coming via four analog links from each front-end chip. The event data are copied to the L1 PreProcessor (L1PP) and stored at the same time in the L1 buffer until the L1 accept/reject signal is issued. The L1PP performs event data reduction and sends clusters to the L1 trigger. The Data Processor removes the rejected events from the L1 buffers and processes the accepted events in order to create clusters to be sent out to the DAQ.

Link Receiver and Synchronization Logic: The Link Receiver consists of a line equalizer, an amplifier and an FADC. Four analog data streams, corresponding to the output of one front-end chip, are fed into four FIFO's controlled by one FPGA. To check synchronization, the 8-bit Pipeline Control Number (PCN) coming with the front-end chip data is compared with the PCN provided by an emulator. In case of an error the event is flagged accordingly.

L1 PreProcessor, L1 buffer and Data Processor: Each of the four L1 PreProcessor blocks processes the data of four front-end chips (= 512 channels). The data are stored in an input FIFO. A local memory which is loaded via ECS contains the pedestal and threshold values for every channel. Faulty channels can be masked. Data are corrected for common mode noise and a cluster finding algorithm is executed based on the threshold information. The clusters are stored into an output FIFO, which holds a maximum of 128 clusters. The L1 interface receives the clusters from the four output FIFO's, packs them together according to the format proposed in the L1 Trigger requirements document [84], encapsulates them according to the s-link protocol [85] and sends the event to the Read-out

Units of the L1 trigger. Events with more than 128 clusters per digitizer board are flagged and the additional clusters are ignored.

The same data that are sent to the L1 PreProcessor are also copied to the L1 buffer waiting for the L1 decision. The L1 buffer holds up to $\simeq 1900$ events and is implemented as one DMA memory of 512 kbyte for 8 input links.

After a positive L1 decision, the data are transferred from the L1 buffer to the L1 derandomizer buffer², where they remain until the data processor is ready to accept the next event. The output of the data processor is kept in the Output Buffer until it is transferred to the LHCb data acquisition system.

The Data Processor performs a similar data reduction as the L1PP but with a better precision and lower thresholds since it has about a factor 10 more time available. The Data Processor runs also a L1PP emulator process that allows to record in an LHCb event the input which was sent to the L1 trigger. A small fraction of the event data are recorded without zero-suppression for offline monitoring of the pedestals and noise per strip.

The processing is done by DSPs³ with a processing power of 2000 MIPS. Each DSP processes data from 8 input links. The L1 derandomizer buffer and the Output Buffer are implemented using the DSP internal data memory of 64 kbytes: 8 kbytes are used to implement a 32-event deep L1 derandomizer buffer; the remaining 56 kbytes are used to implement the Output Buffer. A cluster is coded using 6 to 12 bytes in the output data format: 4 bytes for the cluster address and L1 information and 2 to 8 bytes with the individual strip charge values. The average event size in the output buffer (assuming an average 1% occupancy) is 15 bytes per DSP, which corresponds to a total size of 12 kbytes per event for the full VELO. The maximum L1 accepted event size in the Output Buffer is 512 bytes: therefore in the worst possible case the Output Buffer is able

²<http://lhcb-elec.web.cern.ch/lhcb-elec/html/architecture.htm>

³TMS320C620X DSP Texas Instruments, <http://dspvillage.ti.com/docs/dspproducthome.jhtml>

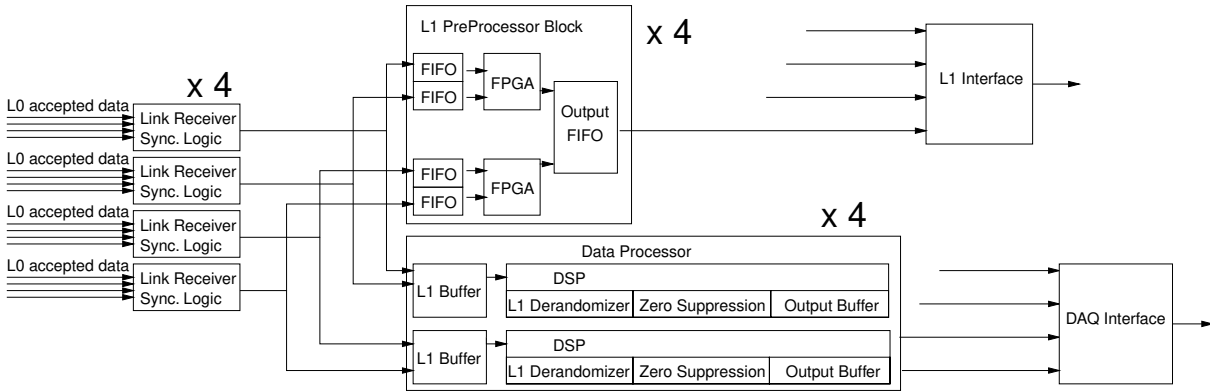


Figure 3.11: Data flow diagram of the digitizer board.

to retain more than 100 events. The data from the 8 DSP's on one digitizer board are multiplexed and packed according to the s-link protocol and sent to one read-out unit of the DAQ. At 100 kHz L1 trigger rate, the average data rate is 12 Mbytes/s, easily supported by existing s-link commercial cards⁴.

TFC and ECS interfaces: The TFC interface contains a TTCrx receiver chip, a front-end emulator and a timing/control FPGA. TTCrx is used to decompose the TTC optical signal into the 40 MHz clock and the fast commands (the reset commands for Event Identification, and the L1 accept/reject command). The front-end emulator holds a real front-end chip or an FPGA emulating the front-end chips digital logic. The L0 trigger is fed into the chip, and for each trigger the PCN header information is decoded and used for synchronization checks.

The ECS interface provides read and write access to the memories and FPGA registers on the digitizer board. The ECS controller is a Credit-Card-PC (CC-PC).

3.3.4 Power supplies

The VELO power supplies must provide:

- Low voltage for the L0 electronics,
- high voltage bias for the silicon sensors.

The required power supplies are summarized in Table 3.3.

The architecture of the power supply system follows the detector partitioning. Each hybrid has its own Low Voltage Module (LVM) and High Voltage Module (HVM). The LVM's and HVM's are hosted in a common crate located behind the shielding wall. The crate also hosts a Crate Controller Module (CCM) which provides the ECS CANBus interface⁵ and an Interlock Module (IM) to disable, according to external signals, the modules.

Low voltage modules

The LVM must provide:

- voltage for the analog part of the front-end chips;
- voltage for the digital part of the front-end chips;
- positive and negative voltage for the line drivers;
- voltage for the TTCrx and other components of the repeater boards.

The LVM's are insulated from the crate power supply and optically coupled to the CCM. Each voltage supply is powered by a separate line with its own return line. Remote sensing lines are present for both analog

⁴<http://hsi.web.cern.ch/HSI/s-link/devices/odin/>

⁵<http://www.can.bosch.com/docu/can2spec.pdf>

	Nominal Voltage [V]	Power [W]
FE analog		
SCTA	5	6
Beetle	2.5	4
FE digital		
SCTA	5	6
Beetle	2.5	4
Line drivers	± 5	60
TTCrx, other	5	2.5
Silicon	1 – 1000	< 5 W

Table 3.3: Power supply requirements.

(4 sensing wires) and digital (2 sensing wires) voltages. The LVM monitors voltages and currents and a hardware over-voltage and current protection is implemented. The hybrid temperature is also monitored at the LVM and in the case of overheating, voltages will be decreased or turned off.

High voltage modules

The HVM provides the sensor bias voltage up to 1 kV. The high voltage is supplied by a coaxial cable; the cable shielding acts as return path. The HVM is insulated from the crate power supply and optically coupled to the CCM. The output voltage and current are monitored. In addition to hardware protection against over-voltage and over-currents, a programmable ramping up and down procedure is implemented.

Crate controller module

The main job of the Crate Controller Module is to communicate with the ECS via CAN-bus, and with the LVM and HVM. All voltage settings, ramping parameters, current-voltage limits, temperature limits, on-off commands are set by the ECS and sent to the appropriate module; information about voltages, currents, temperature, trip conditions and status of modules are collected and sent to the ECS. A local command and monitoring mode used in maintenance and test phases is available.

Cables

The low voltage, high voltage and sensing cables run from the power supply crate in the counting room to the VELO vacuum vessel; each line has its own return cable. The cable length is of the order of 40 – 60 m.

Each high voltage line consists of one coaxial cable, with the shield connected to ground for safety reasons. Each low voltage supply line consists of 2 conventional cables: the use of multi-conductor cables can reduce the amount of low voltage cables in the cavern.

3.3.5 Grounding scheme

The partitioning of the VELO electronics follows the detector topology. Each silicon detector with its hybrid forms a group. There is a total of 100 VELO hybrids with 16 front-end chips each.

As a general rule, the groups are as much as possible electrically isolated from each other. In particular, there is no electrical connection between an R- and ϕ -hybrid within one module. The power distribution and the grounding scheme must follow this partitioning. The number of groups connected to the same power supply is kept as small as affordable.

The VELO detector grounding scheme will follow the basic rules which will be defined for the whole LHCb experiment.

The general scheme to prevent the generation of low impedance ground loops is to use a tree connection terminated at a common

grounding point. The VELO detector tree grounding scheme will have the common point located on the hybrid side and will follow the partitioning described above. When required, capacitors and/or resistors will be used to decouple on and off detector electronics. We give a short description of the implementation for the relevant subsystems.

- **Low voltage power supplies:** The low voltage power supplies (less than 50V) are grounded at the hybrid side (see Safety connection).
- **High voltage power supplies:** The range of voltages required is below 1 kV. The VELO uses a coaxial cable with the shield connected to ground at the power supply side for safety reasons. The HV power supply is grounded via an appropriate resistor at the detector side.
- **Safety connection:** The safety point location for LHCb in the cavern will be defined mid-2001. All the VELO mechanics parts such as the vacuum system, cooling system and RF shield, are connected to the beam pipe. The ground point must never be interrupted. The following options have been identified:
 - connection of the hybrids to ground via the cooling pipes
 - connection via the mechanical hybrid support
 - connection to a point outside of the tank, using an extra line.

The final choice will be done after an *in situ* optimization, which will attempt to reduce the electronic noise that may be induced by this connection.

- **Signal links:** All the analog data and the control lines use shielded twisted pairs. The shield of the cable is connected to the repeater card ground and is decoupled by a capacitor at the digitizer board.

3.4 Mechanics

The mechanical structure that houses the silicon detectors (more details can be found in Ref. [8]) differs considerably from the one described in the Technical Proposal [1], in particular with respect to the vacuum envelope, detector support frames and *xy*-table.

Firstly, requirements are listed, imposed by both the LHC machine and the LHCb experiment, which the design of the vacuum vessel and support structures of the vertex locator need to meet.

LHC requirements:

- Beam-induced bombardment inside the vacuum vessel must be low enough that effects on the beam lifetime and stability are kept at an acceptable level [86].
- During data taking the silicon detectors are placed at 8 mm from the circulating protons. However, during injection the required half aperture amounts to 27 mm [87]. The complete silicon detector array and encapsulations must be retractable such that no material remains within this radius during beam injection and ramping.
- The VELO should not degrade the LHC beam conditions by parasitic RF coupling.
- No LHCb-specific failure scenario should lead to an (expected) downtime for the LHC that exceeds two weeks.

LHCb requirements:

- The acceptance of the vertex detector will be $300 \text{ mrad} \times 250 \text{ mrad}$ (*horizontal* \times *vertical*). Multiple scattering in the vacuum envelope, wake field suppressors and exit window should be kept to a minimum. The geometry should be such as to be compatible with subsequent detectors (e.g. T1 and RICH1).

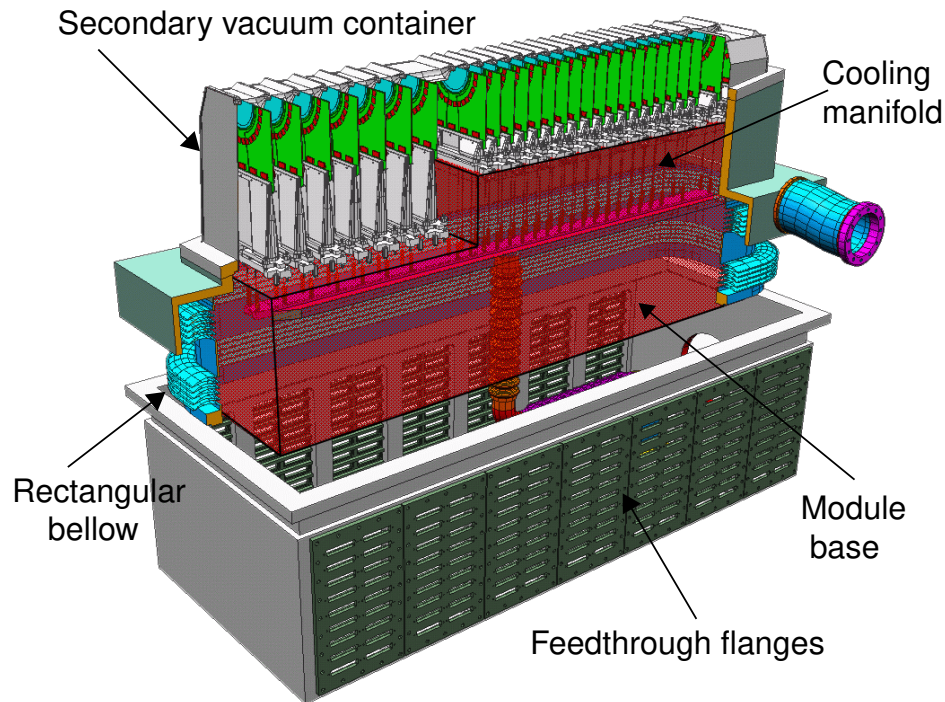


Figure 3.12: Three dimensional view of one detector half (rotated by 90°) showing the silicon detector modules fixed on the support frame, the cooling capillaries and the manifold.

- The silicon detector planes must be positioned with respect to each other with an accuracy of better than $20\ \mu\text{m}$ [1].
- The detector halves must be aligned to each other with an accuracy better than 100, 100 and $500\ \mu\text{m}$ in the x , y and z directions, respectively [1].
- It should be possible to remotely move the detectors in the two transverse directions with respect to the beams by $\pm 5\ \text{mm}$ from the nominal beam axis.
- When retracting or moving in, it should be possible to stop the detectors at an arbitrary intermediate positions and to operate the VELO for finding the beam position by tracking.
- The positioning of the VELO detector halves must be reproducible with an accuracy better than $50\ \mu\text{m}$ [1].
- The VELO mechanical design must accommodate a cooling system such that the silicon detectors can be maintained at their operating temperature (which will be between -25°C and $+10^\circ\text{C}$).
- Heat load and RF pickup due to wake fields must be minimized by suitable choice of the geometry (e.g. vacuum envelope) and specific wake field suppressors (see section 2.5.2).
- The VELO mechanical design should take into account the high radiation levels in the LHCb environment.

3.4.1 Mechanical design

The VELO contains silicon strip detectors as active elements (see section 3.1). These detectors are organized in two halves (one on each side of the beam axis) each containing 27 modules. A single silicon detector module contains

both an R- and a ϕ -silicon plane and their hybrids with the front-end electronics. The two most upstream modules of each half only contain an R-measuring plane and are used as a pile-up veto counter for the L0 trigger (see Ref. [3]). The silicon detectors, including hybrids, cabling, connectors and cooling system will be operated in a so-called secondary vacuum system (separate from the machine vacuum). The implementation of 22,000 electrical feedthroughs has been taken into account. Fig. 3.12 shows a three dimensional view of one VELO detector half. The detector modules are mounted on an aluminium support box with pins and clamping bolts in such a way that the modules can be replaced and repositioned with an accuracy better than $20\text{ }\mu\text{m}$. Before installation of both detector support boxes into the secondary vacuum containers, alignment of the detector modules will be performed to the required accuracy with respect to each other.

A thin aluminium box is used as a boundary between the primary LHC vacuum and the secondary detector vacuum. Moreover, this encapsulation acts as a wake field suppressor. The encapsulation comprises an advanced mechanical structure. Prototypes are being fabricated and their properties (with respect to vacuum, RF shielding, *etc.*) will be tested (see section 2.5.1). The aluminium envelope of the silicon stations must be electrically connected to the exit window to guarantee appropriate wake field suppression and to prevent possible sparking in this transition region. This constitutes a delicate design issue and a prototype design based on corrugated strips is shown in Fig. 3.13. The connections consist of segmented half tapers fabricated from (19 cm long and $70\text{ }\mu\text{m}$ thick) corrugated copper-beryllium strips. The downstream tapers are connected to the interior of the LHCb beam pipe by a press-fit connection. The corrugations are needed to allow for mechanical motion of the detector housings relative to the vacuum vessel and exit window.

A front view of the mechanical design of the VELO is shown in Fig. 3.14. The vacuum vessel and associated vacuum pumps rest on

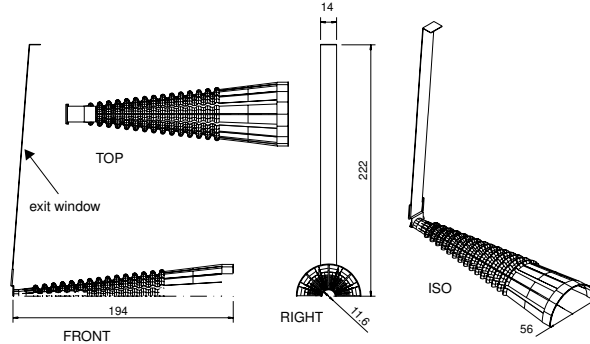


Figure 3.13: Prototype design of the wake field suppressors connecting the thin-walled aluminium box to the beam pipe sections.

a concrete stand. Large rectangular bellows allow precise movement (in the transverse directions) of the detectors during data taking as well as complete retraction of the detector elements prior to filling and dumping the beam. These large rectangular bellows decouple the complete VELO detector system from the primary vacuum vessel. The detector halves are attached to a frame which can be moved in the two transverse directions relative to the concrete stand. All motors, bearings, gearboxes and chains of the positioning system are outside the vacuum. Coupling to the frame is done via bellows.

Fig. 3.15 shows that installation of the fragile secondary vacuum system is performed by removal of the upstream spherical flange. After bake out and venting with ultra-pure neon, the detector halves can be installed via the two large rectangular openings in the sides of the vacuum vessel. The design accommodates 440 feedthrough connectors (50-pin D-type glass-ceramic) to transport the detector signals to the off-detector electronics. After insertion into the vessel, the detector halves are detached from the large feedthrough flanges and mounted to the inner support frames which are coupled to the positioning system. A horizontal cross section of the VELO assembly is depicted in Fig. 3.16, where one can see the two detector halves installed in their containers, inside the primary vacuum chamber.

The exit window (see Fig. 3.16) is mounted

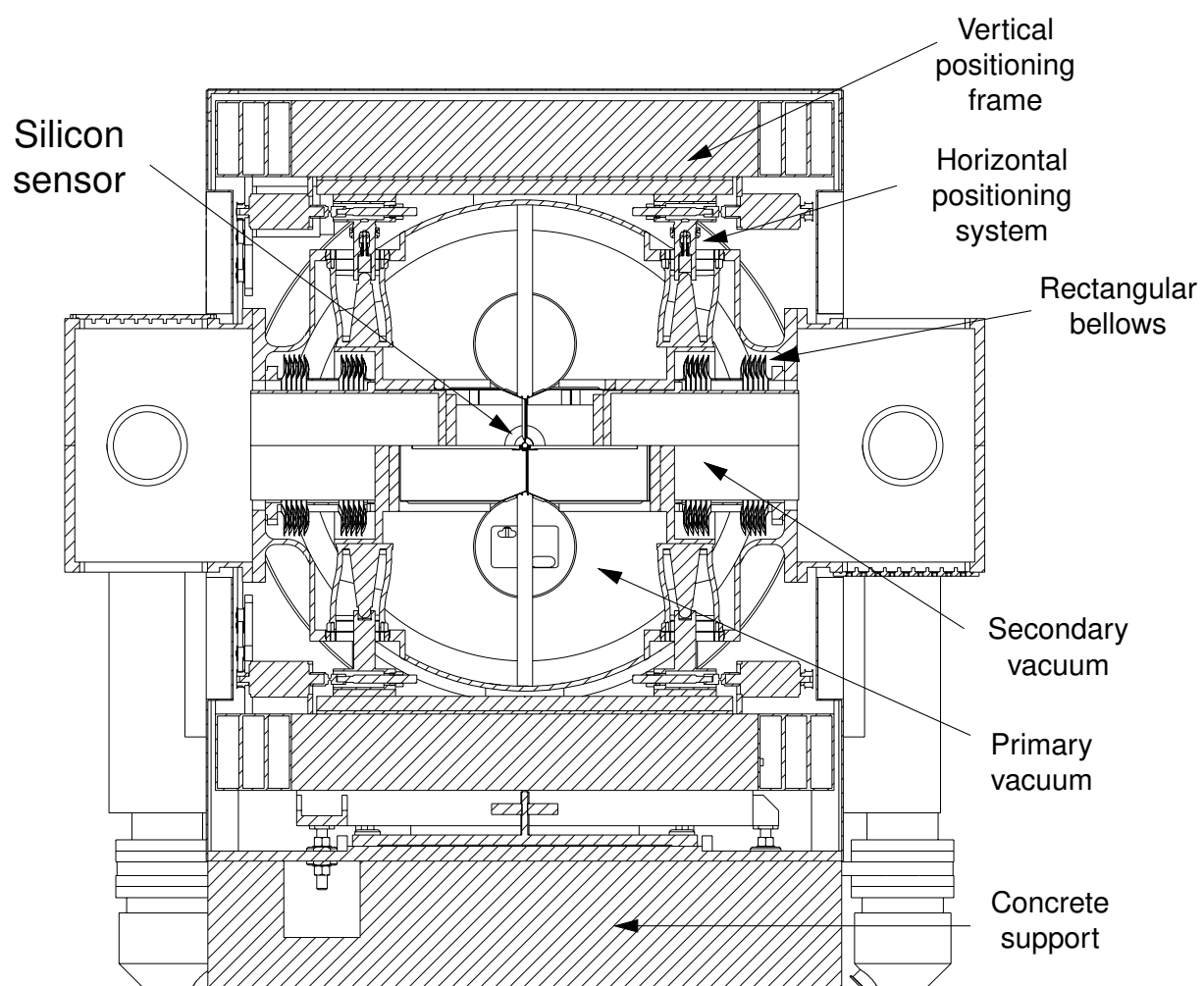


Figure 3.14: Front view of the VELO showing the detector positioning system.

on the vertex detector primary vacuum chamber by a circular flange. It is designed with a diameter of 760 mm for a track clearance of $300 \text{ mrad} \times 250 \text{ mrad}$. Finite element analysis calculations were performed to determine the appropriate geometries for both the exit window⁶ and the vacuum chamber [89]. In this way it was ensured that the design complies with the D2 safety code⁷ regulations.

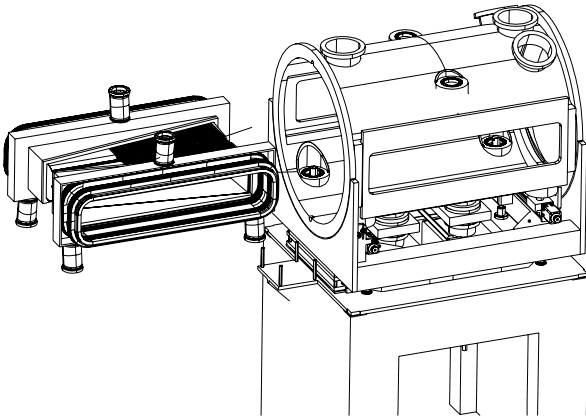


Figure 3.15: Installation of the thin-walled secondary vacuum containers into the VELO primary vacuum system.

In case of a failure which requires removal of the secondary vacuum containers, an emergency wake field suppressor can be installed in the vacuum vessel to provide a conductive (cylindrical) connection between its two ends. This pipe will have holes for vacuum pumping and, if necessary, will be coated with adequate materials. For the more severe scenario where one must remove the exit window and LHCb beam pipe, an emergency pipe will be available, which can be installed throughout the VELO vacuum vessel (leaving the latter at atmospheric pressure). In this way, repositioning of the primary vacuum vessel and detector support frames can be avoided. The design of this emergency pipe will be taken over from the design of a standard LHC warm straight section.

⁶As the exit window is part of the LHCb beam pipe, design and fabrication work has been transferred to CERN/LHC-VAC [88].

⁷CODE DE SÉCURITÉ / SAFETY CODE D2 Rev. 2.

3.5 Vacuum system

The silicon strip detectors are operated in vacuum, since this allows for positioning the sensitive area close to the beam and reducing the amount of material traversed by particles. The vacuum system design described here resembles in several aspects the one proposed in Ref. [90]. To minimize the contamination of the primary (LHC) vacuum, the detector modules are placed in a secondary vacuum container. The secondary vacuum is separated from the primary vacuum by a thin-walled structure. As a consequence, the design must include a protection scheme against possible failures that would lead to an increase of the pressure difference across the thin wall. Electrically activated valves controlled by differential pressure switches will be applied. In addition, the use of a protection mechanism will be included that does not depend on any sensing device or external supply (power and compressed air).

3.5.1 Layout

The VELO vacuum system consists of three communicating sections, namely the VELO primary vacuum vessel, the LHCb beam pipe and the silicon detector housings, as schematically shown in Fig. 3.17. These sections are not independent vacuum systems: none of the section can be brought to atmospheric pressure individually. The VELO primary vacuum vessel and LHCb beam pipe are part of the LHC primary vacuum system.

The LHCb beam pipe extends throughout the complete LHCb detector (length of $\approx 18 \text{ m}$) and currently consists of three tapered, thin-walled pipes connected to each other (for the material, Al, Al-Be alloys and stainless steel are being considered). On the VELO side, the pipe ends with a curved $\text{Ø}760 \text{ mm}$ and $\approx 2 \text{ mm}$ thick Al window (the VELO exit window). The window is welded to the LHCb beam pipe. The interior of the LHCb beam pipe will be coated with low activation temperature NEG⁸ [9]. These will be

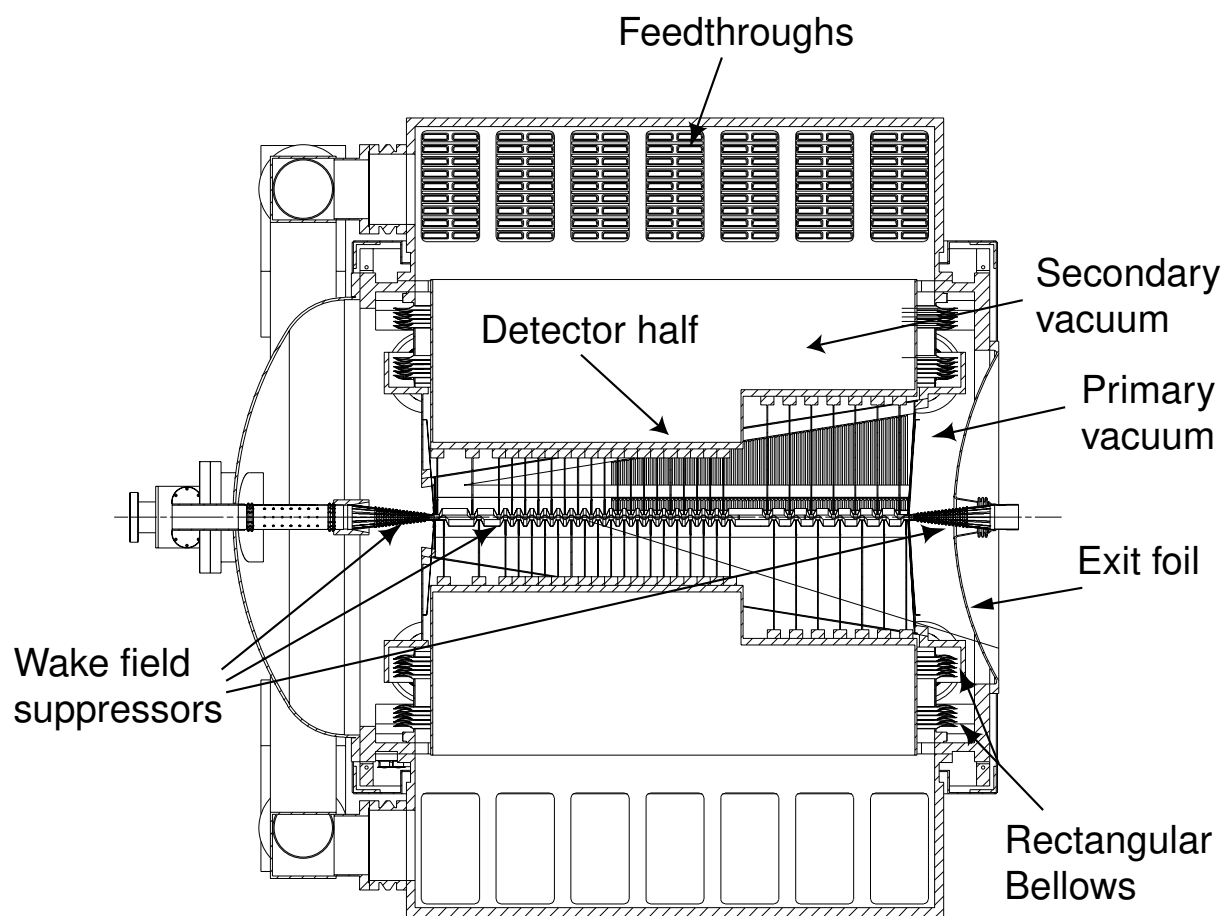


Figure 3.16: Horizontal cross section of the VELO showing the primary and secondary vacuum system. Rectangular bellows allow movement of the detectors in the horizontal plane over ± 30 mm.

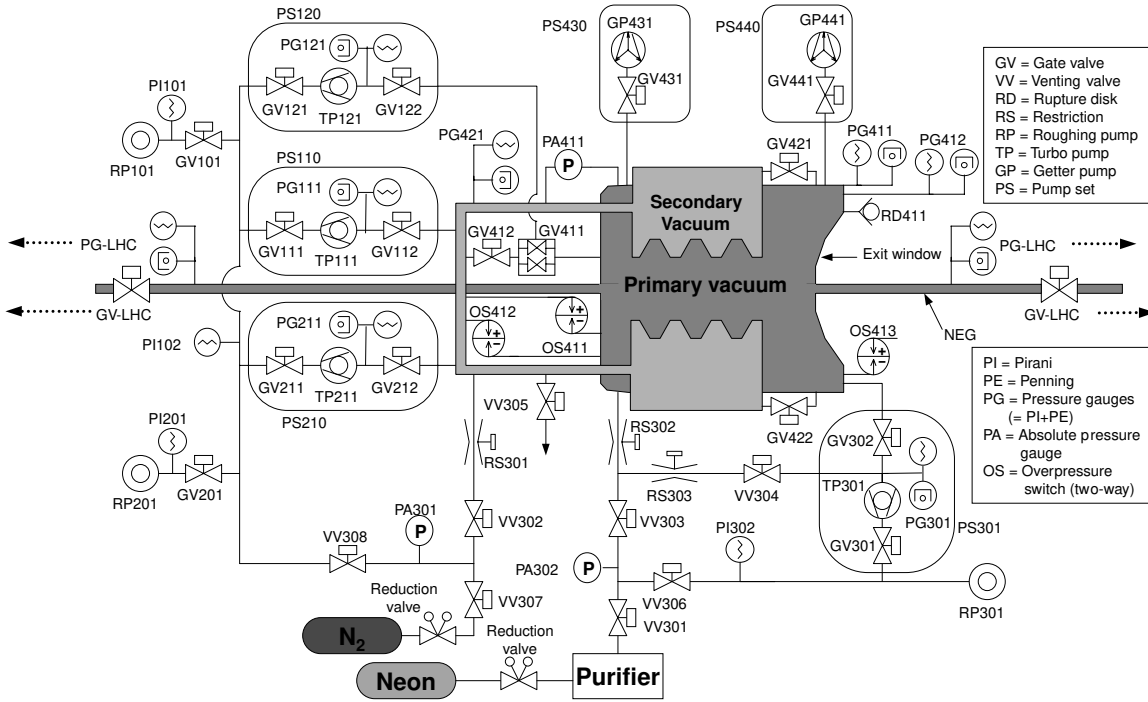


Figure 3.17: Layout of the vacuum system and controls.

activated in-situ by baking the LHCb beam pipe to 200°C for about 24 hours. The NEGs can be vented with clean gas and reactivated later (under high vacuum) without substantial loss of their pumping speed. However, because of their limited capacity, it is expected that after several such cycles the NEGs pumping speed will drop substantially. In the case of the LHCb beam pipe, it is not yet known whether the full pumping speed of the NEGs will be needed to ensure acceptable (static and dynamic) vacuum conditions for the LHC. If not, the maximum number of venting cycles could be somewhat larger. Reactivation at higher temperature (about 250°C) and/or for longer times could be considered to increase the lifetime of the NEG coating [91]. To avoid bake-out after a venting/pump-down cycle, a well-established procedure using ultrapure inert gas (probably neon) will be applied, as is routinely done in e.g. the CERN EST/SM laboratories. The servicing procedures (NEG-preserving venting and subsequent pump-down, normal venting and sub-

sequent pump-down, bake-out of VELO and LHCb beam pipe) are described in detail in Ref. [10].

The VELO vacuum vessel is a 1 m diameter stainless steel vessel of about 1.8 m length which is evacuated by two powerful ion pumps (combined with Ti-sublimation pumps). The VELO vacuum vessel can be baked out in-situ to 150°C. During bake-out, the silicon detectors are not in the secondary vacuum vessel. The nominal static pressure of the baked-out VELO vacuum chamber is expected to be in the 10^{-9} mbar range, the residual gas being mostly H_2 and CO.

The main function of the Si detector housings is to protect the primary vacuum from excessive outgassing rates and to reduce RF coupling between the LHC beams and the VELO. The detectors can be removed without exposing the primary vacuum to ambient air. The detector housings protrude inside the primary vacuum vessel. In the current design, the sides of the housing which fall within the LHCb acceptance are made of 0.5 mm Al. The side fac-

ing the beams is made of 0.25 mm Al. The two detector housings are evacuated by two turbomolecular pump stations.

The LHCb beam pipe, besides being a fragile vacuum structure, constitutes a sensitive part of the high vacuum system because of the active NEG coating. Several options are being studied to ensure that the interior of the primary vacuum system will be minimally exposed to ambient air during an access to primary vacuum components. One of the options, for example, is to enclose the LHCb VELO and RICH1 sub-systems in a clean area with a controlled atmosphere (low humidity, dust-free). In any case, the VELO setup will be located in a closed and possibly restricted area for reducing risk due to human action. Furthermore, all servicing and maintenance operations on the VELO setup will be performed exclusively by qualified personnel.

The complete vacuum system will be controlled by a PLC unit backed with an uninterruptible power supply and interfaced to the LHC and LHCb SCADA systems (via e.g. ethernet). In addition to this software interface, hard-wired interlocks between LHC and LHCb will be implemented, for example for operation of the sector valves.

3.5.2 Protection devices of the LHCb vacuum system

Two kinds of safety valves are used to protect the thin separation foil (detector housing) from an irreversible deformation, or rupture, in case of a pressure increase on either side of the foil. A differential pressure switch is used to open an electrically activated valve whenever the pressure difference between the primary and secondary vacua rises above a value $\simeq 1$ mbar. If the pressure difference exceeds the value $\simeq 5$ mbar, then the gravity-controlled valve (see section 2.5.3) opens under the direct effect of the pressure independently of any electrical power or pressurized air supply. The purpose of these safety valves is to maintain the pressure difference below $\simeq 17$ mbar, the value above which the thin-walled detec-

tor housing is expected to deform irreversibly. Note that, at this pressure, the largest (permanent) displacement on the encapsulation is about 0.3 mm. The actual rupture pressure of the encapsulation is expected to be several hundred mbar [89].

The effect of a leak in the LHCb vacuum section on its neighboring sections should be minimized, and vice versa. The implementation and impact of fast separation valves between LHCb and its neighboring LHC sections are under study. Furthermore, to protect the LHC ring vacuum against possible human-induced mishaps, the sector valves around LHCb will be automatically closed whenever access to the experimental area is granted.

The LHCb equipment will be divided into subsystems, each having its own battery backup (Uninterruptible Power Supply, UPS). These UPS's can take over instantly after a power failure. However, their autonomy time is about 10 minutes. To protect against longer power failures, LHCb will rely on a high-power diesel generator. Since the take-over time of such a generator is of the order of one minute, the distributed UPS's are indispensable. In the case of the VELO, all PLC units, vacuum valves and monitoring devices (gauges, temperature sensors, *etc.*) will be backed up by UPS. The vacuum pumps are not backed up by UPS, but can be powered up by the diesel generator.

3.5.3 LHCb vacuum: effects on LHC operation

LHC constraints on the residual pressure in the primary vacuum vessel are rather loose. For instance, a modest pressure of the order of 10^{-7} mbar (H_2 at room temperature) would contribute negligibly to the integrated density over the LHC ring. More important are possible beam-induced effects which result from the bombardment of the surfaces surrounding the beams by photons, electrons or ions. These phenomena can result in a local 'run-away' of gas density or electron cloud density. Dynamic pressure effects have been simulated by the

CERN LHC-VAC group [92] for a (now obsolete) version of the VELO design which did not allow for bake-out of the primary vacuum walls. The model included ion- and photon-induced desorption, but no electron-induced desorption. The latter contribution is expected to be negligible (unless strong electron multipacting effects take place). It was assumed that the NEG coating in the LHCb beam pipe does not contribute to the pumping speed and that its desorption coefficients are as of an active NEG-coated surface. The pressure profile in the presence of the two beams was calculated numerically for increasing beam current. The current at which the pressure diverges is called the *critical current* and is required to be larger than 3.4 A ($2 \times 2 \times 0.85$ A, where the first factor of 2 is a safety factor, the second one is for the two beams). A number of instructive conclusions can be drawn from the results of these simulations, the main one being that by optimizing the geometry of the detector encapsulations (thereby increasing the linear pumping speed along the beam axis) it is possible to raise the critical current above the required value.

On the basis of the above considerations, one does not expect ion- and photon-induced desorption phenomena to be an obstacle to normal LHC operation. Moreover, with the latest design of the VELO (see section 3.4), which allows for baking out the primary vacuum surfaces, ion- and photon-induced phenomena are expected to be negligible.

Preliminary studies have shown that electron cloud build-up may occur when the VELO is in the open position. The effects on the gas pressure may be tolerated due to the large pumping speed. However, the emittance increase due to electron space charge has yet to be assessed. A coating with low secondary electron yield on the detector encapsulation might be necessary.

3.5.4 Risk analysis

A risk analysis was carried out for the VELO to first identify critical parts of the system

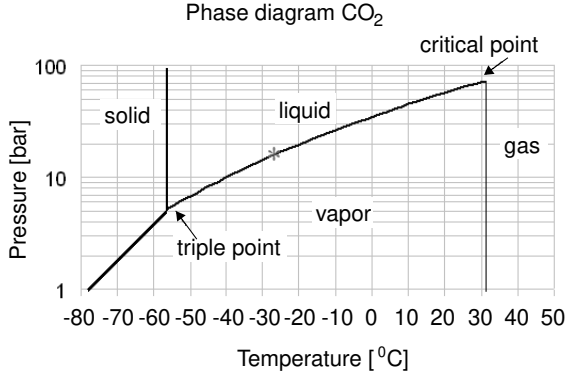
and their possible failure scenarios, then to estimate the associated damage (essentially, the downtime for LHC) and finally to define a number of requirements (tests and precautions) to be fulfilled in order to bring the system to a level of acceptability compatible with LHC standards. The detailed risk analysis is discussed in Ref. [15]. The main conclusion is that, even in the worst scenario (rupturing of the exit window or LHCb beam pipe), the downtime for LHC is not expected to exceed two weeks.

3.6 Cooling

A cooling system must be provided that allows operating the silicon detectors at a temperature adjustable between -25° and $+10^\circ$ C, while the temperature of the electronic components should be kept below 40° C. The total heat produced in the detector amounts to 1.2 kW. Including blackbody radiation from neighboring parts and a safety factor of 1.5, the required cooling capacity is about 2.5 kW. The cooling system must be radiation resistant and the amount of material around the detector should be minimized in order to limit the undesired production of background. Furthermore, due to the required high positioning accuracy of the detector, temperature gradients should be kept minimal.

A two-phase cooling system has been selected with CO_2 as a cooling agent. Refrigerant R744 (CO_2) has excellent cooling properties⁸. CO_2 is widely used as a cooling agent in radiation environments. No free radicals and toxic compounds are expected to be produced in the high-radiation environment of the VELO and the formation of carbon is inhibited by the high recombination rate. The pressure drop over the cooling capillaries in the mixed phase, which depends on the volume ratio between vapor and liquid, compares favorably for CO_2 . As a result, the dimensions of the

⁸For a review of different cooling agents, we refer to the review of the Air-Conditioning and Refrigeration Technology Institute in Arlington, VA, USA; see Ref. [93].

Figure 3.18: Phase diagram of CO₂.

cooling tubes can remain small. Tests showed (see section 2.5.4) that 5 W/cm of heat transfer can be accommodated with stainless steel capillaries that have an inner/outer diameter of 0.9/1.1 mm [72, 7]. Under normal working conditions the pressure varies between 15 and 35 bar, while the pressure at room temperature is about 57 bar (Fig. 3.18). This is well below the rupture pressure of the stainless steel capillaries considered here. Moreover, in the temperature range of operation, the pressure dependence of the vaporization temperature of CO₂ is less than 2 K/bar, whereas the pressure drop over the capillary is less than 0.5 bar. As a result the cooling tube is expected to be isothermal within one degree.

Figure 3.19 shows an outline of the cooling system, which consists of two main circuits. The primary circuit (CO₂) transports the heat from the detectors to the secondary circuit. The latter circuit contains R507 as a coolant (a mixture of CHF₂CF₃ and CH₃CF₃) and transfers the heat to cooling water. If one uses the returning CO₂ refrigerant to pre-cool the incoming liquid through a heat exchanger, the cooling capacity for one kilogram of CO₂ amounts to 294 kJ/sec. Therefore, the 2.5 kW requires a flow of 8.5 g/s. Refrigeration of the detector modules is performed via 54 parallel cooling channels (one per module) and the system has been designed for a 17 g/s flow of liquid CO₂.

From the main supply line the liquid is expanded into the capillaries via flow restric-

tions (Ø0.85 mm wires of 40 mm length inserted in each capillary). The temperature of the coolant in these capillaries is set by controlling the pressure on the return line (typically 15 bar). The capillaries and flow restrictions are vacuum-brazed to a manifold. The supply and return lines are welded to the manifold. No tube fittings are used inside the vacuum. The CO₂ system is filled with the coolant at room temperature up to a pressure of about 40 bar. The complete cooling circuit is designed (and will be tested) to sustain a pressure of at least 200 bar, well above the equilibrium pressure of CO₂ at 30°C (72 bar). The total amount of CO₂ in the system is relatively small, of the order of 5 kg, which corresponds to approximately 2.5 m³ at STP (CO₂ is considered to be toxic in air when its concentration exceeds 5%). Of this amount, only about 100 g is present in the tubing inside the secondary vacuum system. Note also that the pump and compressor units will be located in the accessible area (behind the shielding wall). A more detailed description of this cooling system can be found in Ref. [7].

3.7 Material budget

The material budget distribution of the VELO as a function of the pseudorapidity η and the azimuthal angle ϕ was studied using GEANT3 [94]. 'Geantino' particles were tracked through the detector material. At the boundary of each volume, the distance and the material traversed were recorded and the X_0 of each step was calculated. The 2-dimensional distribution of the integrated X_0 of a particle at the exit of the VELO in the $\eta - \phi$ plane is shown in Fig. 3.20. The dark band at $\eta \approx 4.3$ is due to geantinos that exit the VELO through the 25 mrad conical section of the beam pipe; this material is discarded when calculating the numbers presented here and in Fig. 3.21. The remaining structures observed are due to the components of the VELO (Table 3.4). The region around $|\phi| > 80^\circ$ has an increased concentration of material due to the overlap of the two detector halves.

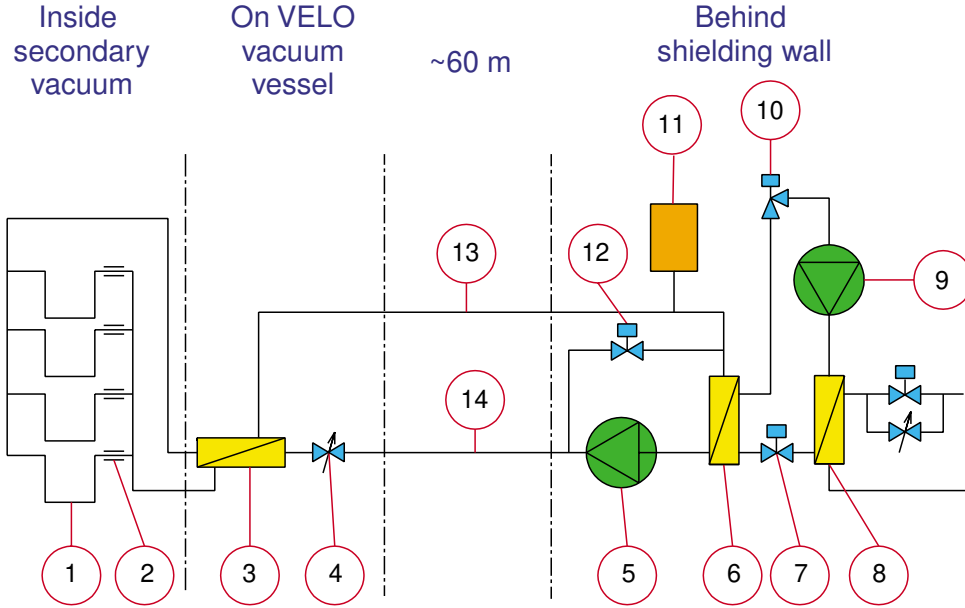


Figure 3.19: Outline of the mixed-phase CO₂ cooling system. (1) Cooling capillary, (2) flow restriction, (3) heat exchanger (cold gas / warm liquid), (4) needle valve to set total flow, (5) liquid CO₂ pump (CAT), (6) heat exchanger (condensor for CO₂, evaporator for R507), (7) thermo-expansion valve (R507), (8) water-cooled R507 condenser, (9) R507 compressor, (10) evaporator pressure regulator, (11) CO₂ gas storage, (12) pressure regulating valve set at 70 bar, (13) gas return line (inner Ø12 mm), (14) liquid supply line (inner Ø6 mm).

Item	x/X_0
RF foil	0.090
Wake-field guide	0.004
Exit window	0.019
Silicon	0.053
Hybrid, support and cooling	0.014
Others	0.010
Total	0.19
Before first measured point	0.032

Table 3.4: Contributions (expressed in fractions of a radiation length) to the material which are in the pseudorapidity range $2.0 < \eta < 5.5$.

The average value found of 18.9% is significantly larger than in the Technical Proposal. The main reasons for this are the increased thickness of the RF-shield, the increased thickness of the sensors and the increased number of stations. However, due to the reduced distance to the beam, and the optimized shape of the RF-shield which resulted in an average of

3.2% of an X_0 before the first measured point, the impact parameter resolution for charged hadrons has slightly improved compared to the TP. More details can be found elsewhere [16].

Preliminary investigations show that the relative increase in occupancy due to particles from secondary interactions in the VELO amounts to 5% in the inner and outer trackers [95] and 9% in RICH1 [96]. The effect on electron and photon reconstruction needs still to be studied. In parallel, a further optimization of the RF-shield is under study showing that its contribution inside the acceptance of the electromagnetic calorimeter ($\theta > 30$ mrad) can be reduced to below 5% of an X_0 in 90% of the azimuthal acceptance.

3.8 Alignment

The following alignment issues need to be considered:

- Alignment between an R- and ϕ -

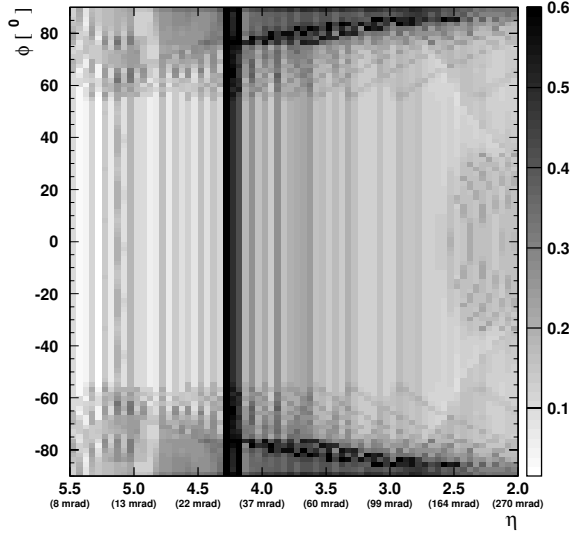


Figure 3.20: Distribution of the material traversed by particles at different η and ϕ . The number of X_0 traversed at the exit of the VELO tank is indicated by the scale on the right-hand side of the plot. The dark band at $\eta \approx 4.3$ is due to the 25 mrad conical section of the vacuum pipe.

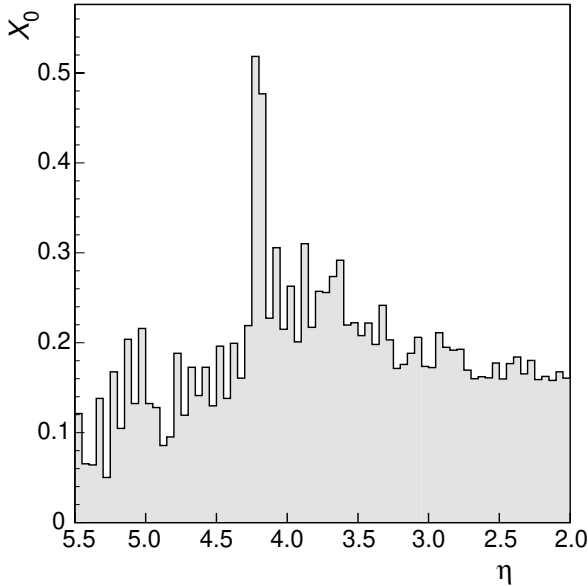


Figure 3.21: Distribution of the material traversed by particles at different η integrated over ϕ . The conical section of the vacuum pipe has been removed from the plot.

measuring sensor inside a module is obtained by construction with a precision of better than $5 \mu\text{m}$.

- Alignment between the sensors and the module base plate is achieved with a precision of better than $10 \mu\text{m}$ by using micrometer adjusters and a survey machine (see Table 2.7 and Fig. 3.7).
- The position of each module in a detector half will be measured by a survey machine and adjusted to the required precision of better than $20 \mu\text{m}$. However, the final alignment constants can only be determined under nominal running conditions, *i.e.* vacuum and low temperature, and therefore only with tracks from pp -interactions in the LHC machine. Both fully equipped VELO halves will be tested in a test-beam to cross check the survey measurements and to mimick as much as possible the LHC machine conditions. The feasibility of aligning the detector with tracks from pp -interactions has been demonstrated in our test-beam studies [37]. The existing algorithm still needs to be optimized for speed in order to deal with 100 sensors. However, comparing to other experiments [97], the VELO alignment, which has to deal with a relatively small number of individual sensors, is not anticipated to pose a particular problem.
- Alignment between the two detector halves: Since the detector halves have to be retracted before each filling of the LHC machine, the alignment between the two halves has to be re-calculated after each LHC fill. This requires only the determination of the relative position between the two detector halves, the modules in each detector half are not affected by the movement. Based on the overlap between the two VELO halves, a fast measurement is expected after the first pp -collisions.
- In addition, since the position of the

beam cannot be assured to be the same for consecutive fills, its position needs to be measured before moving the detectors to their final data-taking position. With about 100 minimum bias events, the distance to the silicon stations can be measured with $10\text{ }\mu\text{m}$ precision when the detectors are retracted by 3 cm from the beam [98].

- Alignment between the VELO and the downstream detectors: The VELO will be repositioned after each LHC filling operations with a precision of $50\text{ }\mu\text{m}$ which is more precise than what is needed to link the VELO tracks to the downstream detectors of LHCb.

- The VELO vacuum vessel will be baked-out in-situ to 150°C or more. A possible damage to the detector is not considered as a safety risk.
- Any accessible metallic piece will be properly grounded.
- An initial study of induced radioactivity in the VELO vacuum vessel showed that maintenance work during shutdowns is possible provided that proper precautions are taken [99].

The TIS commission concluded that no major safety problems were identified and possible safety hazards will be excluded by prototyping and testing the non standard equipment including a high safety factor.

3.9 Safety aspects

The Vertex Locator will comply with the safety policy at CERN (SAPOCO 42), and will follow the CERN safety rules and codes, the European and/or international construction codes which are relevant for the detector construction and operation. Possible specific risks, and actions, as discussed in the Initial Safety Discussion (ISD) with the Technical Inspection and Safety (TIS) Commission are summarized in the following.

- The two-phase CO_2 cooling system will run at a maximum pressure of 75 bar. The complete cooling circuit is designed and will be tested to sustain a pressure of up to 200 bar.
- The temperature of the detector will be monitored and in case of over temperature, the electrical power of the detector will be switched off automatically.
- Two powerful ion getter pumps will evacuate the VELO vacuum chamber. Only trained personnel will be allowed to manipulate this equipment⁹.

⁹ELECTRICAL SAFETY CODE C1.

4 Simulation results

4.1 Software and event samples

The performance of the VELO system has been studied using simulated data produced by the official LHCb simulation and reconstruction programs, SICBMC (v240) and SICBDST (v250) with database (v233). Proton-proton interactions at $\sqrt{s} = 14 \text{ TeV}$ were simulated using the PYTHIA (v6.1) event generator [100]. A multiple-interaction model was used, with varying impact parameter and running p_t cut-off, tuned [101] to reproduce existing low-energy data. The LHCb apparatus was simulated using GEANT3-based routines [94]. The response of the silicon detectors was based on a separate simulation, the results of which were verified with test-beam data [40].

The description of the VELO system in the simulation followed as closely as possible the design given in this report, including the RF-shield, the wake field guide, the cooling plates, the support frames and the parts of the vacuum vessel which are in the LHCb acceptance. Further details can be found in [4, 102].

The following benchmark channels were used to measure the performance of the VELO: minimum bias events, generic b-events and events containing $B_d^0 \rightarrow \pi^+ \pi^-$, $B_s^0 \rightarrow D_s^- \pi^+$ and $B_d^0 \rightarrow J/\psi K_s^0 (\mu\mu)$ decays. The events were generated assuming a luminosity of $2 \times 10^{32} \text{ cm}^{-2} \text{ s}^{-1}$. Each sample contained around 30k events. The B-decays were selected with the LHCb software package AXSEL [103] to restrict the sample to events which can be reconstructed offline and contribute to the physics analysis.

4.2 Optimization

4.2.1 Overall detector optimization

During the process of optimizing the detector layout, many different designs were studied. The performance of each individual design was judged by analyzing the benchmark channels. Taking into account other constraints, such as the necessary thickness of the RF-shield, the availability of thin silicon detectors and the finite number of electronics channels, we decided on the design described in this document. Further improvements, for example reducing the amount of material or using smaller strip pitches, may become possible in the future.

4.2.2 Impact on L1 trigger

The L1 trigger is based on tracks with a significant impact parameter. Tracks are reconstructed based on VELO measurements alone to minimize the amount of data which needs to be processed. As there is no magnetic field around the VELO, momentum information is in principle not available. Low momentum tracks can fake large impact parameters, i.e. signatures for tracks originating from B-decays, due to multiple scattering. In the algorithm employed for the L1 trigger as described in the TP this contribution of fake tracks was reduced by requiring track pairs to form secondary vertices. It was found that increasing the thickness of the RF-shield, from $100 \mu\text{m}$ to $250 \mu\text{m}$, reduces the efficiency of the L1 trigger in the $B_d^0 \rightarrow \pi^+ \pi^-$ channel by 15%. Replacing the corrugated RF-shield with a design which resembles a beam pipe close to the beam-line would reduce the L1 efficiency by almost 30%.

To monitor the development of the VELO

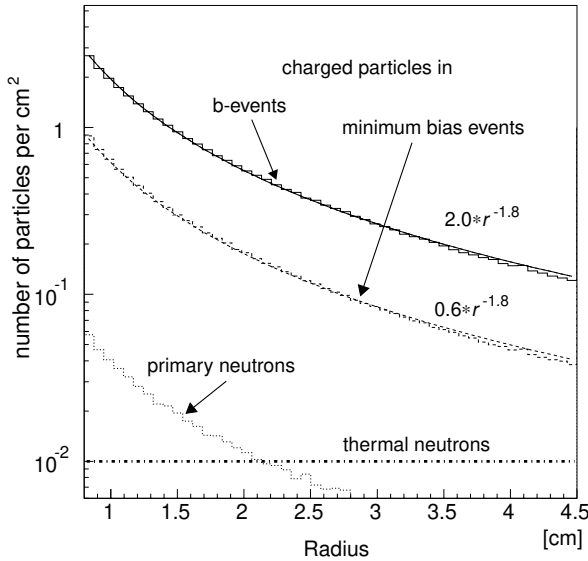


Figure 4.1: Average charged particles and neutron fluxes as function of radius, normalized to one pp -interaction.

since the TP, a simpler algorithm was used to simulate the L1 trigger, to avoid having to re-tune the algorithm for every VELO design, as is described in detail in Ref. [4, 102]. The designs were compared based on the number of tracks with a large impact parameter ($> 50 \mu\text{m}$ and $> 100 \mu\text{m}$). It has been shown that the realistic design with $250 \mu\text{m}$ of RF-shield and $300 \mu\text{m}$ of sensor thickness is expected to give a comparable performance as the TP design but with the $250 \mu\text{m}$ RF-shield. The L1 trigger is currently being retuned and will integrate additional information from L0 [104]. It is expected that its performance will be improved relative to the TP results.

4.3 Particle fluxes

The particle flux on the surface of the silicon is dominated by particles from the primary interaction [105]. Fig. 4.1 shows the average distribution of charged particles per cm^2 as function of their radial position (r) on the silicon surface for minimum bias and generic b-events coming from one pp -interaction. These distributions are well described with the function $N \times r^\alpha$. Typical val-

ues are $0.6 \text{ particles/cm}^2 \times (r/\text{cm})^{-1.8}$ for minimum bias and $2.0 \text{ particles/cm}^2 \times (r/\text{cm})^{-1.8}$ for b-events. The distributions vary slightly from station to station, with the highest density of particles at the innermost radius and the steepest drop as function of radius for the stations around the nominal interaction point.

To determine the radiation damage to silicon, one also needs to consider the flux of neutrons. It was shown in a detailed study [105], taking into account the material around the VELO, that thermal neutrons have no radial dependence and dominate over the neutrons from the primary interaction beyond a radius of about 2 cm. However, both contributions are negligible compared to the charged particle flux (Fig. 4.1).

Based on a total cross-section of 102.4 mb, a luminosity of $2 \times 10^{32} \text{ cm}^{-2} \text{ s}^{-1}$ and 10^7 s of operation per year, one expects about 2×10^{14} interactions per year. The charged particle flux (pions, protons, kaons) and the neutron flux was normalized to the equivalent damage in silicon from neutrons of 1 MeV kinetic energy (n_{eq}) by using the tables of Ref. [106]. Lacking information about kaons, we used the damage factors of pions. The values which were used are shown in Fig. 4.2 as function of the kinetic energy for the different particles. For kinetic energies where no damage factor was available, the value closest to that energy was used. In the Monte Carlo simulation, the tracking of particles was stopped at kinetic energies below 10 MeV. A small test run was made with the threshold reduced to 1 MeV which gave no significant difference in the results.

The yearly dose at $r = 0.8 \text{ cm}$ is found to be equivalent to $(0.5 - 1.3) \times 10^{14} n_{\text{eq}}/\text{cm}^2$ depending on the position in z (Fig. 1.2). The high radiation damage in the stations close to the nominal interaction point is due to the much lower average energy of particles crossing the stations in this region (Fig. 4.2). By swapping stations according to their received dose, it is possible to achieve an average dose of about $0.9 \times 10^{14} n_{\text{eq}}/\text{cm}^2$ at $r = 0.8 \text{ cm}$ for all stations.

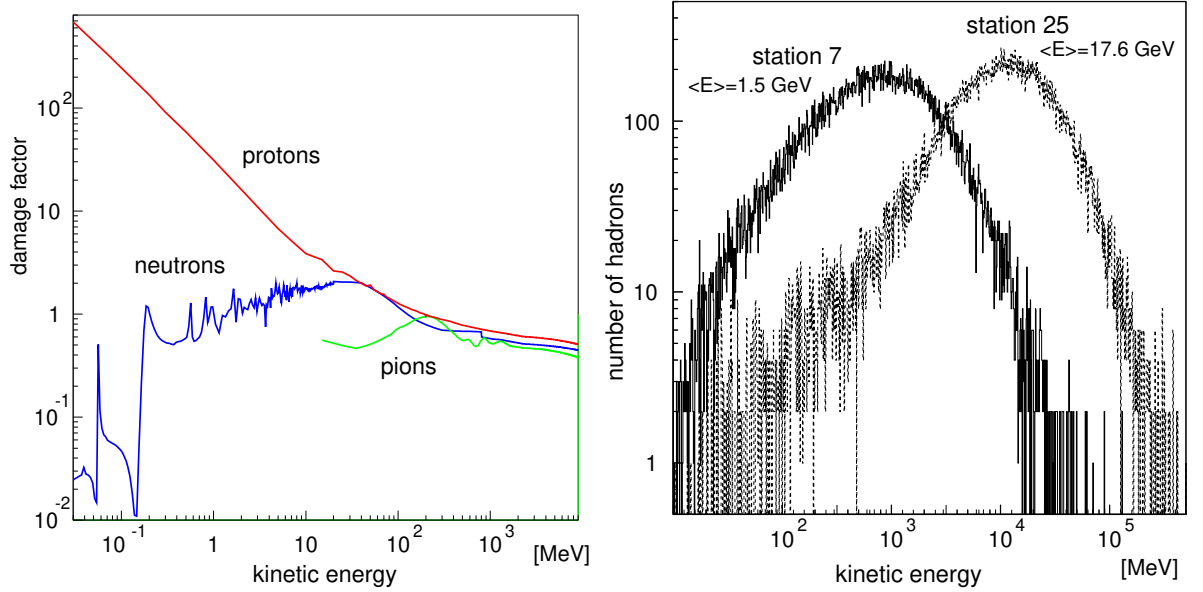


Figure 4.2: Damage factors for different particle types as function of their kinetic energy based on the tables of Vasilescu and Lindstroem [106]. Also shown is the kinetic energy distribution of all hadrons at two different station positions.

4.4 Physics performance

4.4.1 Impact parameter resolution

The impact parameter resolution of the VELO is of great importance for the performance of the L1 trigger, which searches for tracks with large impact parameter with respect to the primary vertex. It is determined by the intrinsic resolution of the sensors and by the amount of Coulomb multiple scattering in the RF foil as well as in the silicon.

A simple model can be used to understand qualitatively the distribution (Fig. 4.3) obtained from Monte Carlo simulations. Taking into account only the measurements of two R-sensors with resolutions σ_1 and σ_2 at distances to the interaction point of Δ_{01} and Δ_{02} , the error on the impact parameter for forward pointing tracks can be written to first order as:

$$\sigma_{\text{IP}}^2 = \frac{r_1^2}{p_t^2 \sqrt{2}} \left\{ 13.6 \text{ MeV}/c \cdot \sqrt{x/X_0} [1 + 0.038 \ln(x/X_0)] \right\}^2 + \frac{\Delta_{02}^2 \sigma_1^2 + \Delta_{01}^2 \sigma_2^2}{\Delta_{12}^2} \quad (4.1)$$

with $\Delta_{12} = \Delta_{02} - \Delta_{01}$ and p_t the transverse momentum. The total amount of material traversed between the interaction point and the second R-sensor is approximated by a radiation length x/X_0 at the position of the first sensor (r_1).

There are two consequences. The first is a natural choice for the sensor strip pitch as a function of radius for the R-sensors. If we require an equal contribution from two measured R-coordinates to the error on the impact parameter then, to a good approximation, $\frac{\Delta_{01}}{\Delta_{02}} = \frac{r_2}{r_1}$. Therefore $\sigma_2 = \sigma_1 \cdot \frac{r_2}{r_1}$, which suggests a design with the strip pitch increasing linearly with the radius (see section 3.1). The second is, that for minimizing the error due to multiple scattering, one should have the first measured point as close as possible to the primary vertex.

The average radius, $\langle r_1 \rangle$, of the first measured point on a track is about 1 cm and the average extrapolation factor, $\langle \Delta_{02}/\Delta_{12} \rangle$ is about 1.8. Fitting the distribution obtained from the Monte Carlo simulation (Fig. 4.3) with Eq. 4.1 yields a multiple scattering term corresponding to about 5% of a radiation

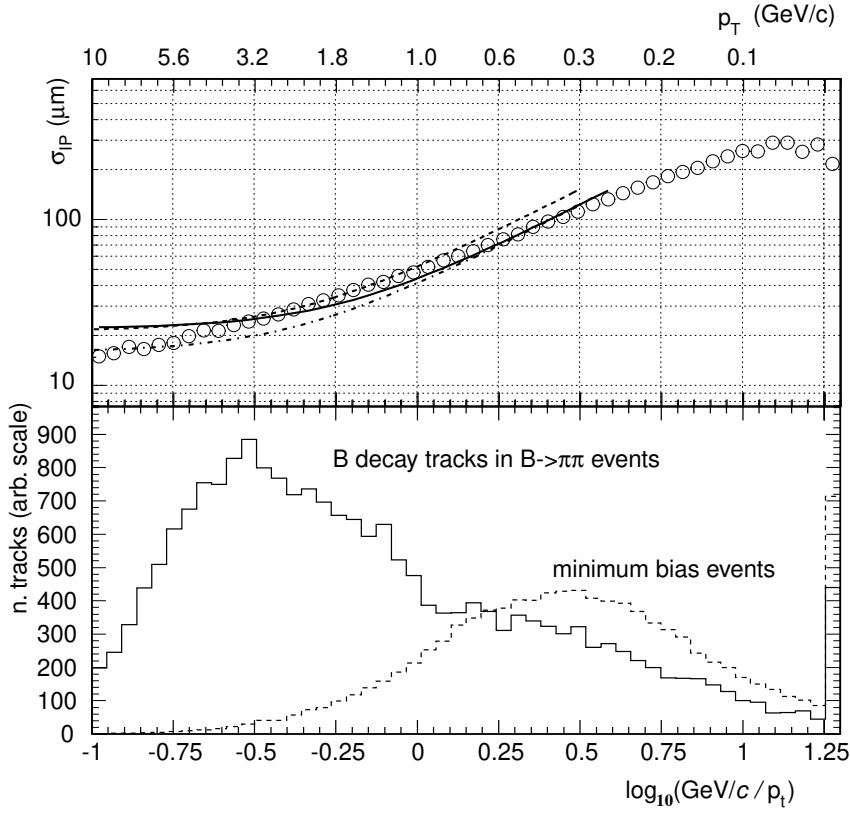


Figure 4.3: The upper plot shows the error on the impact parameter as a function of $\log_{10} 1/p_t$ (p_t in GeV/c). The solid curve is the result of a fit using Eq. 4.1 and corresponds to a multiple scattering term of about 5% of an X_0 and an average resolution of $8 \mu\text{m}$. The dashed and dotted curves are obtained by increasing the multiple scattering contribution by 50% (dashed curve) and by reducing the resolution term by 50% (dotted curve). The lower plot shows the p_t distribution for all tracks from B decays in events where one B decayed into $\pi^+\pi^-$ and for tracks from minimum bias events which passed the L0 trigger.

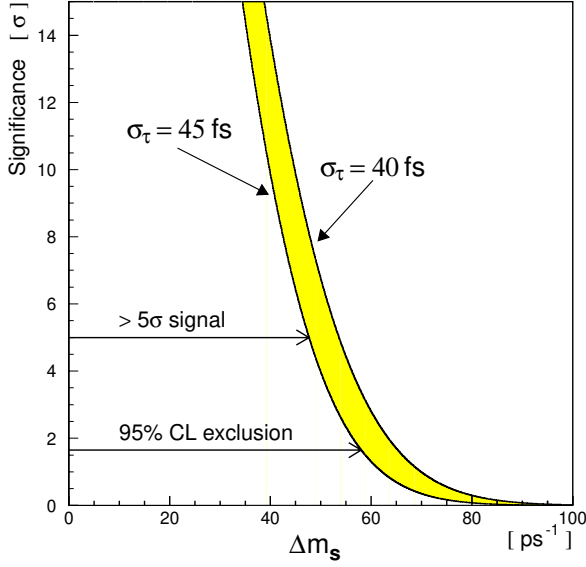


Figure 4.4: The one year sensitivity to Δm_s for proper time resolutions between 40 and 45 fs.

length and an average measurement error of $8 \mu\text{m}$. These numbers agree reasonably well with the expectations (Table 2.4 and Table 3.4).

Two regions of p_t can be distinguished in Fig. 4.3:

- Large p_t : These tracks are typically tracks from b-decays. Here the cluster resolution dominates over multiple scattering. Choosing a small strip pitch is advantageous.
- Small p_t : Multiple scattering dominates the error of the impact parameter. These are the tracks which limit the performance of the L1 trigger, since momentum information is not available at this early trigger level.

4.4.2 Primary vertex, decay length and time resolutions

The error on the primary vertex is dominated by the number of tracks produced in the pp -collision. For an average B-event, the resolution in the z -direction is $42 \mu\text{m}$ and $10 \mu\text{m}$ perpendicular to the beam. The precision on the

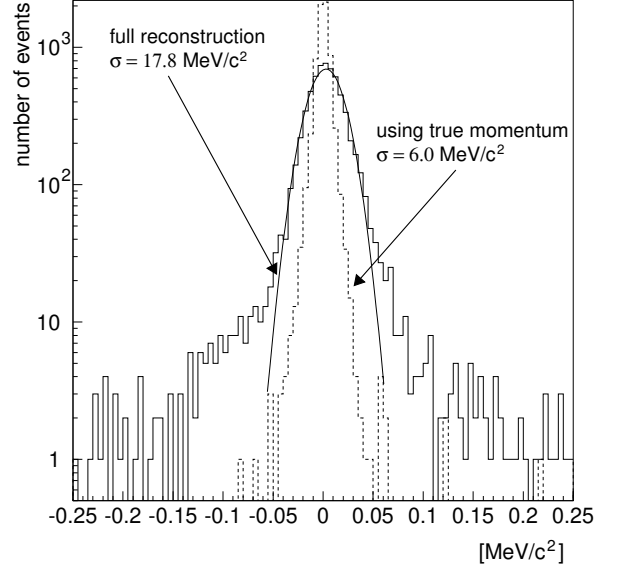


Figure 4.5: Invariant mass of the two pions from the $B_d^0 \rightarrow \pi^+\pi^-$ decay. The deviation from the nominal B^0 -mass is shown. The dotted line shows the distribution obtained by using the true particle momentum and the angle between the two pions as measured in the VELO.

decay length ranges from $220 \mu\text{m}$ to $375 \mu\text{m}$ depending on the decay channel (Table 4.1 and Ref. [4, 102]). The decay length residuals have tails, due to small momenta and thus large multiple scattering contributions, which cannot be fitted with a single Gaussian.

The proper time resolution of the $B_s^0 \rightarrow D_s^- \pi^+$ channel was found to be $\sigma_\tau = 40 \text{ fs}$. It is dominated by the error of the decay length measurement. The error of the time dilation due to the momentum uncertainty is less than 8 fs.

The proper time resolution can be related to σ , the statistical significance of measuring Δm_s [107], using the relation:

$$\sigma \approx \sqrt{N_{\text{tag}}/2} f_{B_s^0} (1 - 2\omega_{\text{tag}}) e^{-(\Delta m_s \sigma_\tau)^2/2}, \quad (4.2)$$

where N_{tag} is the number of tagged B_s^0 events, $f_{B_s^0}$ is the purity of the sample and ω_{tag} is the mis-tag rate of the B_s^0 production flavour. With the proper time resolution of $\sigma_\tau = 40 \text{ fs}$ and the values of N_{tag} , $f_{B_s^0}$ and ω_{tag} reported in [108], Eq. 4.2 leads to the expectation that a 5σ measurement of Δm_s will be possible for val-

event type	σ_1 [μm]	σ_2 [μm]	N_2/N_1	σ_{av} [μm]
$B_d^0 \rightarrow \pi^+ \pi^- [102]$	115 ± 4	358 ± 20	0.40 ± 0.06	224 ± 22
$B_s^0 \rightarrow D_s^- \pi^+ [102]$	153 ± 6	477 ± 27	0.47 ± 0.06	310 ± 30
$B_d^0 \rightarrow J/\psi K_s^0 (\mu\mu) [4]$	159 ± 9	581 ± 55	0.51 ± 0.11	373 ± 66

Table 4.1: Resolutions for decay lengths of different bench mark channels. σ_1 and σ_2 are the widths of a double Gaussian fit to the decay length distribution and N_2/N_1 the ratio of the Gaussian fit normalization, which takes into account the tail contributions. σ_{av} is an average resolution.

decay mode	σ [MeV/c^2]	σ [MeV/c^2]
$B_d^0 \rightarrow \pi^+ \pi^-$	17.8 ± 0.2	6.1 ± 0.1
$B_s^0 \rightarrow D_s^- \pi^+$	12.0 ± 0.2	9.1 ± 0.2
$D_s^- \rightarrow K^+ K^- \pi^-$	5.4 ± 0.1	4.2 ± 0.1

Table 4.2: Invariant mass resolutions for different decay modes. The numbers in the third column list the contribution of the VELO angle measurements only.

ues up to 54 ps^{-1} after one year of data-taking (Fig. 4.4).

4.4.3 Invariant mass resolutions

Invariant mass resolutions for B- and D-mesons are listed in Table 4.2. Fig.4.5 shows as an example the invariant mass distribution of the two pions from the $B_d^0 \rightarrow \pi^+ \pi^-$ decay. For an estimation of the contribution of the VELO angle measurements to the invariant mass resolution, the reconstructed momentum of a particle has been replaced by its true momentum. In the decay $B_d^0 \rightarrow \pi^+ \pi^-$, the invariant mass resolution of $17.8 \text{ MeV}/c^2$ is dominated by the momentum measurement. The VELO angle measurement accounts only for $6 \text{ MeV}/c^2$. For the decays $B_s^0 \rightarrow D_s^- \pi^+$ and $D_s^- \rightarrow K^+ K^- \pi^-$, the VELO angle measurements and the momentum measurements have equal weight.

5 Project organization

5.1 Schedule

The overall work programme and schedule is summarized in Fig. 5.1. It covers the period up to spring 2006, when the first LHC pilot run is expected. The schedule is planned to ensure that the VELO is installed and operational before the beam starts. The period of single beam in LHC is used for commissioning the VELO in situ.

5.1.1 Completion of design and prototyping

A realistic design of the VELO was described in the previous chapter. Several of the tasks in the schedule require the evaluation of final prototypes before the production can start.

1. Silicon: Sensors from different vendors need to be characterized. Some improvements can be achieved with additional R&D, e.g. ultimate ϕ -sensor design with floating strips and thin n -on- n sensors. The prototyping of sensors will be completed by a design review in the summer of 2002.
2. Front-end chip: The final version of the SCTA-VELO chip and a full working Beetle chip are expected to arrive before the summer of 2001. Characterization of the two chips before and after irradiation will be done before the end of 2001. A review of the two chip options will take place in the beginning of 2002 and will lead to a decision which chip to use for the first VELO sensors.
3. Readout electronics: Prototypes of the 16-chip hybrid, repeater electronics and

the L1 readout board will be produced and tested during 2001. The analog link over 60 m twisted pair cables will be tested in a large scale system before the end of 2001.

4. Mechanics & Vacuum: The VELO underwent a conceptual design review [109] in April 2001. Further prototyping is needed to characterize several components of the design. A production readiness review is foreseen for February 2002.
5. Alignment, monitoring and control: different options are proposed to fulfill the various tasks in this category, and prototyping and testing will continue during the next test-beam runs.

5.1.2 Construction

The major construction tasks include:

1. Vacuum vessel: The whole system will be manufactured at NIKHEF, including the secondary/primary vacuum system, the detector mounting system and the cooling system except of the thin exit window (LHC-VAC group). The progress will be reviewed on a yearly basis together with the LHC machine groups involved. Completion is foreseen during 2004.
2. Sensors: From past experience, about half a year is needed to produce the sensors. The production of the front-end chips and the hybrids can partially proceed in parallel. The construction of one complete detector module is expected to take about one week. This includes the

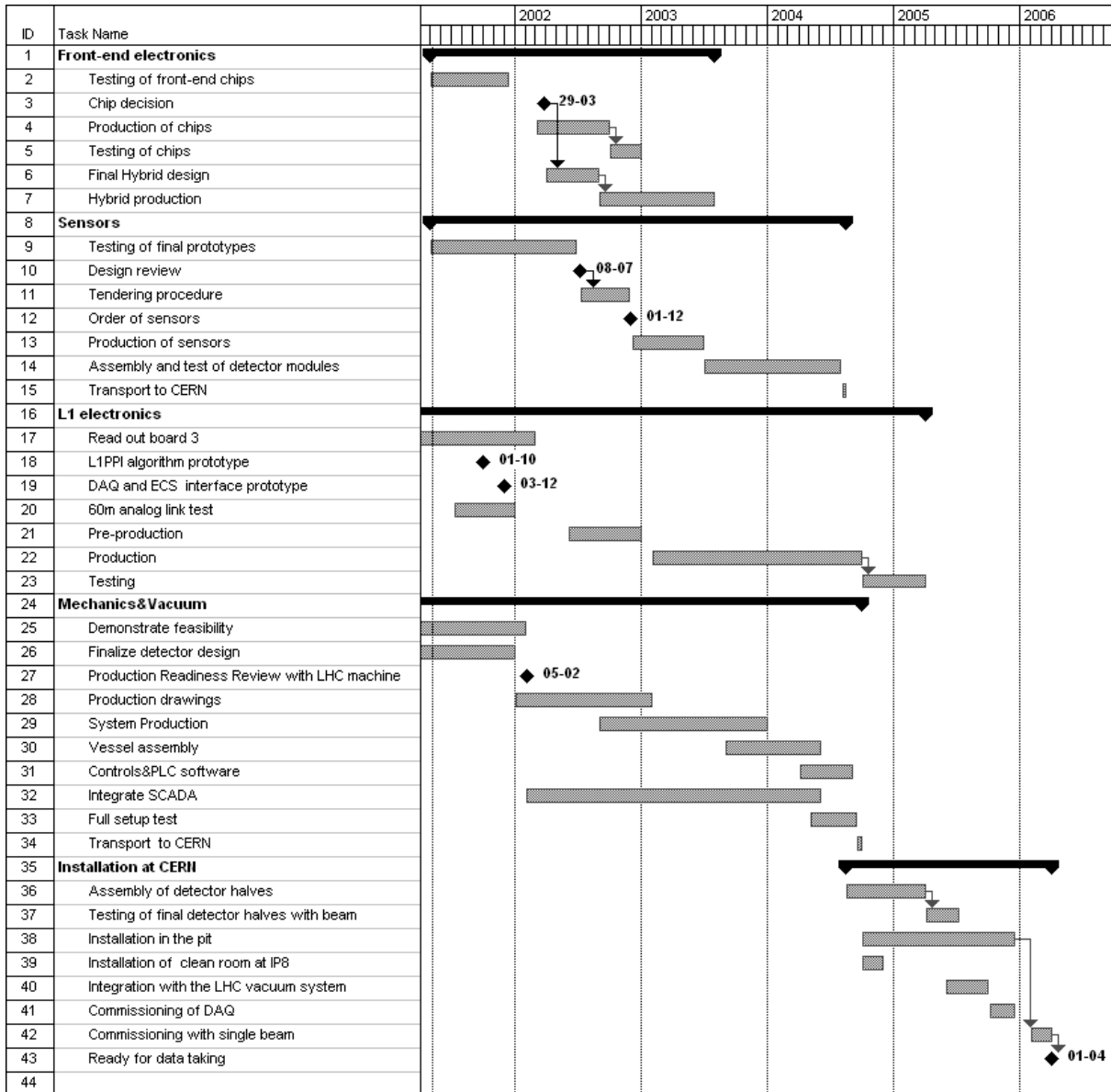


Figure 5.1: Schedule of the VELO project, up to the first physics run of LHCb in spring 2006

precise alignment of the sensors inside a module. Several modules can be built in parallel.

3. Readout electronics: the front-end chip production is scheduled for the summer of 2002, in order to have the chips ready and tested for the module construction. Production of the readout electronics chain (from vacuum vessel pin-out to DAQ) is scheduled to be completed by the end of 2004. These involve common LHC developments (TTC chipset) and the ECS interface. The L1 electronics make maximum use of FPGAs to implement specific functionality. The modules are situated in the counting room and are not exposed to a high radiation dose.

4. Testing: systematic tests and certification of the silicon sensors and readout electronics will be a time-consuming task and must follow the production process.

It is planned to test the two detector halves in a charged particle beam during the first half of 2005.

5.1.3 Installation and commissioning

Installation of the VELO vessel can start after the LHC octant test in September 2004. A clean area at the interaction point needs to be set-up to minimize the pollution of pieces which will be placed inside the primary or secondary vacuum. The vacuum vessel will be connected to the LHC vacuum control system by autumn 2005.

The L1 electronics installation will start at the begin of 2005. The system will be ready to start commissioning of the DAQ with the other LHCb sub-detectors in October 2005. Five months of operation in this mode are foreseen to ensure that the VELO is ready to take data at nominal LHCb luminosity by April 2006. Valuable initial measurements concerning the RF shielding can be done during the LHC single beam operation before the first pilot run with collisions.

Cables	Number	Space (cm ²)
6400 analog links: twisted pair ND36P	400	960
ECS: Cat5	1	0.25
TTC: optical link	4	0.4
HV power cables	100	25
LV power cables	225	225
Pipes		
CO ₂ cooling	2	10

Table 5.1: List of different cables and space needed in the shielding wall.

The logistics of the VELO is situated at the following positions:

- The vacuum pumps are directly mounted onto the vacuum vessel.
- The ECS transceiver boards are located close to the VELO at a distance of about 12 m.
- The L1 electronics and all the power supplies are situated behind the shielding wall. At the same place, about 2 m² of space are needed for the compressor and the pump units of the CO₂-cooling system. The space needed for cables in the shielding wall is summarized in Table 5.1. If a packing of 60% is assumed, then the total space needed amounts to 0.2 m².

5.2 Milestones

Key milestones for the VELO project are listed in Table 5.2.

5.3 Costs

The total cost for the VELO is estimated to be 4850 kCHF. The details are summarized in Table 5.3. Where appropriate, spares have been included. Most of the estimates are based on quotes from industry or recent purchases of similar items (e.g. prototype detectors, feedthroughs).

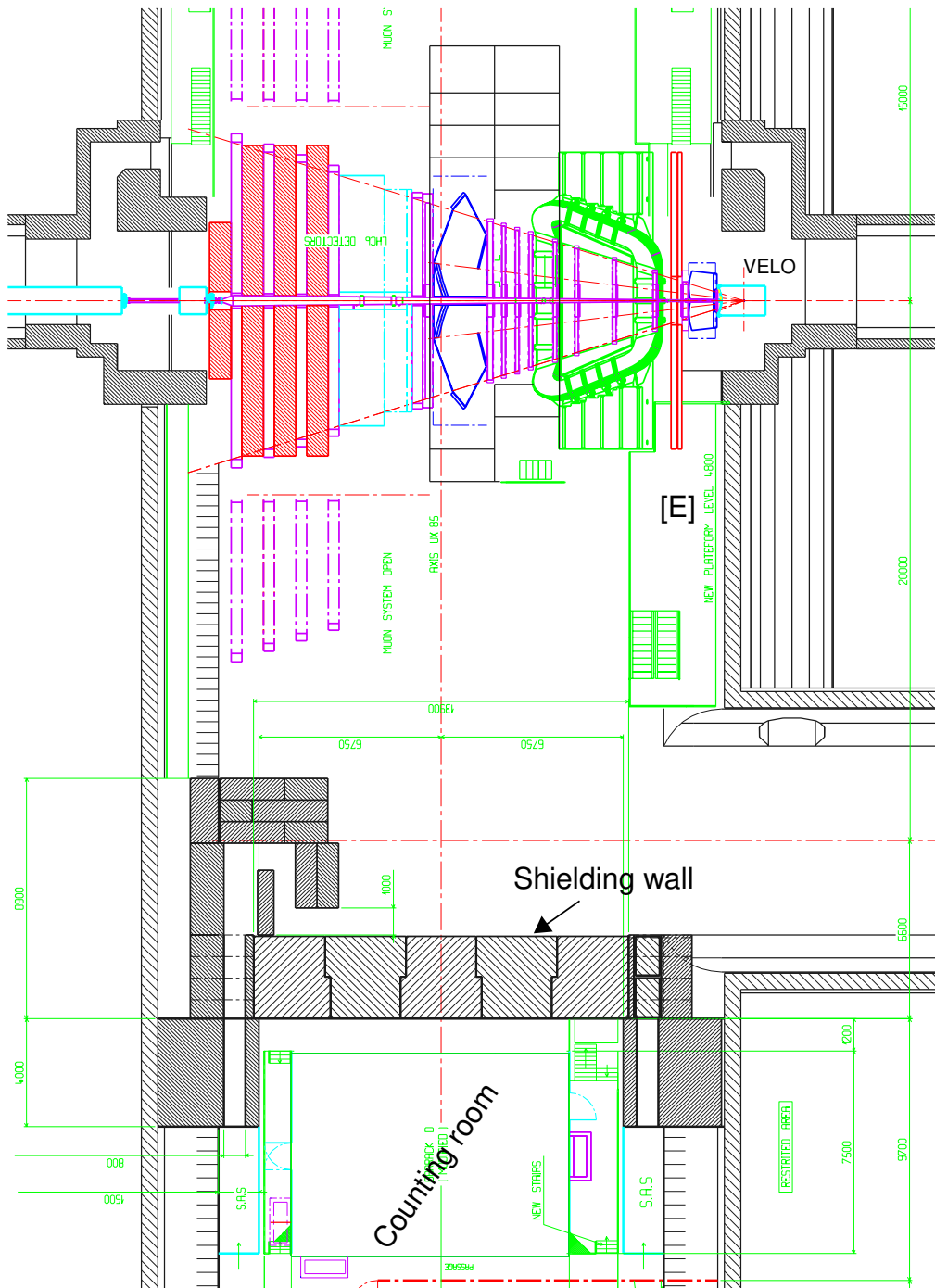


Figure 5.2: Top view of the LHCb cavern showing the LHCb experiment and the counting room. Most of the VELO logistics is located behind the shielding wall in the counting rooms, except of the ECS slave boards which are at about 12 m distance from the VELO [E].

Date	Milestone
2002/July	Silicon Tests of prototypes completed
2002/December	design review and start of tendering
2003/June	Place final order
2004/September	Sensor production finished
2005/April	Module production finished
	Test of detector halves in beam
2001/December	Front-end chip Characterization of chips completed
2002/March	Front-end chip decision
2002/December	Production/testing completed
2001/September	L1 electronics Read-out board 3 prototype
2001/December	Analog links tested on large scale
2002/March	Final prototype of digitizer board
2003/March	L1 electronics production starts
2005/March	Production/testing completed
2002/February	Mechanics/Vacuum Production readiness review with LHC groups
2003/March	All production drawings finished
2004/June	Production/testing completed
2004/December	Installation Start installation in IP 8
2005/October	Commissioning of DAQ with other sub-detectors
2005/December	Installation completed

Table 5.2: VELO project milestones.

Item	Number of units	sub-total (kCHF)
Mechanics& Vacuum:		1407
Vacuum Vessel	1	
Vacuum equipment		
Cooling system		
Patch panels	4	
Feedthrough flanges ¹	28	
Secondary vacuum container	2	
Wake field suppressors		
Ti evaporators		
Positioning mechanism		
Cables and connectors		
Monitoring and control		
Silicon detectors:		635
Sensors	125	
Hybrid	125	
Electronics:		2780
Frontend chips	1600	
Digitizer boards including analog data links	100	
TTC & ECS interface	100	
Data links to Readout Unit	100	
Readout Units	25	
Data links to L1 trigger	100	
Readout Units for L1 trigger	20	
LV1 interface	100	
DAQ interface	100	
Crates	5	
High voltage power supplies	100	
Low voltage power supplies	100	
TOTAL		4822

Table 5.3: VELO project costs (kCHF). ¹includes feed-throughs for pile-up VET0.

5.4 Division of responsibilities

Institutes currently working on the LHCb VELO project are: CERN, NIKHEF and the Universities of Heidelberg, Lausanne and Liverpool.

The sharing of responsibilities for the main VELO project tasks is listed in Table 5.4. It is not exhaustive, nor exclusive. For example, the exact sharing of responsibilities for the software will be discussed in the summer of 2001. However, it is understood that the VELO group will be responsible and will have the resources to provide all VELO specific software, for DAQ, monitoring and reconstruction.

Task	Institutes
Mechanics & Vacuum:	
Vacuum vessel	NIKHEF
Exit window	CERN LHC-VAC
Vacuum system	NIKHEF
RF foil and wake field suppressors	NIKHEF
CO ₂ cooling system	NIKHEF
Detector support frame and positioning system	NIKHEF
Detector modules:	
Silicon sensors	Liverpool
Hybrid	Liverpool
Support and cooling	Liverpool, NIKHEF
Front-end chip	Heidelberg
Read-out Electronics:	
Repeater electronics and analog links	Lausanne
Digitizer boards	Lausanne
L1 trigger interface	Lausanne
Monitoring, Control, Alignment:	
Vacuum, Cooling	NIKHEF
ECS interface of L0 electronics	Heidelberg
ECS interface of L1 electronics	Lausanne
Alignment issues	CERN, Liverpool, NIKHEF
Detector design and optimization	CERN, Liverpool, NIKHEF
Test-beam	CERN
Quality control	all
Final assembly and system tests	all

Table 5.4: VELO project: Sharing of responsibilities.

References

- [1] LHCb Technical Proposal, CERN/LHCC 98-4.
- [2] LHCb Magnet Technical Design Report, CERN/LHCC 2000-7; LHCb Calorimeters Technical Design Report, CERN/LHCC 2000-0036; LHCb RICH Technical Design Report, CERN/LHCC 2000-0037; LHCb Muon System Technical Design Report, CERN/LHCC 2001-011.
- [3] *Study of the LHCb pile-up trigger and the $B_s \rightarrow J/\psi\phi$ decay*, N. Zaitsev, PhD. Thesis, University of Amsterdam, 27 October 2000.
- [4] *VELO Geometry Optimization*, T. Bowcock *et al.*, LHCb 2000-090.
- [5] *Requirements for the L0 front-end electronics*, J. Christiansen, LHCb-99-029.
- [6] *Comparison of analogue and binary read-out in the silicon strips vertex detector of LHCb*, P. Koppenburg, LHCb-97-020.
- [7] *The CO₂ cooling system for the LHCb vertex detector*, H. Boer Rookhuizen *et al.*, LHCb-note, to be published.
- [8] *Mechanical Design of LHCb Vertex Locator*, LHCb 2001-083.
- [9] C. Benvenuti *et al.*, Vacuum **53** (1999) 219-225.
- [10] *Conceptual design of the LHCb VELO vacuum system*, J.F.J. van den Brand *et al.*, LHCb 2001-080.
- [11] *A first study of wake fields in the LHCb vertex detector*, N. van Bakel *et al.*, LHCb 99-041.
- [12] *Wake fields in the LHCb vertex detector: strip shielding*, N. van Bakel *et al.*, LHCb 99-043.
- [13] *Wake fields in the LHCb vertex detector: alternative designs for the wake field suppressor*, N. van Bakel *et al.*, LHCb 99-044.
- [14] *Numerical calculation of the VELO coupling impedance*, N. van Bakel *et al.*, LHCb 2001-082.
- [15] *Preliminary Risk Analysis for the LHCb Vertex Detector*, J.F.J. van den Brand *et al.*, LHCb 2001-079.
- [16] *Material Distribution in the VELO*, J. Libby, T. Ruf, M. McCubbin, LHCb-2001-019.
- [17] *Simulation of the vertex trigger preprocessor: effects of noise on L1 performance*, P. Koppenburg, LHCb-99-003.
- [18] *Overview of silicon detectors*, H. Dijkstra, <http://lhcb-doc.web.cern.ch/lhcb-doc/presentations/conferencetalks/2001.htm>
- [19] *Charge collection efficiency and resolution of an irradiated double-sided silicon microstrip detector operated at cryogenic temperatures*, K. Borer *et al.*, Nucl. Instr. and Meth. **A440** (2000) 17.
- [20] *Simulation of charge collection and sharing in microstrip detectors*, T.J. Brodbeck, A. Chilingarov, Nucl. Instr. and Meth. **A395** (1997) 29; *Charge collection efficiency in heavily irradiated silicon diodes*, L. Beattie *et al.*, Nucl. Instr. and Meth. **A412** (1998) 238.
- [21] *Micro-discharge noise and radiation damage of silicon microstrip sensors*, T. Ohsugi *et al.*, Nucl. Instr. and Meth. **A383** (1996) 166.
- [22] *A comparison of the performance of irradiated p-in-n and n-in-n silicon microstrip detectors read out with fast binary electronics*, P.P. Allport *et al.*, Nucl. Instr. and Meth. **A450** (2000) 297.
- [23] *Design optimization of radiation-hard, double-sided, double-metal, AC-coupled silicon sensors*, T. Ohsugi *et al.*, Nucl. Instr. and Meth. **A436** (1999) 272.
- [24] R.H. Richter *et al.*, Nucl. Instr. and Meth. **A377** (1996) 412;

- IEEE Trans. Nucl. Sci., vol. 47, n. 4, August 2000.
- [25] *ROSE Contribution to the LEB Workshop*, M. Moll:
<http://rd48.web.cern.ch/RD48/6th-workshop/6th-workshop.htm>
- [26] *Improving the radiation hardness properties of silicon detectors using oxygenated n-type and p-type silicon*, G. Casse, P.P. Allport and M. Hanlon, IEEE Trans. Nucl. Sci., vol. 47, no. 3, June 2000;
A comparative study of oxygenated and non-oxygenated Si pad diodes, miniaturation and large area microstrip detectors, G. Casse *et al.*, presented at the 4th International Symposium on Development and Application of Semiconductor Tracking Detectors, Hiroshima, March 22-25 2000, to be published in Nuclear Instruments and Methods in Physics Research.
- [27] *Charge collection efficiency of irradiated silicon detectors operated at cryogenic temperatures*, K. Borer *et al.*, Nucl. Instr. and Meth. **A440** (2000) 5.
- [28] *Operating conditions of the VELO silicon*, T. Bowcock, LHCb 2001-069.
- [29] *Detector Geometry - Vertex Locator test-beam software description*, C. Parkes, LHCb-2000-096
- [30] *A VLSI chip produced by Integrated Detectors and Electronics AS (IDE AS)*, Gaustadalleen 21, N-0371, Oslo, Norway; *VIKING, a CMOS low noise monolithic 128 channel frontend for Si-strip detector readout*, O. Toker *et al.*, Nucl. Instr. and Meth. **A340** (1994) 572.
- [31] *SCTA - a Rad-Hard BiCMOS Analogue Readout ASIC for the ATLAS Semiconductor Tracker*, F. Anghinolfi *et al.*, IEEE Trans. Nucl. Science Vol.44, No.3, June 1997.
- [32] *Noise Evaluation and Improvement of the LAL-RAL Microplex Readout Chip for the DELPHI Vertex Detector*, P. Seller *et al.*, Nucl. Instr. and Meth. **A348** (1994) 444.
- [33] *Study of vertex silicon detectors for LHC experiments*, Thesis, S. Saladino, (CERN-OPEN-99-374), 3 December 1999.
- [34] *Track Fit - Vertex Locator Test-Beam Software Description*, C. Parkes, LHCb 2001-038.
- [35] *Results on the DELPHI microvertex alignment from a precise 3-D mapping*, A. Andreazza *et al.*, Nucl. Instr. and Meth. **A312** (1992) 431.
- [36] MINUIT reference manual, CERN Program Library Long Writeup Y250.
- [37] *Alignment of the 1998 VELO Test Beam Data*, I. Tomalin, LHCb 99-032.
- [38] *The L1 vertex trigger algorithm and its performance*, H. Dijkstra, T. Ruf, LHCb 98-006.
- [39] *Study of the Vertex Trigger Performance on Test-Beam Data*, F. Teubert, LHCb 99-030.
- [40] *VELO Telescope Resolution and Efficiency Measurements*, P. Bartalini *et al.*, LHCb 2000-099
- [41] *Study of Resolution of VELO Test-Beam Telescope*, V. Wright *et al.*, LHCb 2000-103.
- [42] *Measurement of the Irradiation Profile at the PS Beam*, J. Libby, T. Ruf, F. Teubert and G. Casse, LHCb 2001-020.
- [43] *Performance of an irradiated n-on-n Hamamatsu prototype VELO detector*, T. Bowcock *et al.*, LHCb 2001-039.
- [44] *Performance of an irradiated p-on-n Micron prototype VELO detector*, T. Bowcock *et al.*, LHCb 2001-040.
- [45] *Characterisation of an inhomogeneously irradiated microstrip detector using a fine spot infrared laser*, G. Casse *et al.*, LHCb 2001-053.

- [46] *LHCb VELO Module Design*, T. Bowcock, J. Carrol and A. Muir, LHCb 2001-068.
- [47] *Simulation and Measurements of the thermal performance of a LHCb VELO prototype module*, T. Bowcock, J. Carrol and P. Sutcliffe, LHCb 2001-070.
- [48] *HELIX 128 - An Amplifier and Read-out Chip for MSGCs and Silicon Microstrip Detectors*, M. Feuerstack *et al.*, HD-ASIC-18-0696;
HELIX - A Readout Chip for the HERA-B Microstrip Detectors 2nd Workshop on Electronics for LHC Experiments, W. Fallot-Burghardt *et al.*, Balatonfüred, Hungary, 1996.
- [49] *Results of the Industrial Transfer of DMILL, a Rad-Hard Mixed Analog-Digital Technology for High-Energy-Physics Applications*, M. Dentan *et al.*, Proceedings of the 3rd Workshop on Electronics for LHC Experiments, CERN/LHCC/97-60.
- [50] R. Brenner *et al.*, Nucl. Instr. and Meth. **A339** (1994) 564.
- [51] 3rd RD49 Status Report, *Study of Radiation Tolerance of ICs for LHC*, CERN/LHCC/2000-003 (2000).
G. Anelli *et al.*, *Total Dose Behavior of Submicron and Deep-Submicron CMOS Technologies*, Proceedings of the 3rd Workshop on Electronics for LHC Experiments, CERN/LHCC/97-60.
- [52] *Total Dose and Single Event Effects (SEE) in a 0.25 μm CMOS Technology*, F. Faccio *et al.*, CERN/LHCC/98-36 (1998).
- [53] *The performance of the SCTA ASIC when reading out irradiated and non-irradiated VELO prototype detectors*, M. Charles, J. Buytaert and J. Libby, LHCb 2001-041.
- [54] *The SCTA-VELO Reference Manual*, J. Buytaert, LHCb 2001-045.
- [55] *Characterization of the Beetle-1.0 Front End Chip*, D. Baumeister *et al.*, LHCb 2001-049.
- [56] *Investigation of Characteristics and Radiation Hardness of the BeetleCO10 Chip*, N. van Bakel *et al.*, LHCb 2001-037.
- [57] *Vertex Detector Electronics: ODE Pre-Prototype, User Manual Version 2.0*, Y. Ermoline, IPHE note VELO 2000-008, LHCb 2001-057.
- [58] *TTCrx Reference Manual*, V3.2, February 2001, http://www.cern.ch/TTC/TTCrx_manual3.2.pdf.
- [59] *Analog Device AD9059*, <http://www.analog.com/pdf/ad9059.pdf>.
- [60] Access Port and Boundary-Scan Architecture (IEEE Std 1149.1) <http://www.analog.com/pdf/ad9059.pdf>.
- [61] *LHCb VELO Off Detector Electronics Preprocessor and Interface to the Level 1 Trigger*, A. Bay, G. Haefeli, P. Koppenburg, LHCb 2001-043, IPHE 2000-019.
- [62] *Test of VELO detector FE chips using the ODE-PP*, Y. Ermoline, G. Gagliardi, U. Parzefall, LHCb 2001-067, IPHE 2001-006.
- [63] [http://caenlab.caen.it/Catalogo.nsf/\(AllDoc\)/V550V550A](http://caenlab.caen.it/Catalogo.nsf/(AllDoc)/V550V550A).
- [64] *Vertex Detector Electronics: RB3 Specification Draft 4*, Y. Ermoline, LHCb 2001-050, IPHE 2001-002.
- [65] *A Long Analog Transmission Line for the VELO Read-Out*, R. Frei, G. Gagliardi, LHCb 2001-072 VELO, IPHE 2001-005.
- [66] *40 Ms/s Analog transmission on shielded twisted pair cable* J. Buytaert, LHCb-98-032.
- [67] *Shielding of the VELO detectors from the LHC beam high-frequency fields: preliminary considerations*, N. van Bakel *et al.*, LHCb 2001-081.

- [68] Y.H. Chin, *User's Guide for ABCI Version 8.7*, CERN SL/94-02 (AP), see also <http://wwwinfo.cern.ch/parc/abci>.
- [69] LHCb Letter of Intent, CERN/LHCC 95-5, LHCC/I8, 25 August 1995.
- [70] *Single-Beam Collective Effects in the LHC*, F. Ruggiero, LHC Note 313 (CERN SL/95-09 AP).
- [71] see e.g. *Coupling impedance measurements: an improved wire method*, in V.G. Vaccaro INFN/TC-94/023, and J.G. Wang and S.Y. Zhang, Nucl. Instr. Meth. **A459** (2001) 381.
- [72] *Design and test of a mixed-phase CO₂ cooling system for the LHCb vertex detector*, O. Postma *et al.*, LHCb 99-046.
- [73] *Radiation tests with foxfet biased microstrip detectors* R. Hammarstrom *et al.*, Nucl. Instr. and Meth. **A418** (1998) 128.
- [74] *The DELPHI Silicon Tracker at LEP2* P. Chochula *et al.*, Nucl. Instr. and meth. **A412** (1998) 304.
- [75] *The P²C-bus and how to use it*, Philips Semiconductors, April 1995.
- [76] *Specifications of the F/E-Chip for the LHCb Vertex Detector*, M. Schmelling, LHCb 2001-048.
- [77] *Effect of Pulse Overspill on the Level 1 Trigger*, P. Koppenburg, LHCb 2001-078.
- [78] *The Beetle Reference Manual*, D. Baumeister *et al.*, LHCb 2001-046.
- [79] *SPAC: Serial Protocol for the Atlas Calorimeter*, R. Bernier *et al.*, 1998.
- [80] *The ECS Interface to the VELO Front-End Electronics*, T. Glebe, LHCb 2001-044.
- [81] *A SPAC based solution for FEE-ECS*, D. Breton, LHCb Electronics Workshop, Jan. 2001.
- [82] *Analog Device AD8055*, <http://www.analog.com/pdf/ad8055.pdf>.
- [83] Proceedings of the Beaune 97 Xth IEEE Real-Time Conference, H.C. van der Bij *et al.*, <http://hsi.web.cern.ch/HSI/s-link/introduc/rt97.ps>.
- [84] *LHCb Level 1 Vertex Topology Trigger*, Y. Ermoline, V. Lindenstruth and A. Walsch, LHCb Note 99-031.
- [85] *Subevent Transport Format (STF) for Readout Units and Link Multiplexers*, H. Muller and J. Toldeo, <http://hmuller.home.cern.ch/hmuller/RU/STFormat/stf.pdf>.
- [86] *Mechanical and Vacuum Stability Design Criteria for the LHC Experimental Vacuum Chambers*, I.R. Collins, O. Gröbner, P. Lepeule, R. Veness, LHC Project Report 205.
- [87] *Aperture requirements around interaction IP8*, G. von Holtey, LHCb note 97-002/EXPT.
- [88] *Design of the VELO exit window*, J.R. Knaster *et al.*, CERN LHC-VAC, Vacuum Technical Note to be published.
- [89] <http://www.nikhef.nl/pub/departments/-mt/projects/lhcb-vertex>.
- [90] *Preliminary Studies for the LHCb Vertex Detector Vacuum System*, O. Postma *et al.*, LHCb 99-045.
- [91] C. Benvenuti *et al.*, CERN EST/99-008 (SM).
- [92] *LHCb Vacuum Calculations*, A. Rossi *et al.*, CERN LHC-VAC, Vacuum Technical Note to be published.
- [93] ARTI, <http://www.arti-21cr.org/db/dataarticle.pdf>.
- [94] CERN Program Library Long Writeup W5013 (1993).

- [95] The average occupancy in T2 and T3 increases by 5%, and does not change in T4 – T11, Minutes of Tracking Meeting, March 27-28 2001 at NIKHEF.
- [96] Relative increase in RICH 1: $(9.0 \pm 0.6)\%$ and RICH 2: $(2.5 \pm 0.6)\%$, private communication J. Libby;
A simulation study of the LHCb RICH performance M. Adinolfi *et al.*, LHCb 2000-066 .
- [97] *Alignment of the DELPHI vertex detector*, V. Chabaud, A. Andreazza, P. Collins, H. Dijkstra, DELPHI note 95-177 MVX 10, December 1995;
Inner Tracking System, ALICE TDR 4, CERN/LHCC 99-12.
- [98] *The VELO as Beam Monitor*, P. Jalocha, LHCb 2001-031.
- [99] *Induced radioactivity in the vacuum chamber*, R. Wigmans, LHCb 2001-052.
- [100] T. Sjöstrand and M. Bengtsson, Comp. Phys. Comm. **43** (1987) 367.
- [101] *Tuning of Multiple Interactions Generated by Pythia*, P. Bartalini *et al.* LHCb note 99-028.
- [102] *VELO Geometry Optimization - An Update*, T. Bowcock *et al.*, LHCb 2001-071.
- [103] *The AXSEL package*, G. Corti, <http://lhcb.cern.ch/gcorti/analysis/axselect.html> .
- [104] *The LHCb vertex locator and level-1 trigger*, H. Dijkstra, LHCb 2000-001.
- [105] *Radiation environment at the LHCb vertex detector area*, V. Talanov *et al.* LHCb note 98-019.
- [106] *Displacement damage in silicon, on-line compilation*, A. Vasilescu (INPE Bucharest) and G. Lindstroem (University of Hamburg), <http://sesam.desy.de/gunnar/Si-dfuncs.html>.
- [107] *Mathematical methods for $B^0\bar{B}^0$ oscillation analyses*, H.-G. Moser, A. Roussarie, Nucl. Instr. and Meth. **A384** (1997) 491.
- [108] *B-Decays in 'Proceedings of the workshop in Standard Model Physics (and more) at the LHC'*, P. Ball *et al.*, CERN 2000-04.
- [109] *LHCb Vertex Locator, Conceptual Design Review*, CERN/EST-LEA/2001-001/dl.